이학박사학위논문

Fluorescence-Raman Endoscopic System for *In Vivo* Multiplexed Molecular Diagnostics

생체 내 다중 분자 진단을 위한

형광-라만 내시경 시스템에 관한 연구

2016년 8월

서울대학교 대학원

과학교육과 화학전공

정 신 영

ABSTRACT

Fluorescence-Raman Endoscopic System for *In Vivo* Multiplexed Molecular Diagnostics

Sinyoung Jeong

Department of Chemistry Education

The Graduate School

Seoul National University

Optical endoscopic imaging, which was recently equipped with bioluminescence, fluorescence, and Raman scattering, allows non-/minimally invasive real-time detection of cellular structural deformations as well as pathological conditions on the surface of hollow organs. Particularly, by integrating the endoscopic imaging techniques with the molecular probes which are able to specifically target toward biomolecules, the *in vivo* and intraoperative molecular diagnostics could be achieved; it allows for early cancer detection, personalized medicine, and image-guided therapy by identifying tumor-related protein expression. Among the various kinds of molecular targeting probes, the fluorescence dyes have been widely utilized to visualize a specifically targeted lesion in extensive area; the surface enhanced Raman scattering (SERS) active nanoparticles (NPs) are also used for

multiplexed molecular diagnostics due to its high sensitivity and multiplexing capability.

As a targeting agent, antibody conjugated NPs have a great potential in diagnostic and therapeutic applications due to their high sensitivity and specificity for bio-targets, as well as their wide applicability. Unfortunately, these features are significantly affected by antibody conjugation methods in terms of conjugation efficiency, orientation of the target binding site in the antibody, and denaturation during chemical conjugation reactions. Furthermore, the number of conjugated antibodies on each NP and the overall targeting efficacy are critical factors for a quantitative bioassay with antibody conjugated NPs. For these reasons, I developed a versatile and oriented antibody conjugation method using copper-free click chemistry. Moreover, the number of conjugated antibodies and their binding capacity were quantitatively and experimentally evaluated using fluorescently-labeled antibodies and antigens. The strong binding capability of antibody-conjugated NPs prepared using the copper-free click chemistry-based conjugation strategy was 8 times superior to the binding capability seen following the use of the EDC/NHS-coupling method.

To characterize pathological condition of suspicious lesions in a multiplexed way during endoscopic procedure, I developed a dual modal fluorescence-Raman endomicroscopic system (FRES), which used fluorescence and surface-enhanced Raman scattering nanoprobes (F-SERS

dots) as targeting agents. By utilizing the FRES along with antibody conjugated F-SERS dots, real-time, *in vivo*, and multiple target detection of a specific cancer was successful, based on the fast imaging capability of fluorescence signals and the multiplex capability of simultaneously detected SERS signals in breast and colorectal cancer (CRC) xenograft models. Human epidermal growth factor receptor 2 (HER2) and epidermal growth factor receptor (EGFR), as tumor cell targeting biomarkers, on the breast cancer xenografts in a mouse orthotopic model were successfully detected in a multiplexed way. As a clinical diagnostic model, in CRC xenograft models, epidermal growth factor receptor (EGFR) for targeting tumor cells and vascular endothelial growth factor (VEGF) for identifying tumor microenvironment were successfully identified using the FRES *via* colonoscopic examination procedure. Additionally, the relative quantification ability of the FRES was demonstrated in *in vitro* and *ex vivo* condition using Raman intensity corresponding to the targeted F-SERS dots. These features illustrated the potential of FRES as a molecular diagnostic tool that enables real-time characterization of tumor cell receptors and tumor microenvironment during routine endoscopic procedures, allowing an early cancer detection and tailored therapy.

Keywords: Fluorescence-Raman Endoscopic System, *In Vivo* Multiplexed Molecular Diagnostics, Full-length Antibody Conjugation, Quantitative Validation, Antibody Orientation Control, Copper-free Click Chemistry, Breast Cancer, Colorectal Cancer

Student number: 2012-31069

TABLE OF CONTENTS

LIST OF TABLES

LIST OF FIGURES

LIST OF ABBREVIATIONS

SERS	Surface Enhanced Raman scattering
NP	Nanoparticles
FRES	Fluorescence-Raman endoscopic system
CRC	Colorectal cancer
HER2	Human epidermal growth factor receptor-2
EGFR	Epidermal growth factor receptor
VEGF	Vascular endothelial growth factor
F-SERS dots	Fluorescence-surface enhanced Raman scattering nanoprobes
AF	Alexa fluor
CLSM	Confocal laser scanning microscopy
TEOS	Tetraethyl orthosilicate
MPTS	3-Mercaptopropyltrimethoxysilane
EG	Ethylene glycol
OA	Octylamine
APTES	3-Aminopropyltriethoxysilane
RITC	Rhodamine B isothiocyanate
FITC	Fluorescein isothiocyanate
DMSO	Dimethyl sulfoxide
NMP	*N*-methyl-2-pyrrolidone
NHS	*N*-hydroxysuccinimide
DIC	*N,N'*-diisopropylcarbodiimide
DIPEA	*N,N'*-diisopropylethylamine
DMAP	4-Dimethylaminopyridine
BSA	Bovine serum albumin

PBS	Phosphate-buffered saline
a.u.	Arbitrary unit
cps	Count per second
SD	Standard deviation
DAPI	4`,6-diamino-2-phenylindole
IHC	Immunohistochemistry
NTA	Nanoparticle tracking analysis

Fluorescence-Raman Endoscopic System for *In Vivo* Multiplexed Molecular Diagnostics

Introduction

1. Endoscopic Imaging Techniques

Endoscopy is an important and essential tool for screening and managing a cancer in hollow organs, such as the esophagus, stomach, and colon, with non-invasive procedure.[1, 2] The endoscope utilizing white-light can visualize surface morphology in internal organs with real-time that enable the physicians to diagnose a certain cancer during endoscopic examination. Along with diagnostic ability, it offers proper and effective treatment by the endoscopic resection or ablation during endoscopic examination. Thus, there has been a growing interest in improving detection sensitivity and spatial resolution of endoscopic optical imaging to detect a cancer at an early stage.[3, 4]

Thus far, by utilizing advanced white light reflectance (WLR), fluorescence, and chromogenic dye, the endoscopic imaging techniques have been developed to improve diagnostic sensitivity and spatial resolution for suspicious lesion. These advanced endoscopic imaging techniques enable a visualization of surface morphology with high magnification or even a subcellular change with high spatial resolution, allowing discrimination of abnormal lesions from normal surfaces.[5-7]

In common wide-field endoscopy, the narrow band imaging (NBI) technique has been widely utilized to improve detecting sensitivity of

conventional endoscope by enhancing the contrast of suspicious lesion in esophagus, stomach, and colon. The NBI technique can be easily applied during conventional WRL endoscopy by employing special optical filters for reducing white-light to two 30-nm-wide spectra corresponding to blue and green light. Since the hemoglobin more readily absorb in green and blue light, blood vessels appear more dark than surrounding tissue; the visuality of WRL endoscopy could be improved for differentiating between benign and malignant tissues.[8] Furthermore, the NBI endoscope also provides wide-field macroscopic images that enable red flag detection of suspicious lesion, such as filter techniques, in large surface of hollow organ, allowing subsequently precise characterization.

The confocal laser endomicroscopy (CLE) has emerged as a new complementary endoscopic imaging technique to highly improve spatial resolution of endoscopic images up to sub-cellular level, which cannot be seen by WLR endoscopy; the CLE thus offers rapid histological assessment of suspicious lesion, so called "optical biopsy", resulting in diagnosis of a inflammation or dysplasia in flat or depressed suspicious lesion.[9-11] The CLE system constructs the endomicroscopic images by obtaining the fluorescence signals comes from prestained tissue; the fluorescent contrast agents, such as fluorescein, acriflavine hydrochloride and cresyl violet, must be injected to

patients *via* intravenously or directly spraying on to the suspicious lesion.[12]

So far, the CLE system has been integrated with conventional endoscope by either embedding onto the tip of the endoscope or using an optical fiber bundle probe which can be inserted through the instrument channel of conventional endoscope. The embedded CLE technology (eCLE, Pentax, Japan), by directly embedding at the end of endoscope, offers high-resolution images with lateral resolution of 0.7 μm and z-stack confocal microscopic images by collecting the signals from various optical sections (an axial resolution of 7 μm); it enables the detection of subcellular structural changes in deep mucosa. Kiesslich and colleagues have demonstrated the feasibility of eCLE in identification of Barrett's-related neoplasia and screening colorectal cancer with high sensitivity and specificity during endoscopy.[13-15]

Alternatively, the probe-based CLE system (pCLE) has been developed by utilizing the optical fiber bundle as a detecting probe (Cell-vizio, France).[16] The pCLE system can be introduced through instrument channel of any commercial endoscope; this feature allows for utilizing various kinds of endoscopic imaging techniques involving NBI. Additionally, due to its small tip (< 2 mm), it can access to narrow tubular internal organs such as bile ducts and duodenum.[17, 18] Neurath group has evaluated mucosal inflammation and tumor development in a mouse model by combining the pCLE with NBI

endoscope.[19] Muldoon and colleagues have developed high resolution microendoscopy (HRME) with low-cost and small-caliber fiber optic image guide bundle, and successfully applied to diagnose the Barrett's esophagus, oral neoplasia, in *ex vivo*. [5, 20-23]

Although the endoscopy has achieved great advancements in endoscopic imaging capabilities, the accuracy and reliability of detecting the precancerous lesions highly rely on the examiner's ability and experience with solely visual inspection. Especially, subtle neoplastic molecular changes, which are essential to determine the pathological condition, in flat and depressed lesions are difficult to identify based only on these morphological information.[24, 25] Hence, the complimentary functionalities, which can provide molecular information, have been required to accurately detect an early stage of cancer based on objective pathological molecular characteristics of suspicious lesion, along with the structural imaging provided by white-light endoscopy.

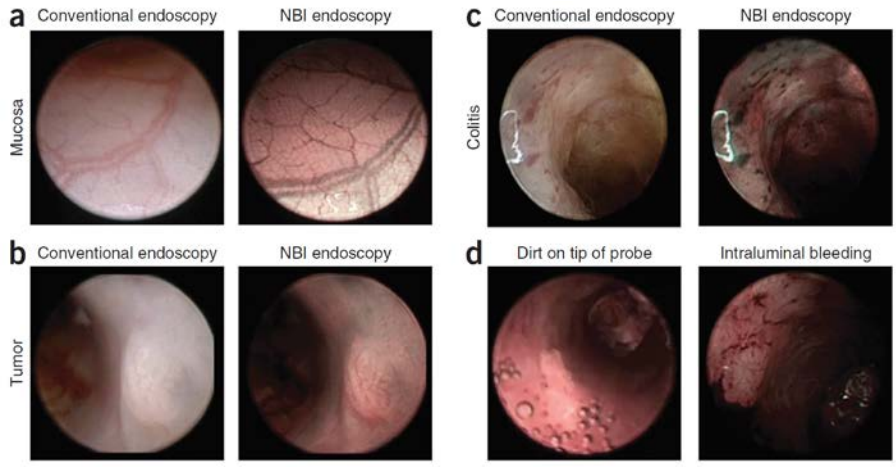

Figure 1. NBI endoscopic images in mouse models of inflammation and tumor development. (a,b) The vessel architecture is more pronounced in the mucosa (a) and tumors of the colon (b) and thus facilitates the detection of pathological changes. (c) Images of colitis show morphological alterations of the mucosa with microbleeds. (d) Possible reasons for poor image quality include dirt on the endoscopic probe and intestinal bleeding, which lead to an increased absorption of blue and green light and therefore result in a darker image.[8]

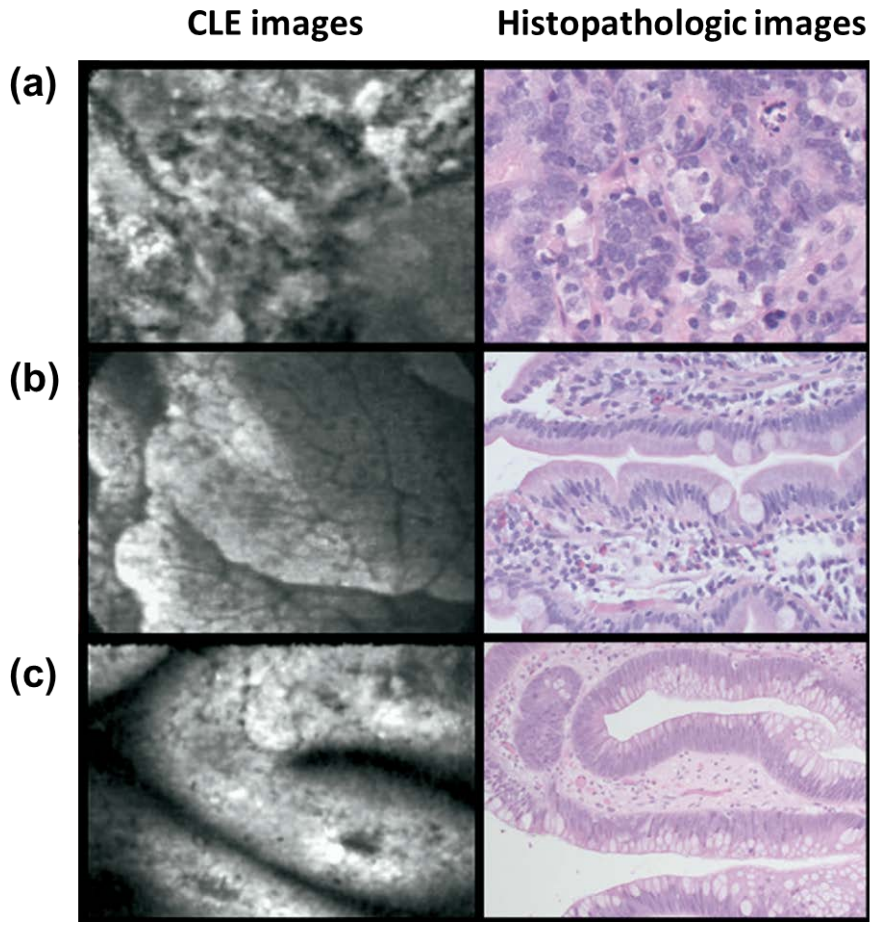

Figure 2. Confocal laser endomicroscopic (CLE) images and corresponding histopathologic images. (a) Esophagus tumor, (b) duodenum, and (c) rectal polyp.[18]

2. Endoscopic Intraoperative Molecular Diagnostics

Molecular imaging employs molecular probes such as antibody, peptide, and aptamer that can specifically target biomolecules associated with a cancer; the molecular imaging therefore allows for early cancer detection, personalized medicine according to pathological condition, image-guided therapy by localizing tumor margins, and monitoring for recurrence based on protein expression.[26] In particular, molecular properties of suspicious tissue reveals unvisualized tissue behavior that can be utilized to discriminate the precancer lesions from normal tissues before gross morphological abnormality.[27]

Until now, many researchers have reported the various kinds of intraoperative molecular diagnostic tool by combining the conventional endoscope with additional functionalities involving fluorescence and Raman spectroscopy. By utilizing the fluorescence functionality, an intraoperative molecular diagnostic method was proposed to specify the tumors in such lesions so that folate-FITC was intravenously administered for targeting folate receptor-α to detect ovarian cancer.[28] Another approach was to spray fluorescent antibodies, the FITC-labeled adalimubab antibodies, over the mucosa of the colon during a colonoscopy, and it successfully visualized the mucosal membrane-bound TNF+ immune cells.[29] Both techniques were

successfully administered in humans, and considering the difficulty in depth imaging, topical application and wide field imaging might be a preferred method.

As an another functionality, Raman spectroscopy were added to the endoscopic system to enhance the lesion detectability and to further characterize the molecular pathologies.[24, 25, 30-33] In particular, by obtaining the Raman fingerprints without any tagging agent, subtle neoplastic changes could be discerned in the pre-cancerous lesion.[31-34] Huang and colleagues have demonstrated the applicability of Raman endoscope by distinguishing Raman signals of between normal and diseased tissue in cervix, esophagus and stomach.[35-38] However, intrinsic Raman endoscopy has limitations in clinical applications, such as real-time imaging, because intrinsic Raman fingerprints lack sufficient sensitivity, and there are less distinctive spectral patterns between normal and cancerous lesion and obliterated diagnostic accuracy due to high false-positive/negative results.[39-41]

To overcome these limitations, nano-probes based on surface-enhanced Raman scattering (SERS probes) were proposed as staining agents to target molecular biomarkers of the tumors.[39, 40] The SERS probes consisted of a noble metal SERS substrate, Raman label compounds, a protective shell layer, and tumor-targeting ligands on the shell surface. These SERS probes were

equipped with a unique spectral fingerprint to tag a specific bio-target with high sensitivity.[42-44] A strong localized surface plasmon in the vicinity of the noble metal surface dramatically enhanced the signals of the Raman label compounds by up to 10-14 orders of magnitude, and thus the Raman signals produced by SERS probes were much stronger than the intrinsic ones.[45, 46] SERS probes have had a large multiplexing capability owing to its narrow spectral bandwidth (< 1 nm) and utilization of a single photo-excitation line for multiple targets detection.[47-49] Peptides, aptamers, or antibodies can be conjugated with SERS probes to identify various biomolecules by selective and specific targeting.[49, 50]

Although SERS probes offer high sensitivity and selectivity for the molecular diagnosis of specific cancers, SERS probes-based Raman endoscopy is still limited in identifying cancerous tissues hidden within the vast normal-looking tissues. To solve this problem, a point-by-point mapping is required for the SERS probes targeted to the cancerous tissue, but scanning large areas within a practical time poses great difficulties because of the post data processing and relatively low spatial resolution.[51] To achieve the high sensitivity and multiplexing capability as well as rapid imaging ability, the dual-modal probes integrate the fast imaging ability of fluorescence moiety and high multiplexing capability of SERS, which can be used as a clinical

screening tag, in conjunction with the dual-modal imaging endoscopic techniques.[52-54]

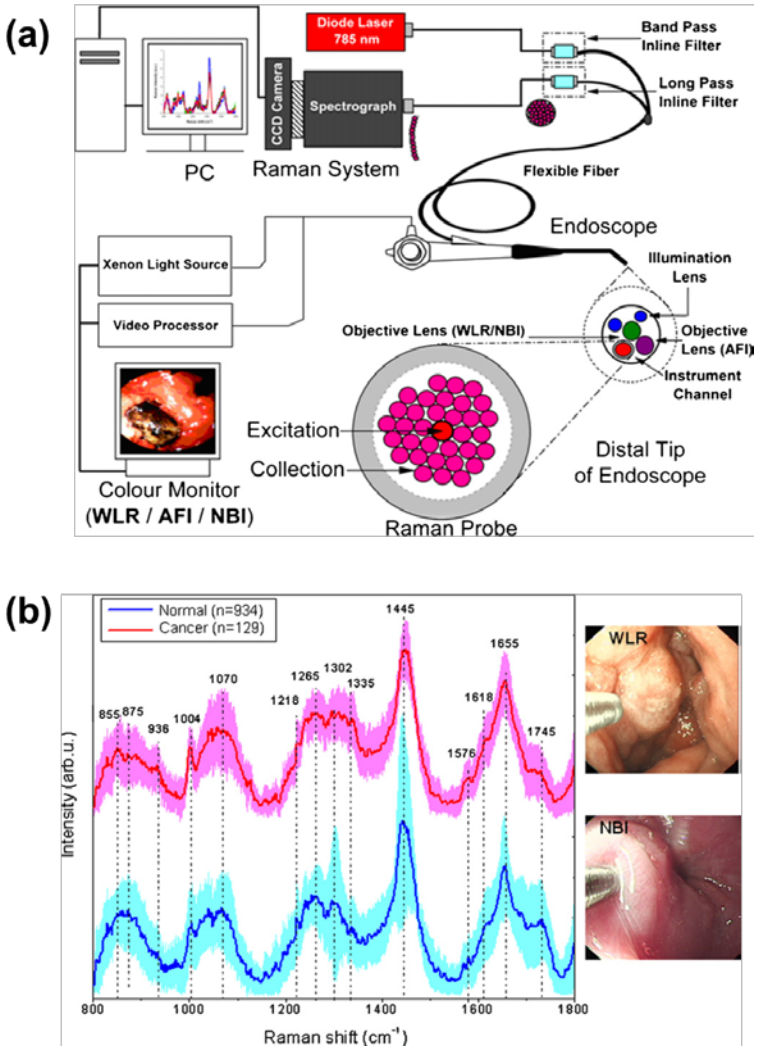

Figure 3. The Raman endoscope. (a) The schematic of Raman endoscope system. WLR, white light reflectance; AFI, autofluorescence imaging; NBI, narrow-band imaging. (b) *In vivo* mean Raman spectra of normal (n = 934), and cancer (n = 129) gastric tissue, as well as the corresponding WLR image and NBI acquired during clinical gastroscopic examination.[32]

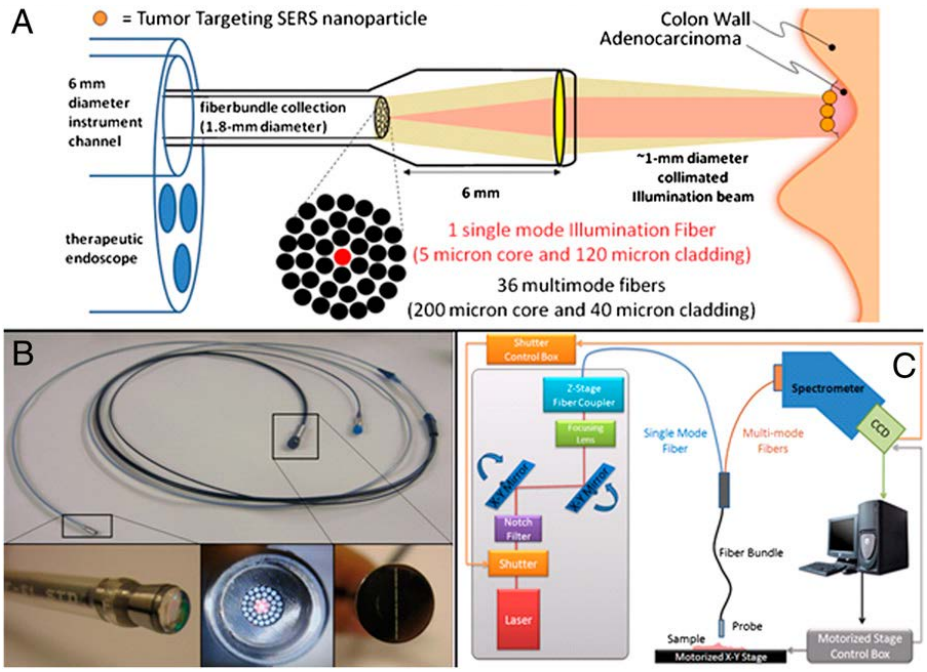

Figure 4. Raman endoscope design and setup incorporating SERS active nanoprobes as a targeting agent. (a) Schematic of Raman endoscope designed to be inserted through the accessory channel of a clinical endoscope with a 6-mm instrument channel. (b) Photograph depicts the final fabricated Raman endoscope to be used for clinical studies. (Lower) Enlarged digital photograph of the endoscope head (Left), a magnified photograph of the fiber bundle (Center), and a magnified photograph of the back end of the device (Right). (c) Schematic of the entire device setup.[39]

3. Antibody Conjugation Strategy

Antibodies have been widely utilized as a targeting moiety in diagnostic and therapeutic applications such as immunoassays, nanoparticle-targeted molecular diagnosis, targeted drug delivery, and radio-immunotherapy, due to their high affinity, specificity, and broad applicability with well-established production techniques.[55-59] To take advantages of antibodies in such applications, proper conjugation of antibodies to nanoparticles (NPs) is an essential process. However, during the conjugation step, the majority of conjugation methods suffer from various limitations such as heterogeneity, low conjugation efficiency, and low reproducibility.[60, 61] In particular, when antibodies are conjugated to a solid surface, their orientation on the surface is a critical factor for the detection of bio-targets, since the limited freedom of movement and the consequent limited accessibility of antigen-binding sites reduce antibody binding efficacy.[62-65] Thus, in biochemical and medical applications using antibodies, the sensitivity of immunosensors or the efficacy of targeted therapies are greatly affected by antibody conjugation methods. In this regard, considerable effort has been made to develop antibody conjugation methods while preserving the biofunctionality of antibodies.[60, 63, 66, 67]

To date, various strategies have been developed to conjugate antibodies

to a solid surface involving NPs. One of the most common antibody conjugation methods utilizes a primary amine functional group on the antibody with 1-ethyl-3-(3-dimethylaminopropyl)-carbodiimide hydrochloride (EDC) and/or *N*-hydroxysulfosuccinimide (Sulfo-NHS) as coupling reagents. This conjugation method can offer high stability in various biological conditions by the formation of stable amide bonds between the NPs and antibodies. Nonetheless, since the primary amine functional groups exist randomly throughout the antibody, the orientation of antibodies on a solid surface is random, and thus, the antigen-binding sites on a proportion of the antibodies are inevitably blocked, which results in diminished selective binding ability.[65, 68] Moreover, the EDC/Sulfo-NHS coupling has been shown to result in a low coupling efficiency; only 1-20% of antibodies are able to be conjugated to the solid surface, which may lead to a high cost for the preparation of specifically-targetable NPs.[59, 69] During the chemical reaction, partial denaturation of the antibodies may also occur, resulting in a decrease in antigen-binding ability.

As one of the alternative approaches, click chemistry has been utilized to conjugate antibodies to NPs, owing to its high conjugation efficiency, reproducibility, and reaction specificity between azide and alkyne functional groups.[66, 70-73] Furthermore, only those click chemicals react with each other to

form a triazole ring without interference from endogenous biological materials, which enables investigation of bio-interactions in an *in vivo* system. In particular, by using the strain-promoted alkyne-azide cycloaddition (SPAAC) reaction, the click reaction can occur in mild reaction conditions, resulting in minimization of chemical damage to antibodies during the conjugation reaction.[70, 71] However, commonly used click chemistry requires transformation of amine groups in antibodies to azides or terminal alkynes, and still cannot control the orientation of conjugated antibodies.[66]

To maintain full bio-functionality *via* the control of the orientation of antibodies conjugated to a solid surface, several site-specific antibody conjugation methods have been developed using antibody binding proteins or antibody fragments. Antibody binding proteins such as protein A, G, and Z can specifically bind to the specific site in Fc region of an antibody; thus, the orientation of antibodies can be properly controlled.[60, 68, 74, 75] Unfortunately, this technique has limits with respect to its versatility and applicability, since the protein A and G can bind to only specific IgG subclasses and not all kinds of antibodies.[67] Moreover, these site-specific conjugation methods require technically complex procedures and genetically engineered proteins, resulting in a high cost and lack of applicability. As an alternative site-specific antibody conjugation method, half-antibody fragments with free sulfhydryl groups have

been employed by reducing disulfide bridges in the hinge region of intact antibodies using dithiothreitol (DTT) or tris(2-carboxyethyl)-phosphine hydrochloride (TCEP).[73, 76] By utilizing the free sulfhydryl groups in the Fc region, the half-antibody fragments can be efficiently conjugated to a solid surface with control of the orientation of antigen-binding sites. Nevertheless, this method also suffers from lack of reproducibility and consistent affinities, since the disulfide bonds in antigen-binding sites are also easily cleaved along with those at the hinge site, resulting in denaturation of the antibodies. Hence, in order to preserve the antigen-binding ability following antibody reduction, the reducing conditions should be precisely determined.[77]

Thus far, there exists the issue that the number of antibodies on a single NP and the target binding capability of conjugated antibodies have not yet been determined, quantitatively and experimentally. This is a significantly important issue for the proper interpretation of the results of bioassays labeled with antibody-conjugated NPs.[76] Although several efforts have been previously reported for the quantification of the number of antibodies conjugated with NPs,[73, 76] they still cannot sufficiently provide quantitative and experimental analysis for the assessment of the antigen-binding ability of conjugated antibodies.

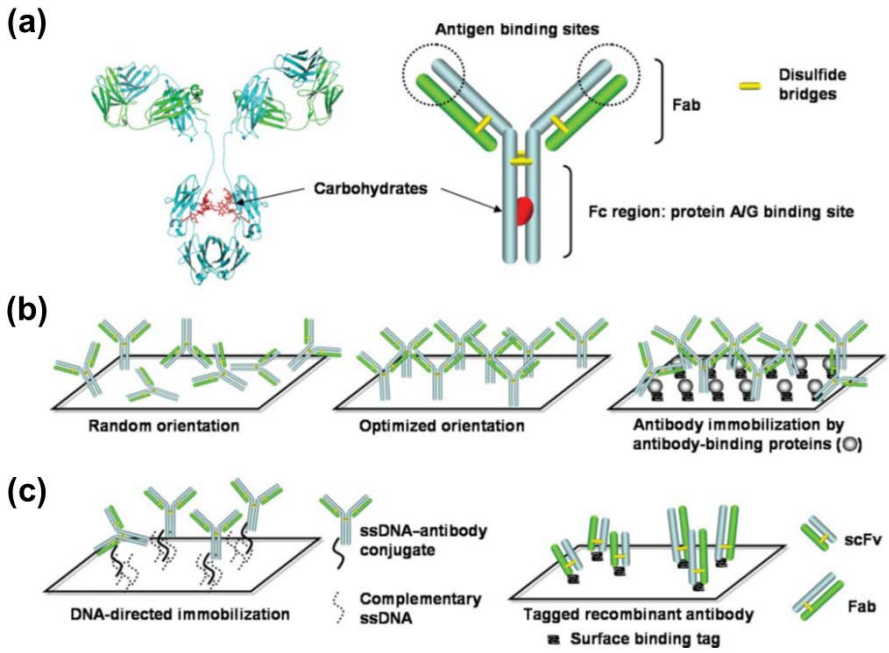

Figure 5. Schematic representations of antibody and surface immobilization. (a) Crystal structure and diagram of an antibody: antibody Fc (fragment crystallizable) and Fab (fragment antigen binding) regions, carbohydrates, disulfide bridges, and antigen binding sites are indicated. (b) Antibody immobilization on solid surfaces with random orientation, ideal straight upward orientation, and antibody-binding protein-mediated orientation. (c) Examples of recent strategies for antibody immobilization: DNA-directed antibody immobilization and recombinant antibody immobilization.[78]

4. Research Objectives

In this study, I newly developed the fluorescence-Raman endoscopic system (FRES) along with fluorescence-SERS active nanoprobes (F-SERS dots) having tumor specific antibody as targeting agents for *in vivo*, *in situ*, and intraoperative multiplexed molecular diagnostics with real-time. The performances of this system were evaluated as an *in vivo* molecular diagnostic tool in terms of sensitivity, endomicroscopic imaging ability, and multiplex targeting ability.

To prepare the targeting agents by conjugating antibodies to NPs, highly robust and optimized antibody conjugation method for NPs was developed by using copper-free click reaction with simple and facile reaction procedure. Additionally, for control of the antibody orientation, site-specific modification of disulfide bonds in the Fc domain of full antibodies was utilized, by reduction to thiol groups with highly optimized reaction conditions. The orientation of antibodies could therefore be controlled, allowing binding sites to be available to target molecules without steric hindrance, resulting in an improvement in the target-binding capability. Furthermore, I proposed an experimental quantification protocol for the number of antibodies on a single NP and their biofunctionality. Firstly, the number of nanoparticles was quantitatively and experimentally determined, and subsequently, the number

of antibodies bound to a single NP was determined using fluorescently labeled antibodies. The bio-functionality of conjugated antibodies was also quantitatively determined using fluorescently labeled antigens. The high targeting ability following the use of this conjugation strategy was successfully demonstrated by active targeting of a breast cancer cell line in comparison with EDC/Sulfo-NHS coupling methods. Additionally, the versatility and expandability of this strategy were also demonstrated by the successful conjugation of three types of silica-encapsulated nanoprobes to antibodies, regardless of the internal structure of the nanoprobes.

Lastly, with this simultaneous use of an intraoperative endoscopic visualization with F-SERS dots, the feasibility of the FRES could be demonstrated in a mouse orthotropic breast and colorectal cancer xenograft model. The FRES exhibited high sensitivity and multiplexing capability for an *in vivo* endoscopic molecular diagnosis of tumors by identifying the tumor location, characterizing the surface receptors and tumor microenvironment, simultaneously, which enabled rapid identification of pathological condition and accurate diagnosis of specific cancer at an early stage.

Experimental Section

1. Chemicals and Materials

Tetraethyl orthosilicate (TEOS), 3-mercaptopropyltrimethoxysilane (MPTS), ethylene glycol (EG), silver nitrate ($AgNO_3$, > 99.99%), 3-aminopropyltriethoxysilane (APTES), octylamine (OA), rhodamine B isothiocyanate (RITC), fluorescein isothiocyanate (FITC), dimethyl sulfoxide (DMSO), *N*-methyl-2-pyrrolidone (NMP), *N*-hydroxysuccinimide (NHS), *N*,*N*′-diisopropylcarbodiimide (DIC), *N*,*N*′-diisopropylethylamine (DIPEA), 4-dimethylaminopyridine (DMAP), bovine serum albumin (BSA, > 98%) phosphate-buffered saline (PBS, tablet) were purchased from Sigma-Aldrich Inc. (St. Louis, MO, USA). Succinimidyl ester conjugated with Alexa Fluor (AF) 563, 594, 610-X, and 633 were purchased from Invitrogen Inc. (Carlsbad, CA, USA). The 3-azidopropyl-1,4,7-triaza-cyclononane-1,4,7-triacetic acid (NOTA-N_3), NOTA-ADIBO, and ADIBO-PEG4-Maleimide (ADIBO-PEG4-Mal) were purchased from FutureChem (Seoul, Korea) and used without further purification. Absolute ethanol (99.9%), ammonium hydroxide (NH_4OH, 27%), 2-propanol (99%), and ethanol (99.9% and 98%) were purchased from Daejung Chemicals (Siheung, Korea). Deionized (DI) water was used for all experiments. Herceptin [anti-human epidermal growth factor receptor 2 (anti-HER2) monoclonal antibody], Cetuximab [anti-epidermal growth factor receptor (anti-EGFR) monoclonal antibody], and

Bevacizumab [anti-vascular endothelial growth factor (VEGF) monoclonal antibody] were purchased from Merck Millipore (Darmstadt, Germany). Recombinant Human EtbB2 (HER2 antigen) was purchased from Sino Biological Inc. (Beijing, China). Instant thin layer chromatography-silica gel (ITLC-SG) plates were purchased from Agilent Technologies, Inc. (Santa Clara, CA, USA). PD-10 size-exclusion columns were obtained from GE Healthcare (Buckinghamshire, U.K.).

2. Instruments

UV-Visible extinction spectra were obtained by UV-Visible spectrometer (Cary 300 Bio, Agilent, Santa Clara, CA, USA). The size and concentration of nanoparticles were determined by nanoparticle tracking analysis (NTA; Nanosight LM10, Malvern, Worcestershire, UK). The shape and morphology of nanoparticles were characterized by energy-filtering transmission electron microscope (EF-TEM, LIBRA 120, Carl Zeiss, Oberkochen, Germany). Radioactivity was measured using a gamma scintillation counter (Packard Cobra II, GMI, NM, USA). Antibody molecular weight was measured by matrix-assisted laser desorption ionization time of flight/time of flight mass spectrometry (MALDI-TOF/TOF MS) using the TOF/TOF 5800 system (AB Sciex, Foster City, CA, USA). Antibody concentration was measured spectrophotometrically using a NanoDrop® ND-1000 spectrophotometer (Nano-Drop Technologies, Wilmington, DE, USA). Fluorescence imaging was performed using a Xenogen IVIS 200 small animal imaging system (Xenogen, Alameda, CA, USA). Fluorescence images of cells were obtained by Confocal Laser Scanning Microscopy (CLSM; SP8 X, Leica, Wetzlar, Germany).

3. Fluorescence-Raman Endoscopic System (FRES)

3.1 Design of the FRES

The FRES used a continuous wave diode-pumped solid-state 532-nm laser (Cobolt Samba™, Cobolt, Sweden) coupled with a single mode fiber for light delivery. A custom-made dual-axis laser scanning unit (Raman proto type of Cell-Vizio, Mauna Kea Technologies, France) combined with a spectroscopic system for real-time fluorescence imaging and multiplexed Raman detection utilized an optical fiber bundle for delivery of the incident light to the sample and collection of the lights from it.[16] This optical fiber bundle consisted of *ca*. 100,000 optical fibers of 2-μm diameter and had an overall external diameter of 2.6 mm. The working distance of the optical fiber bundle was 60 μm and its field of view was 240 μm. The separation unit used two optical filters: A long-pass dichroic filter (FF593-Di03-25D, Semrock Inc., Rochester, NY) for separation of scattering light and fluorescence light and an edge filter (LP03-532RS-25, Semrock Inc.) for separation of Rayleigh- and Raman-scattering light. To detect Raman signals, a spectrometer (SR 303i-A, Andor Technology, Belfast, UK) with a thermo-electrically cooled CCD detector (DV401A-BV, Andor Technology) was utilized. The fluorescence signal was collected by an avalanche photodiode and processed into real-time images by the imaging software (ImageCell, Mauna Kea Technologies)

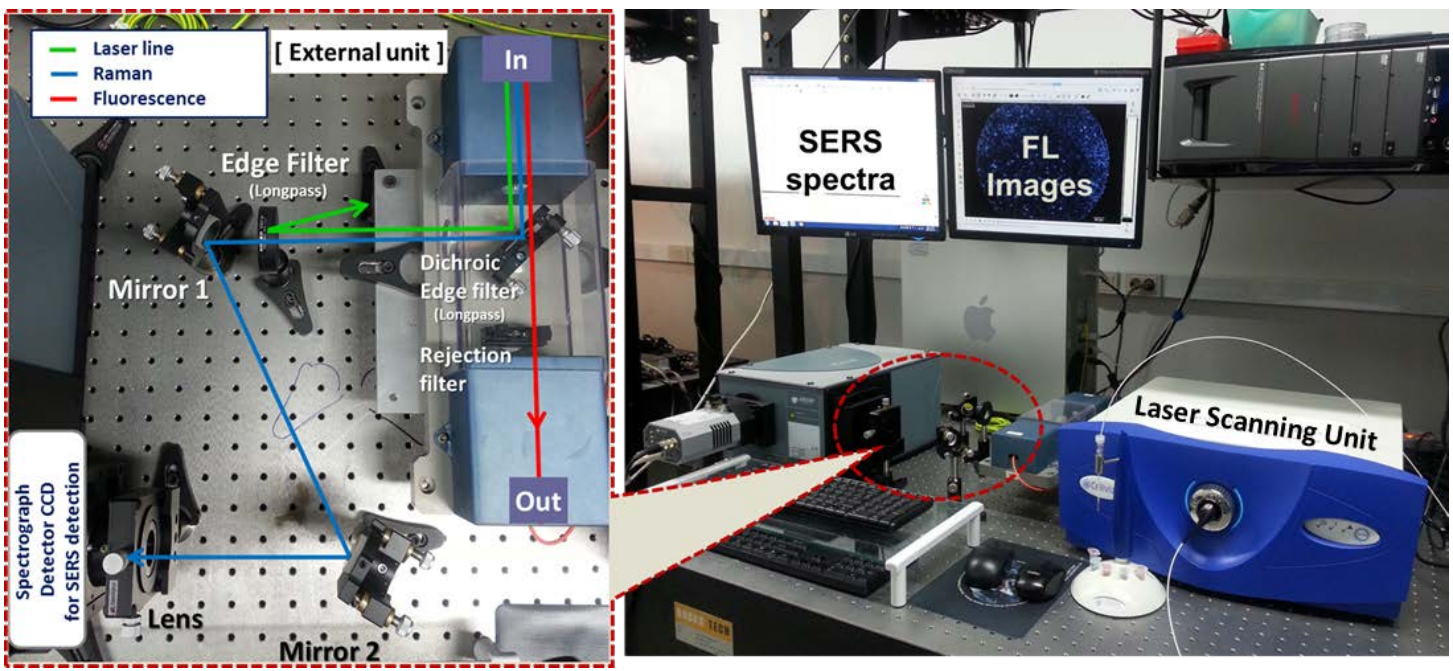

Figure 6. Photograph of the fluorescence-Raman endoscopic system (FRES)

3.2 Preparation of fluorescence surface-enhanced Raman scattering probes (F-SERS dots)

The schematic illustration of fabrication process of fluorescence-surface enhanced Raman scattering nanoprobes (F-SERS dots) is shown in Figure 7. The *ca.* 200-nm sized silica nanoparticles (NPs) were synthesized by the Stöber method.[79] Tetraethyl orthosilicate (TEOS, 1.6 mL) was dissolved in 40 mL of absolute ethanol, followed by addition of ammonium hydroxide (NH_4OH, 27%, 3 mL). The resulting mixture was vigorously stirred using a magnetic bar for 20 h at 25°C. The silica NPs were centrifuged and then washed with ethanol several times to remove excess reagents. These silica NPs were then functionalized with thiol groups as described below. The silica NPs (100 mg) were dispersed in 2 mL of ethanol containing 100 μL MPTS and 20 μL NH_4OH (27%). The mixture was stirred for 2 h at 25°C. Subsequently, the resulting thiol-functionalized silica NPs were centrifuged and washed with ethanol several times. One hundred milligrams of thiol-functionalized silica NPs was thoroughly dispersed in 50 mL of $AgNO_3$ solution (3 mM in ethylene glycol). Octylamine (82.7 μL, 10 mM) was then rapidly added to the above dispersion and stirred for 1 h at 25°C. Octylamine was used as both a reducing agent and as a stabilizer for the mild nucleation of the silver NPs on the surface of the silica NPs. The resulting silver-

embedded silica (Ag Si) NPs were then centrifuged and washed with ethanol several times for purification. These Ag Si NPs were labeled with two kinds of Raman-label compounds (RITC and FITC). Ten milligrams of Ag Si NPs were dispersed in a 1 mL ethanol solution containing 1 mM of each Raman label compound. The dispersion was shaken for 30 minutes at 25°C. The Raman-labeled Ag Si NPs (SERS NPs) were centrifuged and washed with ethanol two times to remove excess reagents. These SERS NPs were coated with a silica shell to prevent aggregation and fluorescence quenching as described below.[52] Ten milligrams of SERS NPs was dispersed in 24 mL of a solution containing 2-propanol (20 mL) and water (4 mL). Then, NH_4OH (27%, 600 μL) was then added to this dispersion. Next, TEOS (7 μL) was added into the mixed dispersion three times each at the intervals of 1 h and then stirred for 24 h. The silica-coated SERS NPs were centrifuged and washed with ethanol several times to remove excess reagents. Next, these silica-coated SERS NPs were encapsulated by a fluorescence dye conjugated to the silica shell. A 50 μL of the APTES (19.2 mM in ethanol) and 5 μL of the AF610 (8 mM in DMSO) were mixed to allow the conjugation of the APTES and fluorescence dye. The resulting solution was stirred for 15 h at 25°C. A 10 mg portion of silica-coated SERS NPs were dispersed in 24 mL of a mixed solution containing 2-propanol (20 mL) and water (4 mL). Then, 55 μL of the

AF610-APTES conjugated ethanol solution was added to this dispersion. Subsequently, 10 μL of the TEOS and 0.5 mL of NH_4OH (27%) were added. The dispersion was stirred for 9 h at 25°C. The final nanoprobes (the F_{AF610}-$SERS_{RITC/FITC}$ dots) were centrifuged and washed with ethanol several times for purification.

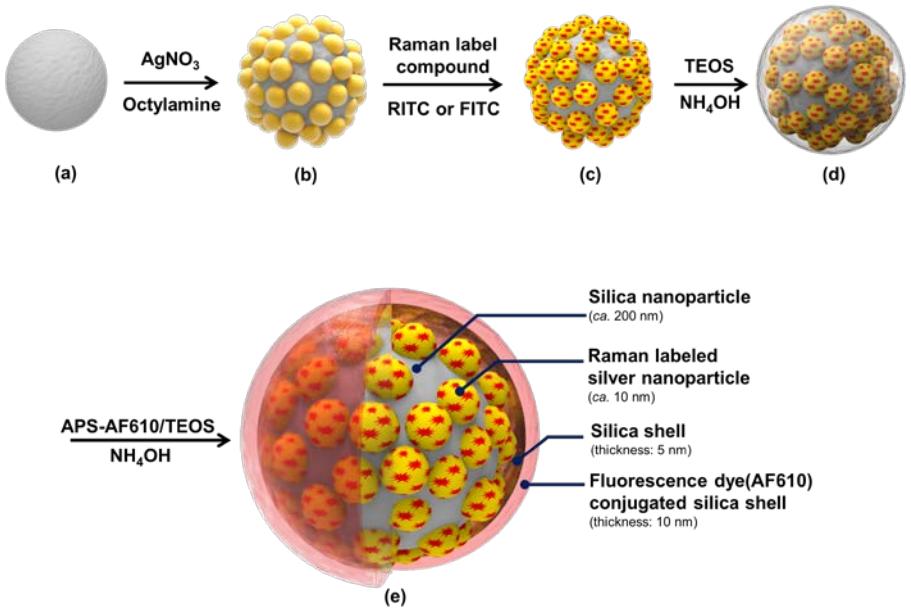

Figure 7. Schematic illustration of fabrication procedure of fluorescence-SERS active nanoparticle (F-SERS dot). (a) Silica nanoparticle (NP), (b) silver-embedded silica NPs (Ag silica), (c) Raman-labeled Ag silica (SERS NPs) by RITC or FITC respectively, (d) silica shell-coated SERS NPs, and (e) fluorescence dye (AF610) conjugated silica shell coated SERS NPs (F-SERS dot).

3.3 Immobilization of antibodies on F-SERS dots

A 1 mg portion of the F-SERS dots was dispersed in 1 mL of the APTES solution (5 vol% in ethanol), and 10 μL of NH_4OH (27%) was added. The resulting dispersion was vigorously stirred for 1 h at room temperature. The APTES-treated F-SERS dots were washed with ethanol several times, and then re-dispersed in 500 μL of NMP. Succinic anhydride (1.75 mg) was added to the APTES-treated F-SERS dots dispersion, followed by adding 3 μL of DIPEA to introduce carboxyl groups on the F-SERS dots. The resulting mixture was stirred for 2 h. Subsequently, the carboxyl group-functionalized F-SERS dots were washed with DMF three times and then re-dispersed in 200 μL of anhydrous DMF. Then, DIC (2.7 μL), NHS (2 mg), and DMAP (0.21 mg) were added to the dispersion of carboxyl group-functionalized F-SERS dots to activate the carboxyl groups for antibody conjugation. The resulting mixture was stirred for 2 h and then washed with PBS (pH 7.4) three times. Herceptin (50 μg, Trastuzumab; anti-HER2/neu receptor monoclonal antibody) or Cetuximab (50 μg; anti-EGFR monoclonal antibody) was added to the NHS-activated F_{AF610}-$SERS_{RITC/FITC}$ dots dispersed in 200 μL of PBS. The mixture was incubated for 1 h at 25ºC. The antibody-immobilized F-SERS dots were centrifuged and washed with PBS containing 0.1% (w/v) Tween 20 and PBS, consecutively. Finally, the antibody-immobilized F-SERS

dots were treated with BSA (1% (w/v) in PBS solution, pH 7.4) for 30 minutes and washed with PBS solution containing Tween 20 and PBS.

3.4 Measurement of confocal microscope Raman system

As an additional characterization of fabricated F-SERS dots, Raman measurements were performed using a confocal microscope Raman system (LabRam 300, JY-Horiba, France) equipped with an optical microscope (BX41, Olympus, Japan). In this system, the Raman scattering signals are collected in a back-scattering geometry and detected by a spectrometer equipped with a thermo-electrically cooled CCD detector. The excitation source is the 532-nm line of a diode-pumped solid-state laser (CL532-100-S, CrystaLaser, Reno, Nevada). Focusing of the excitation laser lights and collection of Raman signals are accomplished by the same 100× objective lens (NA 0.90, Olympus, Tokyo, Japan). The strong Rayleigh-scattering light was eliminated by a long-pass edge filter. Raman spectra were acquired using 2.8-mW laser power, and a 1-s acquisition time. The fluorescence spectra were also obtained under the same excitation and acquisition condition.

4. Highly Robust and Optimized Conjugation of Antibodies to Nanoparticles using Quantitatively Validated Protocols

4.1 Preparation of reduced antibody and ADIBO conjugated antibody

To functionalize the antibody with ADIBO, a thiol group was derived from the disulfide bonding in antibodies, which were reduced according to a previously developed procedure.[80, 81] In order to optimize the reaction conditions, four different reducing conditions were tested. For 0.25 mL of antibody in phosphate-buffered saline (PBS) solution (2 mg/mL), 2 μL of ethylenediaminetetraacetic acid (EDTA) in deionized water (DW,0.3 M, pH 8.0), 2 μL of sodium bicarbonate in DW (1 M), and 2.5 μL of β-mercaptoethanol in DW (1.5 M) were added (Reaction 1). In reactions 2-4, the same quantity of antibody was used, while the volumes of the other reagents were increased by 2, 4, and 8 times for harsher conditions. All reactions were incubated at 37ºC for 1 h. Reduced antibody was purified using a PD-10 column with PBS. Subsequently, by reacting the thiol group in the antibody with maleimide-ADIBO, the ADIBO functionalized antibody was prepared.

4.2 Evaluation of azide functionalization of SiNPs and ADIBO functionalization of antibody by radio-TLC

The radioisotope (^{64}Cu) containing vials were blow-dried by N_2 gas in a fume hood for 1 h. After the vial was completely dry, 200 µl of 1 M sodium acetate buffer (pH 5.3) was added to reach pH 5. 7.5 nmol of NOTA-N_3 or NOTA-ADIBO was then added and the vials were incubated at 60ºC for 30 min on a heating block. Radiolabeling efficiency was determined using radio-instant thin layer chromatography-silica gel (radio-ITLC-SG) following the radiolabeling procedure with citric acid (retardation factor (R_f) of radiolabeled NOTA-N_3 or NOTA-ADIBO = 0.6-0.7; R_f of free radioisotope = 0.9-1.0; R_f of radiolabeled Ab or radiolabeled NP conjugate = 0.0-0.1) as the mobile phase.

4.3 MALDI-TOF mass spectrometry analysis of the antibody and ADIBO functionalized antibody

Matrix-assisted laser desorption/ionization time-of-flight/time-of-flight tandem mass spectrometry (MALDI-TOF/TOF MS) was performed to evaluate antibody-ADIBO functionalization. The antibody solution was mixed with sinapinic acid dissolved in 50% acetonitrile/50% water containing 0.1% TFA (10 mg/ml) at a 1:1 ratio. Aliquots (1 μL) of each antibody solution were spotted onto MALDI plates and allowed to air dry completely at room temperature. Measurements were acquired in linear mode with an accelerating voltage of 25 kV. Molecular weights of the antibody alone and the ADIBO functionalized antibody were calculated as the average from 500-1000 laser shots following the standard MALDI-TOF/MS method used for protein analysis.

4.4 Determination of proteins concentration involving antibody and antigen

The concentration of protein sample was determined by measuring the absorbance at 280 nm, which is associated with threonine, tryptophan residue, or cystein-cystein disulfide bonds, using NanoDrop® 1000 spectrophotometer (Thermo Fisher Scientific Inc, Wilmington, USA). All concentration of protein was calculated by Beer-Lambert equation using each of extinction coefficients: 13.7 at 280 nm for a 1% (10 mg/mL) IgG solution and 1.0 at 280 nm for 0.1% (1 mg/mL) general protein solution involving antigen. The reliability of this system was verified by using accurately measured standard solutions.

4.5 Preparation of fluorescence labeled antigen

Recombinant human EtbB2 was modified using click chemicals for fluorescent dye labeling. A general synthetic procedure for clickable modified antigen was performed in two steps. Firstly, the antigen was conjugated to dibenzocyclooctyl N-hydroxysuccinimide (DBCO-NHS), and the DBCO conjugated antigens (Ag-DBCO) were then purified using a PD-10 column. Secondly, FNR-648-azide was mixed with Ag-DBCO in order to conjugate DBCO to the azide group using a click reaction. Using a 100 kDa centrifugal filter, fluorescently labeled antigen was washed with PBS 3 times at 4°C. The final volume was 0.2 mL and the concentration was determined using NanoDrop®.

4.6 Measurement of confocal laser scanning microscopy for cancer cells targeted by fluorescent NPs (QD^2)

Cells were fixed with 4% of paraformaldehyde, followed by nuclear staining using mounting solution containing DAPI (4',6-diamidino-2-phenylindole). Confocal laser scanning microscopy (CLSM; SP8 X, Leica, Wetzlar, Germany) was used to obtain fluorescence images of cells targeted by anti-HER2 fluorescent NPs (anti-HER2-QD^2). Excitation laser-lines for DAPI and anti-HER2-QD^2 were 405 nm. The DAPI signals were collected from 420 nm to 490 nm and the anti-HER2 QD^2 signals were collected from 610 nm to 650 nm, respectively. All obtained images were analyzed using the imaging process software provided by Leica (Leica Application Suite X, Leica, Germany).

5. *In Vivo* and *In Situ* Multiplexed Molecular Diagnosis using FRES for Breast and Colorectal Cancer

5.1 Establishment of cancer cell lines

The human breast cancer cell line MDA-MB-231/HER2, a HER2-expressing variant of MDA-MB-231 (ATCC, Manassas, VA), and human colorectal adenocarcinoma cell line (HT29), which is known to express EGFR and VEGF[82], were acquired from the Korean Cell Line Bank (KCLB, Seoul, Korea). Cancer cells were cultured with Dulbecco's modified Eagle's medium (DMEM; Invitrogen, Grand Island, NY, USA) containing 10% Fetal Bovine Serum and 1% penicillin/streptomycin. Cells were incubated in a humidified atmosphere of 5% CO_2 at 37°C and passaged with 0.125% trypsin. Then, those cancer cells were harvested.

5.2 Reverse transcriptase-polymerase chain reaction (RT-PCR)

RNA was isolated by Trizol reagent (Invitrogen, Carlsbad, CA) in MDA-MB-231/HER2 cells, and cDNA was synthesized following the protocol (cDNA Synthesis Master Mix; GenDEPOT, Barker, TX). For PCR, the initial denaturation of 5 minutes at 94°C, 30 amplification cycles of 30 s at 94°C, 30 s at 60°C, and 30 s at 70°C, and 7 minutes extension at 72°C was performed for HER2, EGFR and β-actin. The products of RT-PCR were resolved by 2% agarose gel electrophoresis. The DNA bands corresponded to HER2 and EGFR transcripts with 220 and 637 base pairs (bp), respectively.

5.3 Western blot analysis

Cells were lysed in radio-immunoprecipitation assay (RIPA) buffer (Sigma, St. Louis, MO, USA) containing protease inhibitor cocktail (Roche Diagnostics, Basel, Switzerland), and subsequently cleared *via* centrifugation (14,000 ×g for 20 min at 4°C). Protein concentrations were determined using BCA protein assay kits (Thermo Scientific, Rockford, IL, USA). Approximately 30 μg of protein was mixed with 4× polyacrylamide gel electrophoresis sample buffer, boiled at 70°C for 10 min, separated by gradient (4 – 12%) polyacrylamidegel electrophoresis, and transferred to nitrocellulose membranes (Invitrogen Grand Island, NY, USA). Membranes were blocked with 5% skim milk in Tris-buffered saline (20 mM Tris, 137 mM sodium chloride, and 0.1% polysorbate 20) for 1 h at room temperature, and then incubated overnight at 4°C with the following primary antibodies: rabbit monoclonal HER2 and EGFR antibody (1:1,000 dilution; Cell Signaling, Danvers, MA, USA), rabbit polyclonal VEGF antibody (1:1,000 dilution; Abcam, Cambridge, MA, USA) and mouse monoclonal β-actin antibody (1:5,000 dilution; Sigma-Aldrich, St. Louis, MO, USA). After membranes were washed with Tris-buffered saline three times, they were incubated with a secondary anti-rabbit/anti-mouse horseradish peroxidase–conjugated antibody (1:2,000 dilution; Santa Cruz Biotechnology, Santa Cruz,

CA, USA) for 2 h, and enhanced chemiluminescence detection reagent (Thermo Scientific, Rockford, IL, USA). Signal intensities were then measured using an LAS-3000 imaging system (Fuji Film, Tokyo, Japan).

5.4 *In vitro* specific targeting on the cancer cell line

The human colorectal cancer cells (HT29, 1×10^5 cells/well) in a Lab-tek glass chamber slide (Nalge Nunc International) were incubated for 24 h at 37°C and cells fixed with 4% paraformaldehyde (Wako, Osaka, Japan) for 20 min, and washed with PBS three times. Subsequently, the cells were mixed with the anti-EGFR antibody conjugated F-SERS dots solution (0, 5, 10, 20, 40, 60, 80 and 100 μg) for 10 min at 25°C. After washing the slide several times with PBS solution containing 0.1 wt% tween-20 and PBS solution, the chamber slides were washed with PBS and deionized water for several times and measured by the FRES for 3 min.

5.5 Modeling of orthotopic breast cancer xenografts

All animal studies were conducted according to the protocols approved by the Institutional Animal Care and Use Committee of the Seoul National University. The 5×10^6 cells of prepared MDA-MB-231/HER2 were injected in the mammary fat pad of a female BALB/c nude mouse (OrientBio, Sungnam, Korea). A 30-gauge needle was used for injection. The injection volume was 0.1 mL containing tumor cells and medium/matrigel complex with 50% dilution. Tumor growth was evaluated for 14 days, and an *in vivo* tumor imaging was performed when the largest tumor diameter reached 1-1.5 cm.

5.6 Modeling of orthotopic colorectal cancer (CRC) xenografts

Six-week-old male BALB/c nude mice were obtained from Orient Bio, Inc. (Seoul, Korea) and housed in a specific, pathogen-free environment. Before each tumor cell injection, mice were anesthetized with an intramuscular injection of 200 μL of 0.5% zoletil 50 (tiletamine-zolazepam; Virbac S.A., Carros, France) and 0.2% xylazine (Rompun; Bayer, Leverkusen, Germany) solution (1:1). Using a 30-gauge needle, a 0.1 mL volume of complex (containing tumor cells at a 1:1 ratio in medium/matrigel) was injected in to the posterior colorectal wall *via* the anus.[83, 84] Tumor growth was investigated for two weeks for the 1×10^7 of HT29 cells injection groups, and for one week for the 5×10^6 of HT29 cells injection group.

5.7 Validation of *in vivo* specific targeting by intraoperative multiplexed F-SERS dots

For *in vivo* studies, all mice were initially anesthetized with an intramuscular injection of 200 μL of 0.5% zoletil 50 (tiletamine-zolazepam; Virbac S.A., Carros, France) and 0.2% xylazine (Rompun; Bayer, Leverkusen, Germany) solution (1:1).

For an intraoperative multiplexed imaging by targeted F-SERS dots on breast cancer xenograft models, the anti-HER2 antibody-conjugated F_{AF610}-$SERS_{RITC}$ dots (anti-HER2-F_{AF610}-$SERS_{RITC}$ dots) and anti-EGFR antibody-conjugated F_{AF610}-$SERS_{FITC}$ dots (anti-EGFR-F_{AF610}-$SERS_{FITC}$ dots) were prepared. After making a minimal (*ca.* 10 mm) skin incision and exposing the tumors, two types of the tumor surface were studied: the outer surface, from which it is assumed to identify the tumor on their surface, and the cut surface, from which it is assumed to find tumors at the resection margins. For the outer surface study, the F-SERS dots were sprayed on the tumor, whereas the F-SERS dots were sprayed after a 5-mm cutting for the cut surface study. To validate the specific targeting ability of the F-SERS dots, the tumor site was pre-treated with blocking antibodies (monoclonal antibodies against HER2 or EGFR). For either single target blocking, HER2 or EGFR, the tumor sites were treated with 1 mg of anti-HER2 or anti-EGFR antibodies (injection

volume, 200 μL of 5 mg/mL antibodies in PBS). For the dual target blocking, a tumor site was treated with 1 mg of mixture of the anti-HER2 and anti-EGFR antibodies. After 10 minutes, these tumor sites were washed with PBS, and 100 μg (volume = 20 μL, estimated concentration: 0.28 - 0.63 μg/mm^2) of the targeting F-SERS dots (anti-HER2-F_{AF610}-$SERS_{RITC}$ dots and anti-EGFR-F_{AF610}-$SERS_{FITC}$ dots, concentration = 5 mg/ml, respectively) were sprayed on the surface of tumor sites using a micro-pipette (AxyPet™ Single-channel pipettor, Axygen, USA). After 10 minutes incubation, the F-SERS dots-sprayed tumors were washed with PBS three times (200 μL at each time) to remove unbound F-SERS dots using a micropipette. Subsequently, real-time fluorescence images and Raman spectra at the tumor sites were obtained using the FRES. The antibodies pre-treatment, F-SERS dots treatment, and FRES probe insertion were performed on the same surface of the tumor.

To validate feasibility of the FRES as an endoscopic molecular diagnostic tool, each 100 μg of anti-EGFR-F_{AF610}-$SERS_{RITC}$ dots and anti-VEGF-F_{AF610}-$SERS_{FITC}$ dots were sprayed onto the lumen of the colon through the anus. After 10 min of incubation, antibody-conjugated F-SERS dots treated area was washed with 300 μL of PBS five times. The targeted area was investigated for 3 min by inserting an optical fiber bundle probe of the FRES in the colon through the anus of tumor-implanted and normal mice.

5.8 Pathologic evaluation of colorectal cancer xenografts

Immunohistochemistry (IHC) for EGFR and VEGF was carried out on formalin-fixed, paraffin-embedded serial sections cut at 3 μm and dried at 37°C overnight. Immunostaining was performed using an avidin–biotin complex (ABC) procedure, including heat-induced epitope and enzymatic antigen retrieval procedures. IHC for EGFR (C74B9 1:50; Cell Signaling Technologies, Beverly, MA, USA) was performed according to manufacturer's instructions.

5.9 Measurement of confocal laser scanning microscopy for tumor targeted by F-SERS dots

Tumors were excised and fixed with 4% of paraformaldehyde, followed by staining nuclei using DAPI (4',6-diamidino-2-phenylindole). Confocal laser scanning microscopy (CLSM; LSM 510 META, Carl Zeiss, Jena, Germany) was used for fluorescence signal detection. Excitation laser-lines for F-SERS dots and DAPI signals were 610 nm and 405 nm, respectively. Fluorescence signals of Alexa Fluor 610 (F_{AF610}) from F-SERS dots were detected and visualized. Data were analyzed with LSM Image Examiner software (Carl Zeiss).

Results and Discussion

1. Fluorescence-Raman Dual Modal Endoscopic System (FRES)

1.1 Strategy for *in vivo* and *in situ* endoscopic multiplexed molecular diagnostics using FRES

The dual modal FRES was developed with the following imaging and targeting strategies: (i) simultaneous detection of dual mode (fluorescence and Raman scattering) signals from dual modal nanoprobes in order to diagnose pathological lesions based on the strategy of using fluorescence images to track the target and Raman spectra to identify specifically targeted biomolecules; and (ii) utilization of optical fiber bundles, which can access *in vivo* suspicious lesions with a non-/minimally invasive procedure in conjunction with conventional endoscopy for intraoperative real-time molecular diagnostics. Figure 8 shows a schematic overview of an *in vivo* molecular diagnostic procedure where an optical fiber bundle probe could access the vicinity of a suspicious lesion in a minimally invasive manner. To target biomolecules expressed in a cancerous tissue, the antibody-conjugated F-SERS dots were sprayed directly on the surface of the lesion. The F-SERS dots, as tumor targeting agents, were able to simultaneously emit fluorescence and SERS signals using a single excitation source. After washing the unbound F-SERS dots, the targeted area was assessed by FRES to obtain real-time fluorescence images and Raman spectra. As the fluorescence signals were produced from the F-SERS dots, the location of the target biomolecules could

be tracked easily while the types of target biomolecules could be identified by the SERS signals. Through this *in vivo* multiplexed molecular diagnostic process, the pathological condition of suspicious lesion at the molecular level could be intraoperatively identified during routine endoscopic examination; the accurate and reliable diagnosis for specific cancer at an early stage could be possible. Afterwards, the proper and personalized therapy could be achieved at an early stage of cancer.

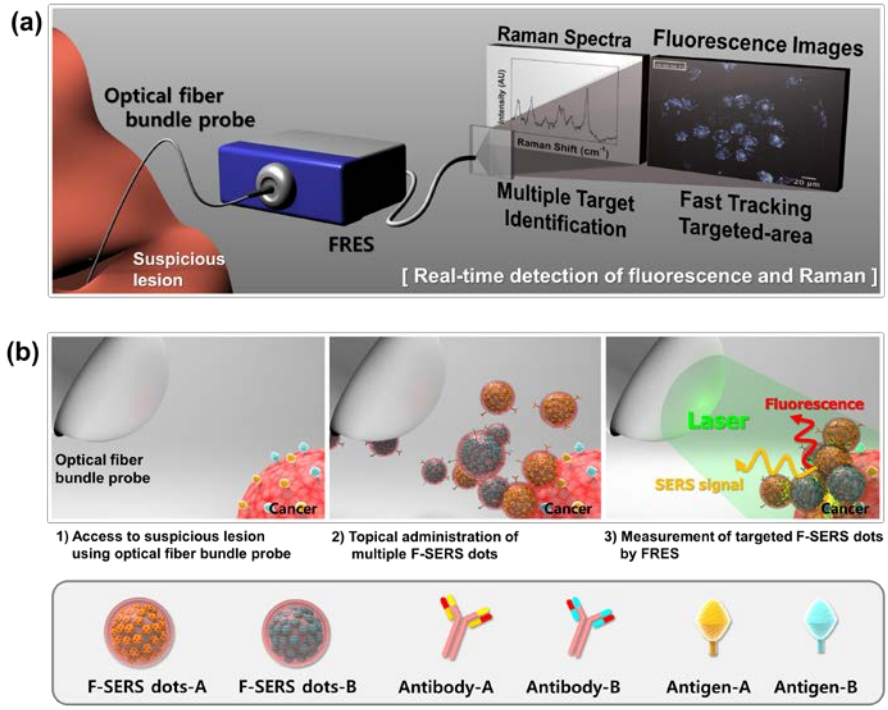

Figure 8. Schematic illustration of real-time multiplexed imaging using the FRES. (a) The mode of dual modal detection with fluorescence and Raman scattering. The real-time fluorescence imaging tracks the locations of the probe-targeted areas, and a concurrent SERS spectral analysis identifies the species of targets. (b) Illustration of the *in vivo* multiplexed molecular imaging procedure: First, access to a suspicious lesion *via* optical images; second, the spray-and-mix multiple F-SERS dots for topical administration; third, a multiplexed measurement of the targeted F-SERS dots with the FRES.

1.2 Synthesis and characterization of the F-SERS dots

As tumor targeting agents, the fluorescence-SERS dual modal nanoprobes (F-SERS dots) were synthesized to emit fluorescence and SERS signals simultaneously using a single excitation source. As shown in Figure 7 and 9(a), the F-SERS dots consisted of silica nanosphere as a supporting material, Raman-labeled silver nanoparticles for SERS signals, and a fluorescence dye-conjugated outer silica shell for fluorescence signals, with an overall diameter of *ca.* 240 nm (Figure 10). As shown in Figure 11, an extinction band of the synthesized F-SERS dots was observed ranging broadly from 350 to 600 nm. The broadening of plasmonic extinction band can be interpreted by plasmonic couplings among silver nanoparticles on the surface of silica nanosphere. For SERS signals, the RITC and FITC compounds were utilized as Raman-label compounds. These Raman-label compounds were adsorbed on the silver nanoparticles using an isothiocyanate functional group. Additionally, AF610 was utilized as a fluorescence dye for the fluorescence signal. These F-SERS dots were further conjugated with each antibody for specific binding to a target in breast cancer or colorectal cancer xenografts, respectively: anti-HER2 and anti-EGFR antibodies for breast cancer (anti-HER2-F_{AF610}-$SERS_{RITC}$ dots and anti-EGFR-F_{AF610}-$SERS_{FITC}$ dots), anti-EGFR and anti-VEGF antibodies for colorectal cancer (anti-EGFR-F_{AF610}-$SERS_{RITC}$ dots and anti-VEGF-F_{AF610}-$SERS_{FITC}$ dots). To confirm their simultaneous emission of the fluorescence and the SERS signal, the F-SERS

dots were examined on a glass slide by a micro-Raman spectrometer (LabRam 300, JY-Horiba). The distinct bands of each F-SERS dot were clearly observed (Figure 9(b)) and well-matched with the results in the literature.[85, 86] Furthermore, the fluorescence signal of AF610 at *ca.* 625 nm was apparent in both of the F_{AF610}-SERS dots.

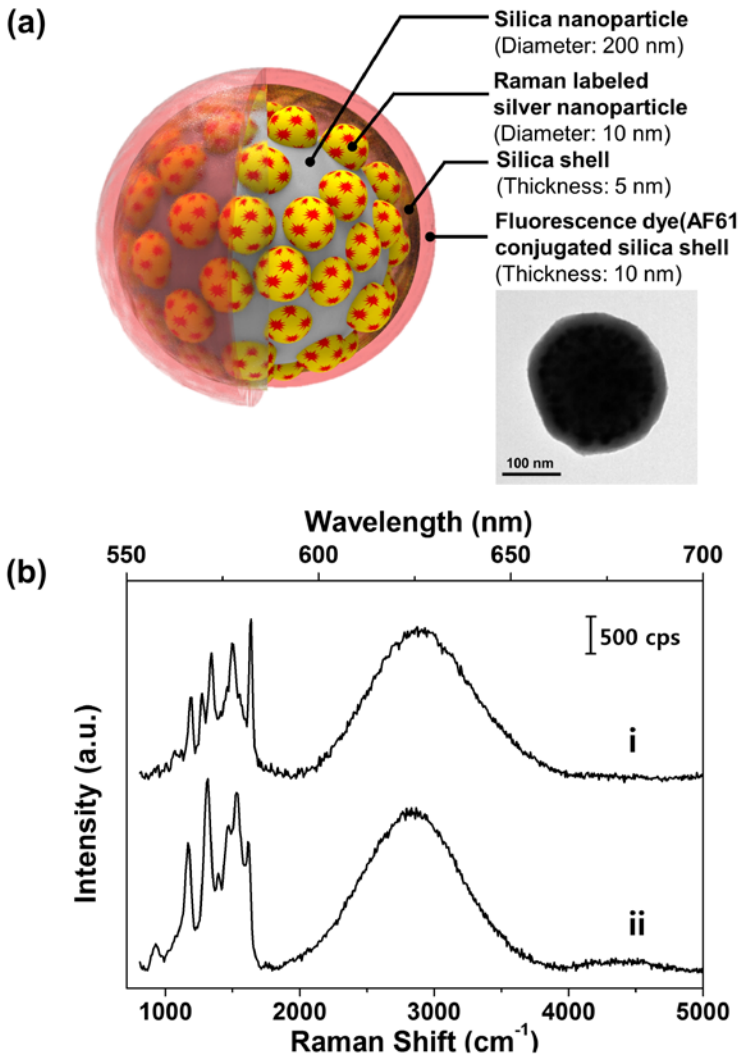

Figure 9. The characterization of F-SERS dots. (a) Illustration of composition of F-SERS dots and transmission electron microscopy (TEM) image of a F_{AF610}-$SERS_{RITC}$ dots. (b) The Raman spectra of F-SERS dots labeled with two different kinds of Raman compounds using micro-Raman spectroscopy: i) F_{AF610}-$SERS_{RITC}$ dots and ii) F_{AF610}-$SERS_{FITC}$ dots. All F-SERS dots were coated with an AF610 fluorescence dye conjugated silica shell. Raman spectra were obtained with 532 nm laser power of 2.7 mW, acquisition time of 1 s, and diffraction grating of 300 grooves/mm.

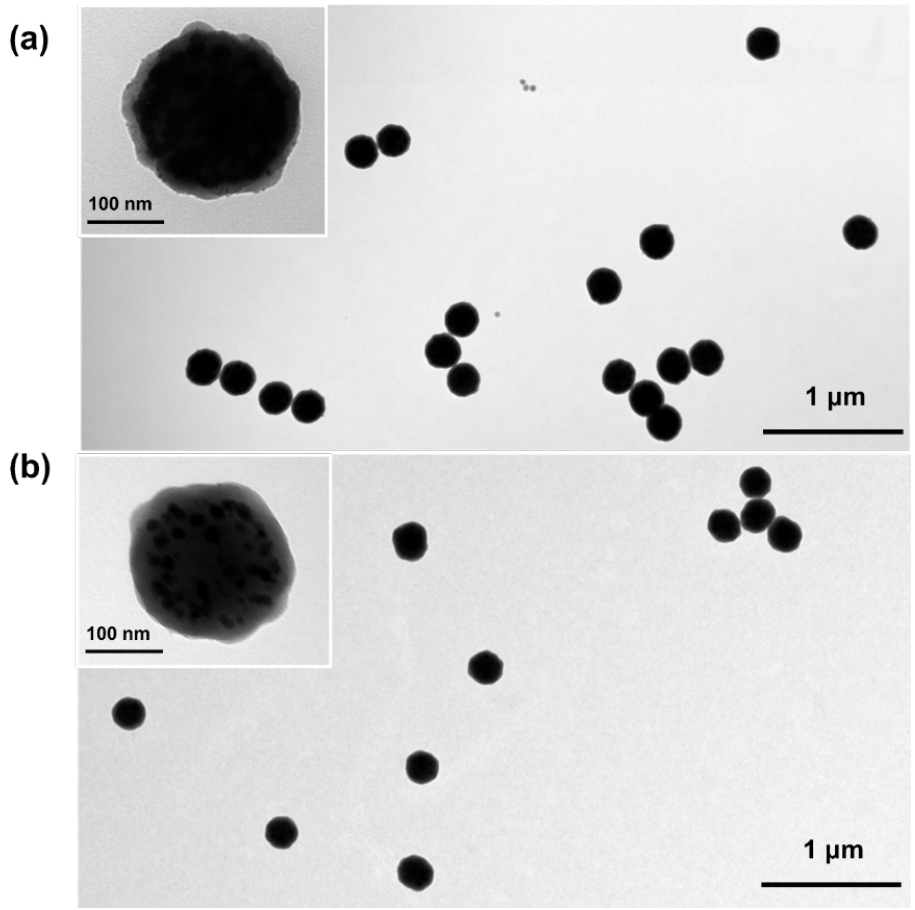

Figure 10 Transmission electron microscopy (TEM) images of (a) F_{AF610}-$SERS_{RITC}$ dots and (b) F_{AF610}-$SERS_{FITC}$ dots. The insets are highly magnified images of each F-SERS dot.

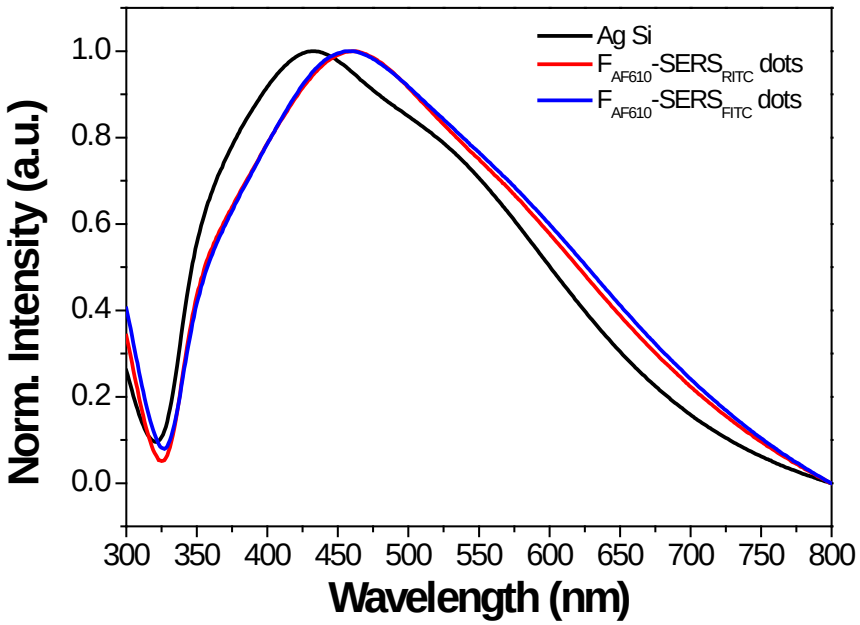

Figure 11. UV-Visible extinction spectra of Ag NPs-embedded silica nanoparticles (Ag Si), F_{AF610}-$SERS_{RITC}$ dots, and F_{AF610}-$SERS_{FITC}$ dots

1.3 Design of the FRES

The FRES simultaneously detected both fluorescence and Raman signals in real-time, capitalizing on an intense fluorescence signal for an acute detection of the target location and on a narrow bandwidth of the Raman scattering for multiplexed analysis. In *in vivo* dual-modal endoscopic detection, the FRES consisted of three components, as shown in Figure 12(a): i) a dual-axis laser-scanning unit to allow for light incidence to and light collection from an entire optical fiber bundle; ii) a separation unit for fluorescence and SERS signals to simultaneously detect both signals from the targeted F-SERS dots; and iii) two detection units that consisted of an avalanche photodiode for fluorescence imaging and a spectrometer equipped with a CCD camera for SERS spectral measurements. As an excitation source, a 532 nm laser was utilized to generate SERS-effective Raman signals of the F-SERS dots and simultaneously excite the fluorescence dyes of the F-SERS dots. The spectral window was divided into two sections (Figure 12(b)): One for the fluorescence signals above 2000 cm^{-1} from a 532 nm laser-line, and the other for the Raman scattering signals from 1250 to 2000 cm^{-1} to minimize an optical noise from the optical fiber. The paths of the optical beams from the fluorescence and Raman signals were completely separated and independently detected, and thus the FRES enabled simultaneous, real-time detection of the fluorescence images and Raman spectra with a single laser-line excitation (Figure 13).

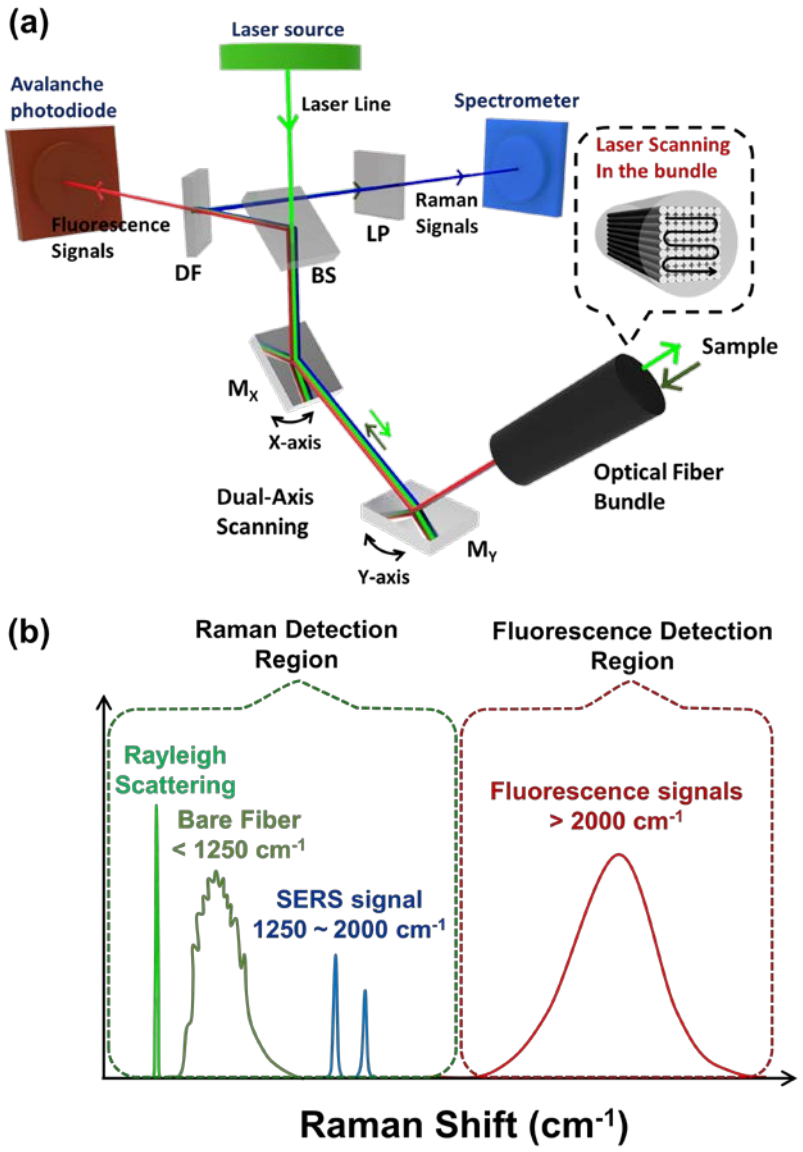

Figure 12. (a) Schematic diagram of the optical beam path of FRES. B.S.: beam splitter, M_X: oscillating mirror for X-axis, M_Y: oscillating mirror for Y-axis, D.F.: dichroic filter, and L.P.: long pass edge filter. (b) Illustration of the spectral design sectioning the ranges of the collected signal from the sample. The collected signal contains four different kinds of signals: laser line, intrinsic Raman scattering of the optical fiber, SERS signal, and fluorescence signal.

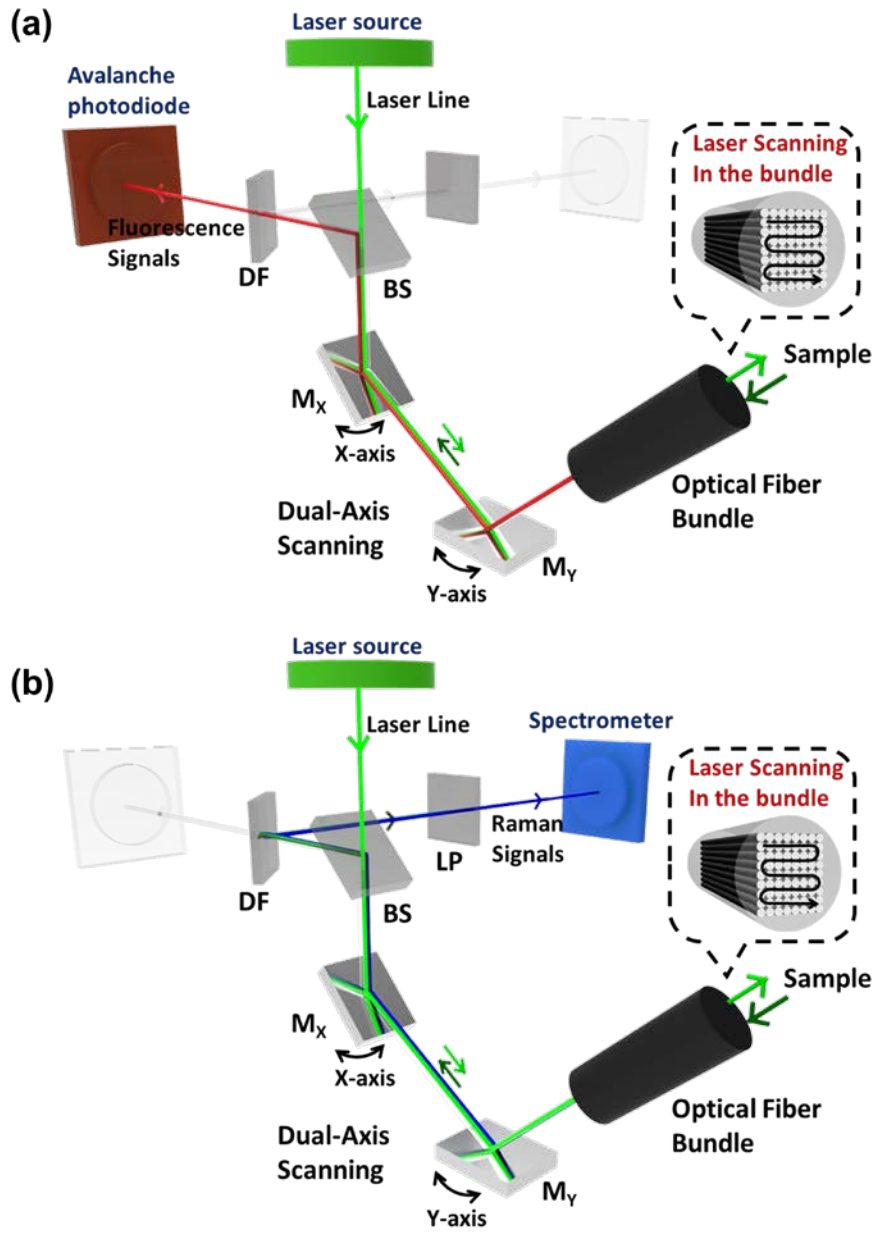

Figure 13. Schematic diagram of the optical beam path for (a) fluorescence imaging, and (b) SERS detecting. BS: Beam Splitter, M_X: Oscillating mirror for X-axis, M_Y: Oscillating mirror for Y-axis, DF: Dichroic Filter, and LP: Long-pass edge filter.

1.4 Evaluation of fluorescence endomicroscopic imaging ability of FRES in real-time

Signals were collected through a dual-axis laser-scanning unit that was composed of two oscillating mirrors for real-time imaging. The excitation laser lights sequentially illuminated into *ca.* 100,000 individual optical fibers in the entire fiber bundle optical guide through two orthogonally oscillating mirrors at 4 kHz. The signals were collected from the individual optical fibers using an identical optical pathway as the excitation light, and they were then separated into the fluorescence and the Raman signal by a dichroic filter. At this stage, each point from the individual optical fibers collecting fluorescence signals were synchronized with each pixel of the processed fluorescence image. This allowed the FRES to rapidly construct the fluorescence images (12 frames/s) that enabled real-time tracking of the tumor-targeting F-SERS dots in a large area (Figure 14). For simultaneous, dual-modal detection, a fluorescence dye was used for the F-SERS dots, which have a maximum emission wavelength over 593 nm when the fluorescence dye was excited by a 532 nm laser-line. AF610 was chosen among four dye candidates - AF568, AF594, AF610, and AF633 - since it showed the lowest background noise in the Raman detection range and sufficiently intense fluorescence signals to construct images in the fluorescence detection range (Figure 15).

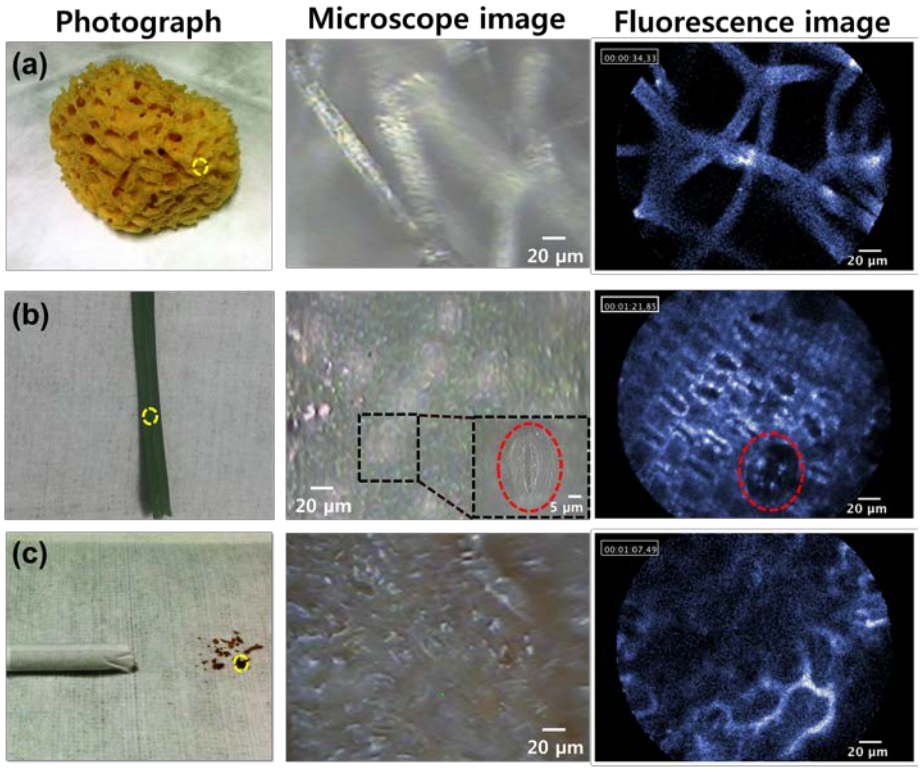

Figure 14. Demonstration of fluorescence endomicroscopic imaging ability of our developed system using optical fiber bundle probe. (a) Natural sponge, (b) leaf, and (c) cigarette. All fluorescence images were obtained by their auto-fluorescence signal and represented by false color.

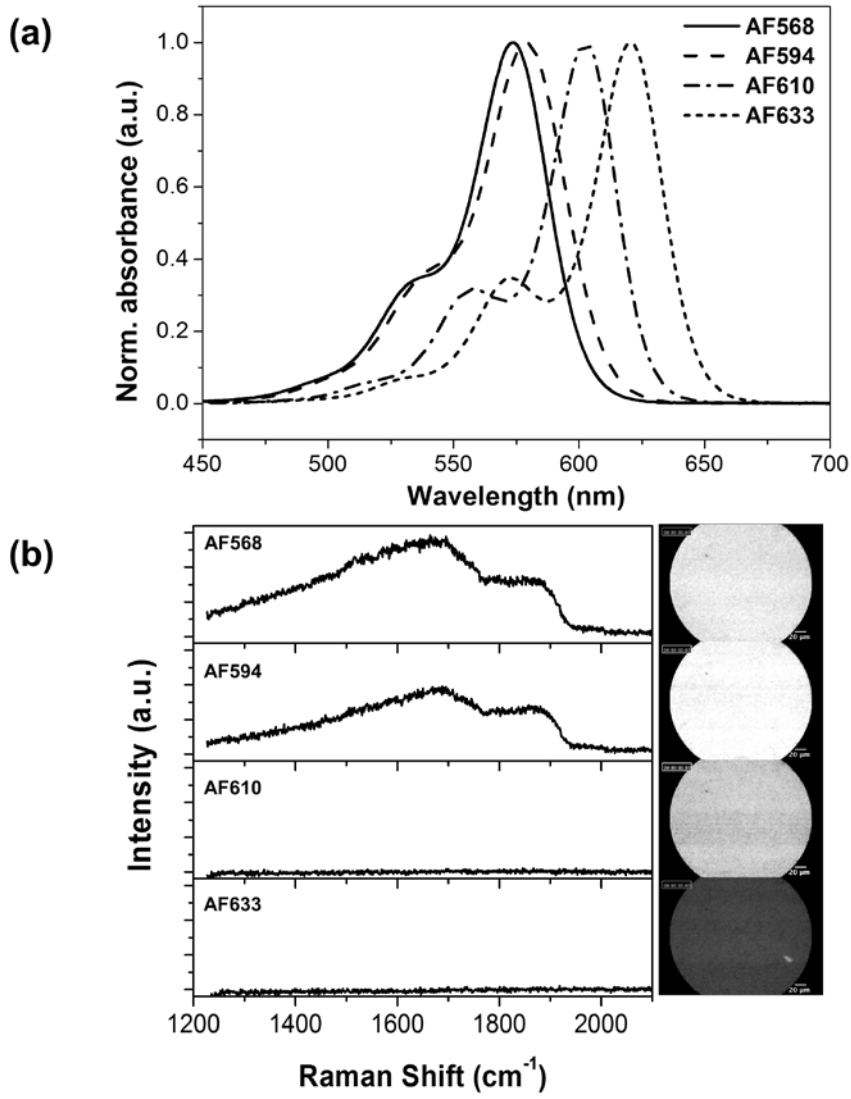

Figure 15. (a) The absorption spectra of candidate dye for F-SERS dots: AF568, AF594, AF610, and AF633 at 0.8 mM. (b) The fluorescence images and SERS spectra of them measured by FRES. All fluorescence images were obtained by FRES with real-time. The Raman spectra were taken by FRES with laser power of 2.7 mW and acquisition time of 1s.

1.5 Evaluation of Raman signal detecting ability of the FRES

The reflected light from a fluorescence-passing filter (below 2000 cm^{-1} from the laser-line) contained Rayleigh and Raman scattering light. The light was then passed through an edge filter to block Rayleigh scattering before entering a spectrometer equipped with a CCD detector for Raman detection (Figure 13(b)). As the strong intrinsic Raman signals below 1250 cm^{-1} were produced by optical fibers, a spectral window with a low background noise was selected, ranging from 1250 to 2000 cm^{-1} (Figure 16). For Raman-label compounds in SERS detection, the RITC and FITC dye molecules were used since they have strong and distinct bands without any spectral overlap in the SERS detection range. The Raman detecting ability of the FRES was evaluated by comparing the conventional Raman spectroscopy in terms of signal-to-noise ratio and spectral resolution. Figure 17 shows that the FRES exhibits similar Raman detecting performance in comparison to conventional confocal Raman system. (LabRam 300, JY-Horiba)

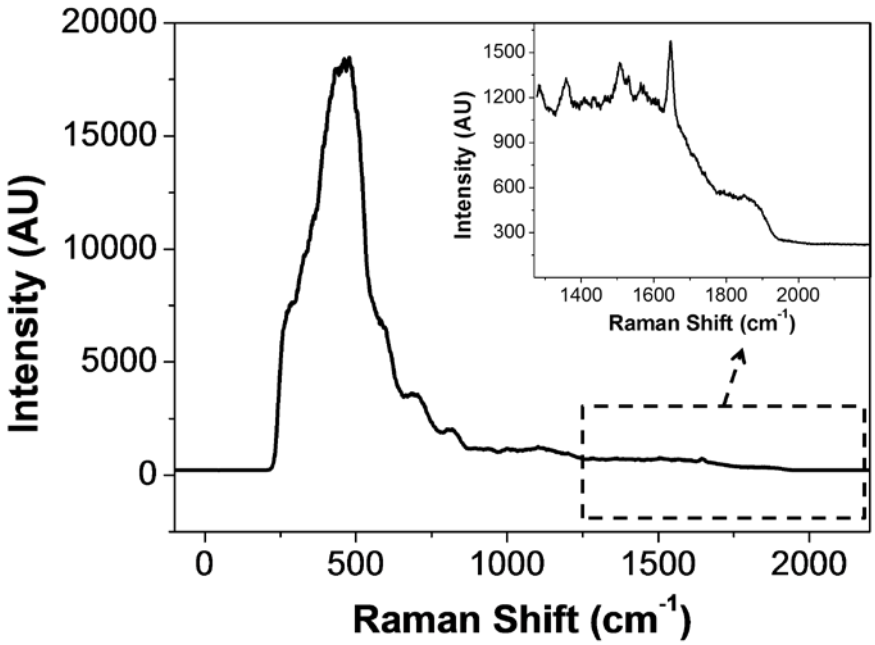

Figure 16. The Raman spectrum of optical fiber bundle probe with F_{AF610}-$SERS_{RITC}$ dots using the FRES. The inset is an enlarged spectrum of SERS detectable range; 1250 - 2200 cm^{-1}, which has low background noise signal.

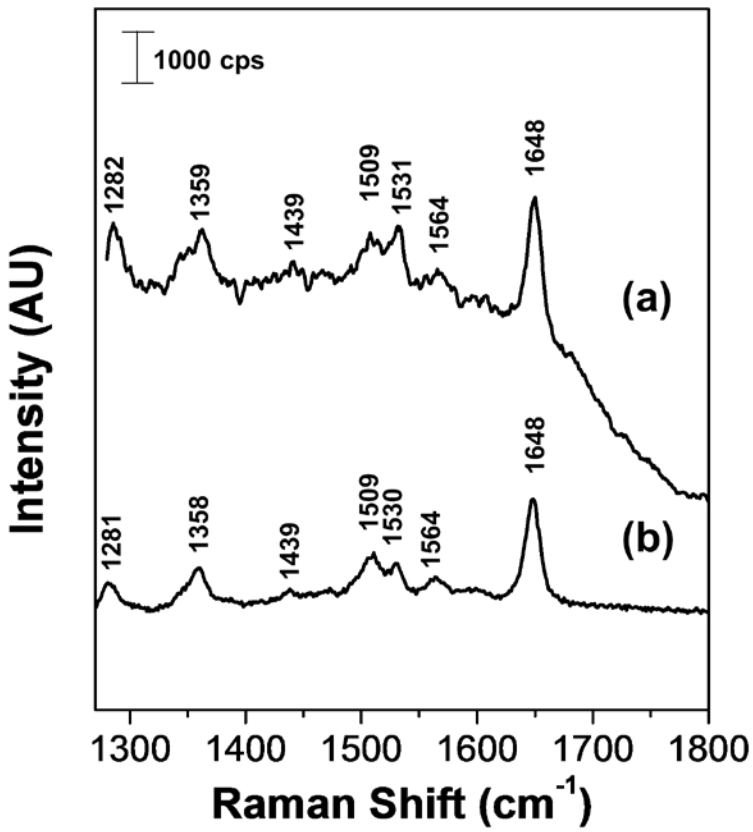

Figure 17. Raman spectra of F_{AF610}-$SERS_{RITC}$ dots on the slide glass using (a) the FRES and (b) standard micro-Raman spectroscopy in order to evaluate Raman detecting ability in terms of signal-to-noise ratio and spectral resolution. The Raman spectrum was taken with a laser power of 2.7 mW and acquisition time of 1 s using the FRES; the Raman spectrum was taken with a laser power of 4.3 mW and acquisition time of 1 s using micro-Raman spectroscopy (LabRam 300, JY-Horiba).

1.6 Evaluation of simultaneous fluorescence and Raman signals detecting ability of FRES

To evaluate the ability of the dual modality detection of the F_{AF610}-$SERS_{RITC}$ and F_{AF610}-$SERS_{FITC}$ dots, each F-SERS dots and their mixture in PBS were prepared separately in a conical tube, and their fluorescence and Raman signals were measured simultaneously by FRES. Figure 18 shows fluorescence images and Raman spectra simultaneously obtained by FRES. The fluorescence images of each kind of F-SERS dots and their mixture exhibited bright small dots were clearly distinguished from a background image (Figure 18(a)). In the Raman spectra, distinct bands of F-SERS dots could be identified from the mixture along with those from the individual F-SERS dots: 1285 and 1648 cm^{-1} bands for the RITC coded F-SERS dots; 1324 and 1633 cm^{-1} bands for the FITC coded F-SERS dots (Figure 18(b)). In contrast, the fluorescence images and Raman spectra did not show any signals from the F-SERS dots in PBS.

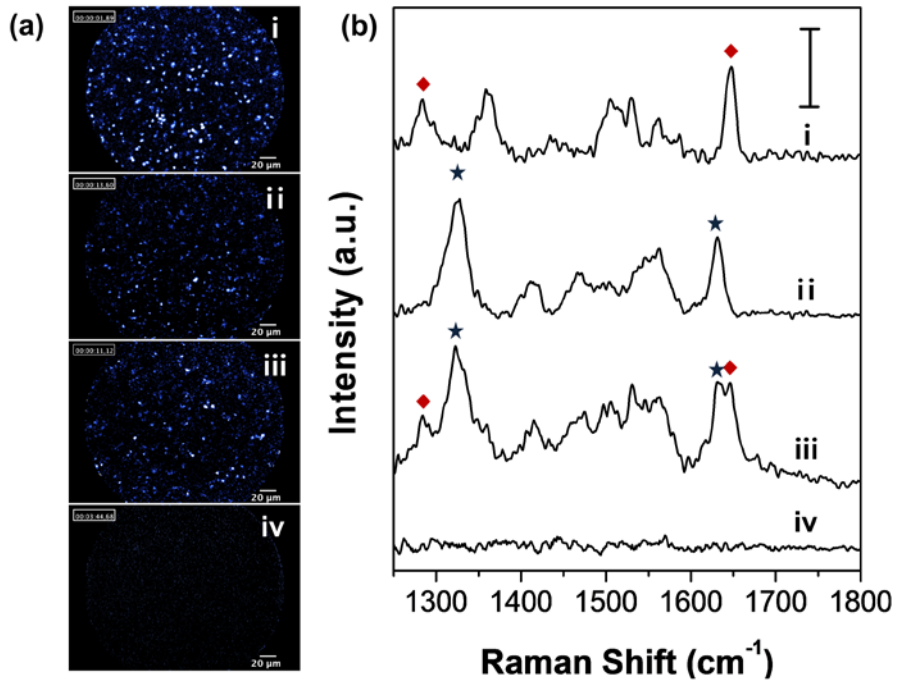

Figure 18. (a) Fluorescence images and (b) Raman spectra of two different kinds of F-SERS dots and phosphate buffer solution (PBS): i) F_{AF610}-$SERS_{RITC}$ dots(◆) and ii) F_{AF610}-$SERS_{FITC}$ dots(★), iii) a mixture of the two types and iv) PBS as solvent in a conical tube. All fluorescence images and Raman spectra were obtained using the FRES at laser power of 2.7 mW. All fluorescence images were represented by false color. The SERS spectra were integrated for 1 s. Scale bar: 100 cps

1.7 Evaluation of sensitivity of the FRES

The intensities of the fluorescence and Raman scattering of the F_{AF610}-$SERS_{RITC}$ dots in different concentrations (152 to 0.3 pM in PBS) were measured in a conical tube by FRES to evaluate their sensitivity. Fluorescence images and Raman spectra were obtained from each concentration of the F_{AF610}-$SERS_{RITC}$ dots at a laser power of 2.7 mW. The fluorescence images in Figure 19(a) show that the number of bright dots decreased with a decreasing concentration of the F_{AF610}-$SERS_{RITC}$ dots. In the Raman spectra (Figure 19(b)), the SERS intensity of the F_{AF610}-$SERS_{RITC}$ dot peak at 1648 cm^{-1} also decreased linearly as the concentration of the probe decreased ($R^2 = 0.99$). The minimal detectable concentration was approximately 1 pM for the F_{AF610}-$SERS_{RITC}$ dots with an optical fiber bundle probe possessing a 240 μm-field of view and a 10 μm-optical sectioning.

The FRES exhibited high sensitivity to detect a low concentration of F-SERS dots as tumor targeting agents (as low as 1-pM). This detection limit showed much greater sensitivity than that of other previously reported Raman-based fiber optic devices that relied only on intrinsic Raman scattering.[24, 32, 33] This feature met the sensitivity standard to be used as a clinical diagnostic tool.[25, 40] However, although small molecules like folate could evade reticuloendothelial system after intravenous administration,[28] the nanoparticle-based targeting agents accumulated in the liver and spleen by a mononuclear phagocytic system in an intravenous injection of nanoparticles

for *in vivo* targeting.[39, 87-90] By utilizing the direct topical administration of the tumor-targeting probe, the FRES was able to circumvent major limitations from the accumulation of nanoparticles, such as potential toxicity and low targeting efficiency. Since topically administered targeting agents can reach and bind to their targets more effectively than those from intravenous injection, the administration method used in FRES potentially increases the targeting efficiency.[25, 29]

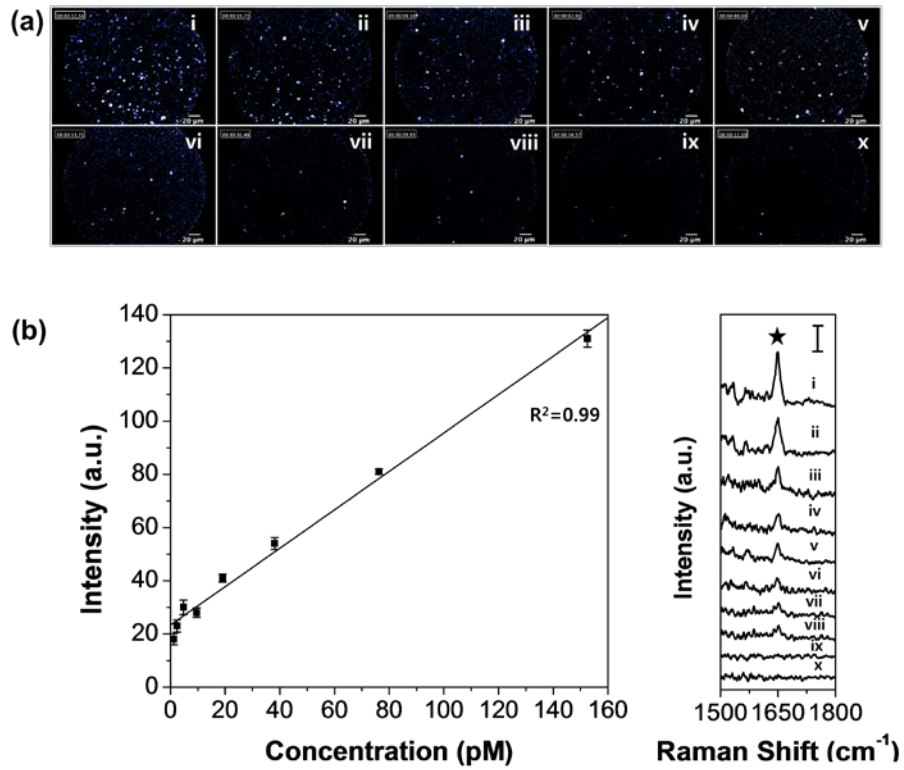

Figure 19. Evaluation of the detection limit of fluorescence and SERS signal using FRES. (a) Fluorescence images of different concentrations of F_{AF610}-$SERS_{RITC}$ dots: i) 152, ii) 76, iii) 38, iv) 19, v) 10, vi) 5, vii) 2, viii) 1, ix) 0.5, and x) 0.3 pM, and (b) SERS intensity graph of the characteristic RITC band at 1649 cm^{-1}(★). Left side is the SERS spectra of different concentrations of F_{AF610}-$SERS_{RITC}$ dots. All fluorescence images were represented by false color. All Raman spectra were measured at laser power of 2.7 mW and acquisition time of 1 s. Scale bar: 50 cps

2. Highly Robust and Optimized Conjugation of Antibodies to Nanoparticles using Quantitatively Validated Protocols

2.1 Versatile and facile antibody conjugation strategy using copper-free click chemistry

Figure 20 shows the procedure for antibody-conjugation using azide-functionalized silica nanoparticles (NPs) and alkyne-functionalized antibodies for antibody-orientation control, high conjugation efficiency, and minimal denaturation of antibodies during conjugation for overall targeting efficacy. To control the orientation of the antibodies, the alkyne group was functionalized in the Fc region of the antibody by reacting the maleimide group in aza-dibenzocyclooctyne-maleimide (ADIBO-Mal) with the thiol group derived from the disulfide bonds in the Fc region of the antibody. As a counter-coupling reagent, an azide group was introduced on the surface of silica-encapsulated NPs *via* silane coupling between the hydroxyl group on the silica surface of the NPs and the silane group in N-[3-(Triethoxysilyl)propyl]-2-azidoacetamide (NTPA). Subsequently, the azide-functionalized NPs and ADIBO-conjugated antibodies were mixed in order to conjugate the antibodies with the silica surface of NPs at room temperature. Since two benzene rings are conjugated to a cyclooctyne in a single ADIBO molecule, it reacts easily with the azide functional group with high efficiency and reproducibility *via* a strain-promoted alkyne-azide cycloaddition (SPAAC)

reaction, also known as a copper-free click reaction.[71] Additionally, these click-chemistry agents have bioorthogonality, since they do not react with endogenous biomolecules, resulting in high stability and biocompatibility of conjugation in biological conditions.

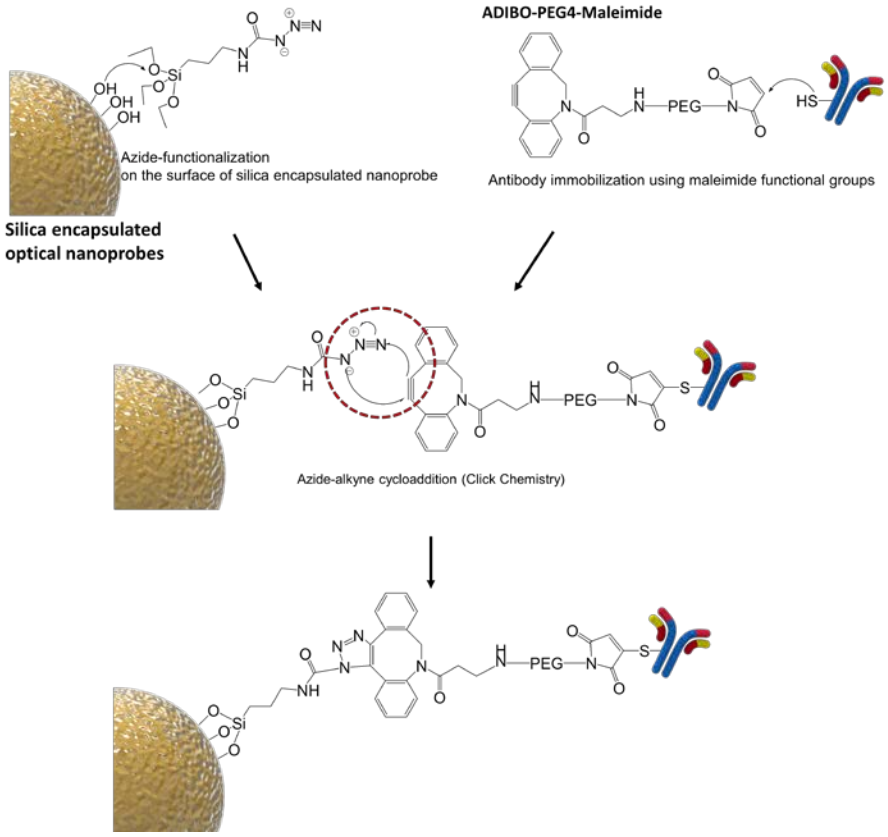

Figure 20. Schematic illustration of the versatile and oriented antibody immobilizing strategy for silica encapsulated nanoparticles using click chemistry

2.2 Site-specific conjugation of ADIBO at the Fc region of antibody

In order to link the alkyne group efficiently to the site-specific thiol group in the Fc domain while retaining antibody activity, reduction of the disulfide bonds in the Fc domain was precisely controlled using 2-mercaptoethanol (2-ME).[80, 81, 91] As shown in Figure 21(a), by reducing the disulfide linkages in the general antibody, immunoglobin-G (IgG), four distinct products can be generated: A partially-reduced full-length antibody containing a thiol functional group (150 kD), a fragment cleaved in half (75 kD), a heavy chain (50 kD), and a light chain (25 kD). Among these products, only the former two can successfully bind a specific target, owing to intact binding sites (Fab) consisting of a heavy chain and a light chain. For this reason, to preserve the biofunctionality of the antibodies, the optimal reducing conditions were elucidated, in order to avoid excessive cleavage of disulfide linkages, by verifying the fragmentation of full-length IgG antibodies in various reducing conditions using sodium dodecyl sulfate polyacrylamide gel electrophoresis (SDS-PAGE) analysis of reduced antibodies. I recognized that the amount of both heavy and light chains also increased with an increase in reducing agents (Figure 21(b)). However, in reaction condition 1 (line 2 and 7, red-dashed rectangle in Figure 21(b)), no fragmentation was observed in the SDS-PAGE analysis. This result implies that all antibodies were functionalized efficiently with thiol groups at the hinge site in the Fc region of

the IgG antibody, without the denaturing of antibody activity. Subsequently, the site-specific thiol groups were conjugated to the maleimide group possessing ADIBO. The orientation of this site-specific ADIBO-conjugated antibody in the Fc region is controlled when linked to the substrate surface, resulting in a much higher binding activity compared with random oriented antibody conjugation methods.[60, 61]

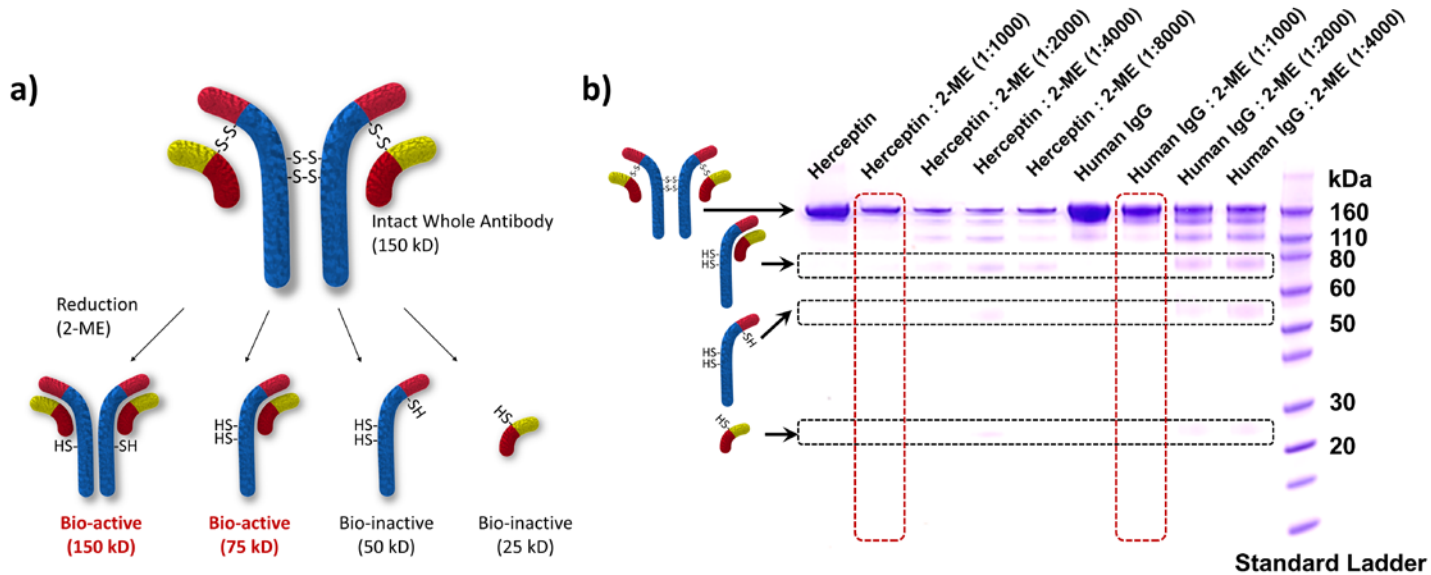

Figure 21. The optimization of the reducing conditions for antibody conjugation with ADIBO using a site-specific thiol functional group in the antibody. (a) Illustration of the fragmentation scenario by cleaving the disulfide bonds in the antibody. (b) SDS-PAGE analysis of antibody fragmentation with various ratios of the antibody to reducing agents: 1:1000, 1:2000, 1:4000, and 1:8000. The initial reducing condition (antibody:2-ME = 1:1000) was 4 μL of 0.3 M EDTA, 4 μL of 1 M sodiumbicabonate buffer, and 5 μL of β-mercaptoethanol (2-ME) in 500 μL PBS solution.

2.3 Confirmation of functional modification of both silica NPs (SiNPs) and antibodies

To evaluate the functionalization of both silica NPs (SiNPs) and antibodies, radio thin-layer chromatography (TLC) analysis was performed. The azido-functionalized SiNPs were conjugated to radio-labeled ADIBO containing 1,4,7-triazacyclononane-N,N',N''-triacetic acid (NOTA). Independently, the ADIBO functionalized antibodies were reacted with the radio-labeled azido-NOTA. As shown in Figure 22, once mixed with click chemistry agents containing NOTA and the azido-functionalized SiNPs or ADIBO-functionalized antibodies, the peak of NOTA shifted towards the starting position, which is attributed to the increased weight of NOTA due to the conjugation of heavy SiNPs or antibodies. From these results, I confirmed that both the SiNPs and antibodies were successfully functionalized. As a further confirmation, mass spectrometry analysis of the antibodies alone and the ADIBO-functionalized antibodies was performed using MALDI-TOF. Conjugation of the antibody to ADIBO-PEG4-maleimide increased its mass by *ca*. 2200 g/mol, which corresponds to the mass of the three molecules of ADIBO-PEG4-maleimide (molecular weight = 674.74 g/mol, Figure 23). According to the results of the mass spectrometry, not only was ADIBO functionalization of the antibodies confirmed, but also the quantitative amount of ADIBO molecules conjugated to a single antibody.

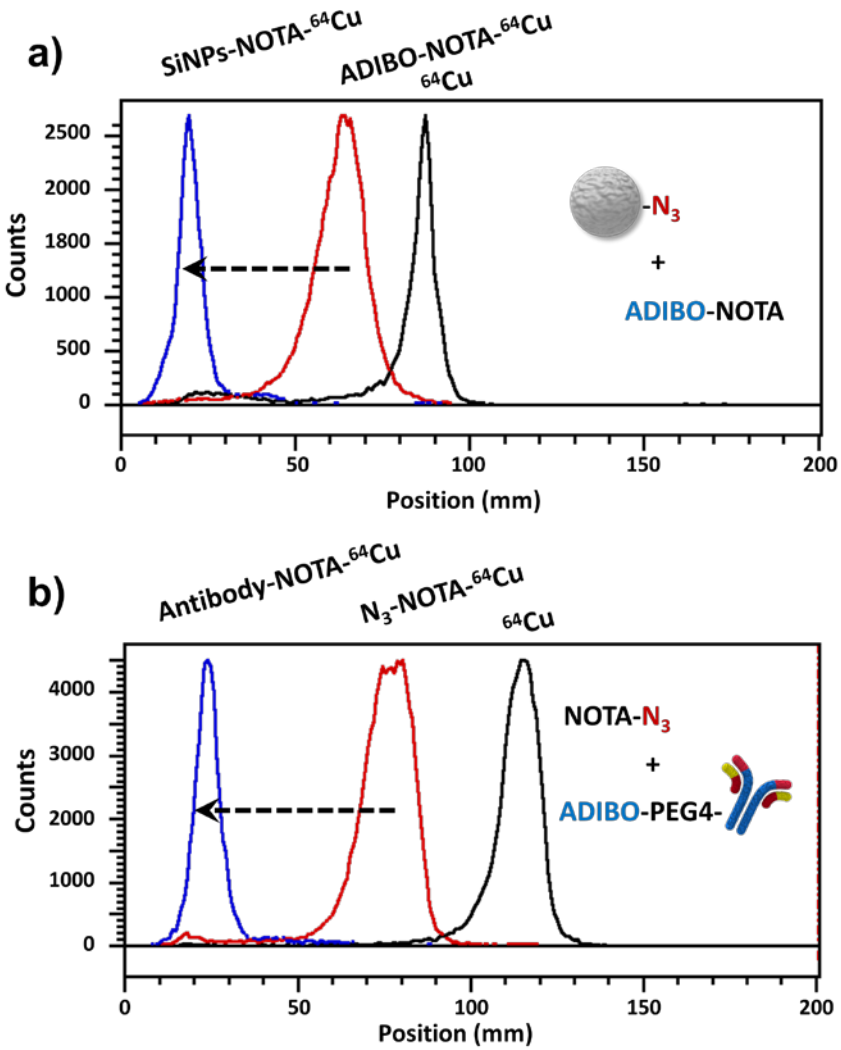

Figure 22. Radio thin-layer chromatography (TLC) analysis for the confirmation of functionalization of both the SiNP and the antibody. (a) The azido-functionalized SiNP was reacted with ADIBO-NOTA labeled with radio-active ^{64}Cu. (b) The ADIBO-functionalized antibody was conjugated to azido-NOTA labeled with radio-active ^{64}Cu.

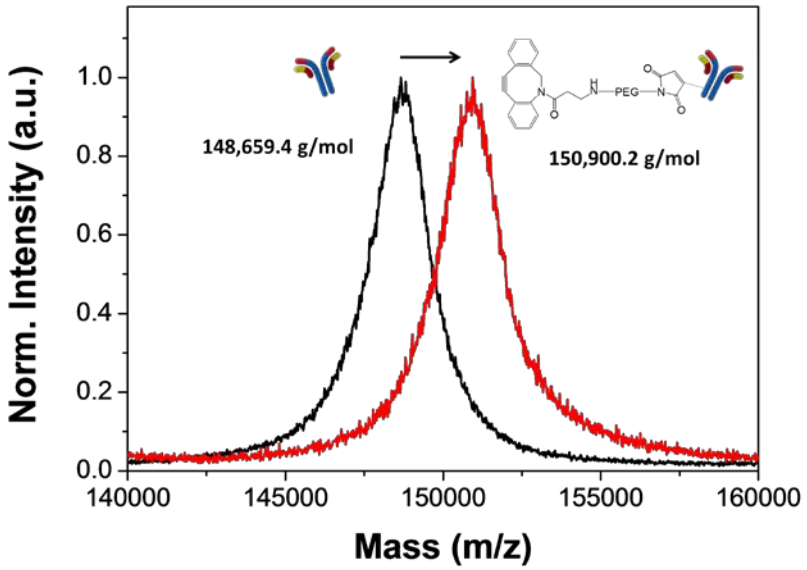

Figure 23. MALDI-TOF spectrometry analysis of antibody alone and the ADIBO-conjugated antibody.

2.4 Quantitative determination of the number of antibody conjugated on a single SiNP

The fluorescently-labeled antibodies (FL-antibodies) were conjugated to SiNPs in order to experimentally and quantitatively evaluate the number of conjugated antibodies on a single SiNP. (Figure 24 (a)) Firstly, the FL-antibodies were functionalized with ADIBO using ADIBO-PEG4-maleimide (ADIBO-FL-antibodies), and increasing concentrations were subsequently reacted with azido-SiNPs. For quantitative analysis, the concentration of azido-SiNPs was determined using nanoparticle tracking analysis (NTA, NanoSight™, Figure 25). Concurrently, the concentration of the ADIBO-FL-antibodies was determined using Nano-Drop™. The fluorescence signal of the FL-antibody-conjugated SiNPs was evaluated by obtaining the fluorescence images using fluorescence imaging instrument (IVIS™). As shown in Figure 24, each FL-antibody-conjugated SiNP was quantitatively analyzed based on the standard curve of the ADIBO-FL-antibodies (see Figure 26); as a result, a single SiNP with a 230-nm diameter had *ca.* 450 antibodies on its surface. Theoretically, the surface area of a 230-nm sphere-shaped SiNP corresponds to a covering area of *ca.* 900 antibodies, assuming *ca.* a 15-nm size for each (Figure 27). As regarding repulsions among the full-length antibodies, I estimate that the available surface of each SiNP was fully linked with antibodies. In comparison to conventional EDC/NHS coupling, in terms of conjugation efficiency (below 20%), the click chemistry-based antibody

conjugation method clearly shows superior coupling efficiency. In addition, by improving the coupling efficiency, the number of conjugated antibodies also increased. This enabled significant enhancement of the sensitivity and affinity of the antibody-conjugated NPs, resulting from multiple conjugated antibodies, also called avidity.[92, 93]

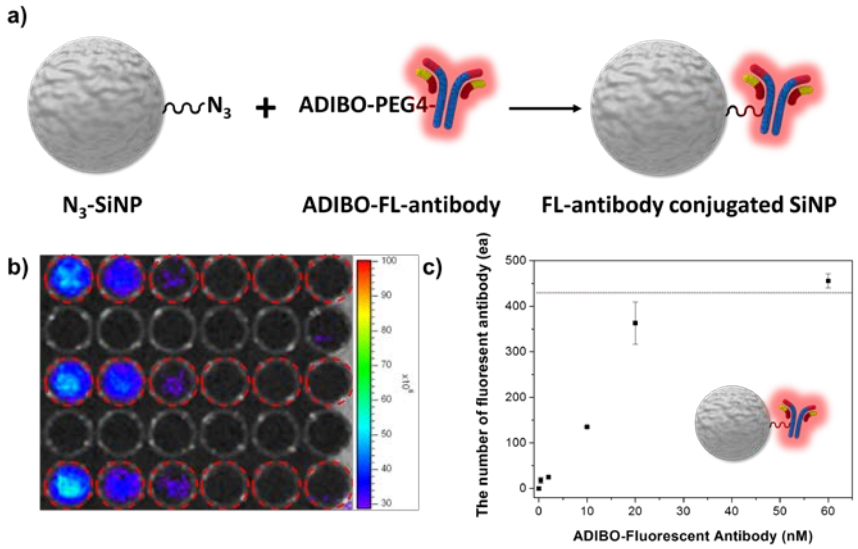

Figure 24. Quantification of the number of antibodies bound to a single SiNP using a fluorescent antibody. (a) Schematic illustration of the conjugation of the fluorescent antibody to SiNP using click chemistry. (b) Fluorescence image of the ADIBO-conjugated antibody obtained using an IVIS. (c) Quantitative analysis of the number of antibodies bound to a single SiNP using the fluorescence signal.

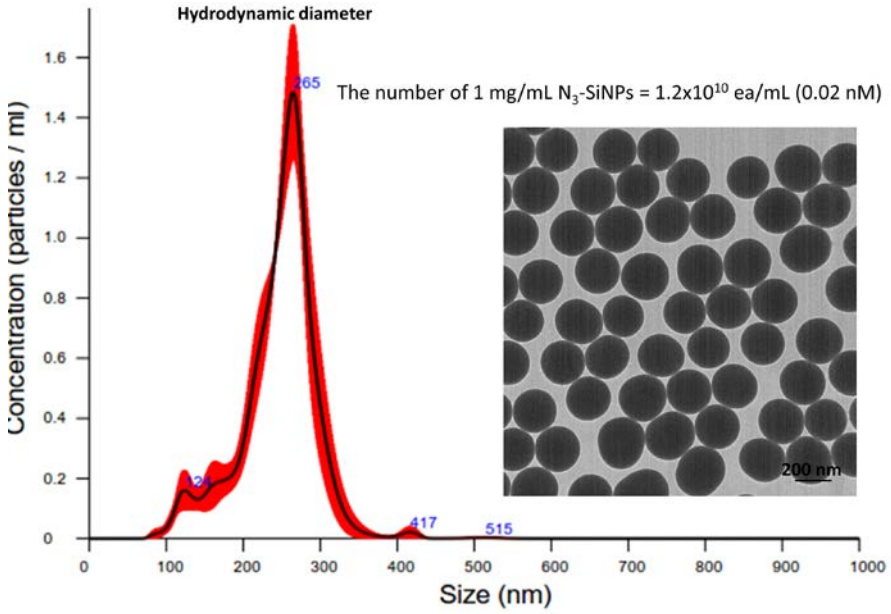

Figure 25. Characterization of silica nanoparticles (SiNPs) using nanoparticle tracking analysis (NTA, NanoSight Ltd) and transmit electron microscopy (TEM).

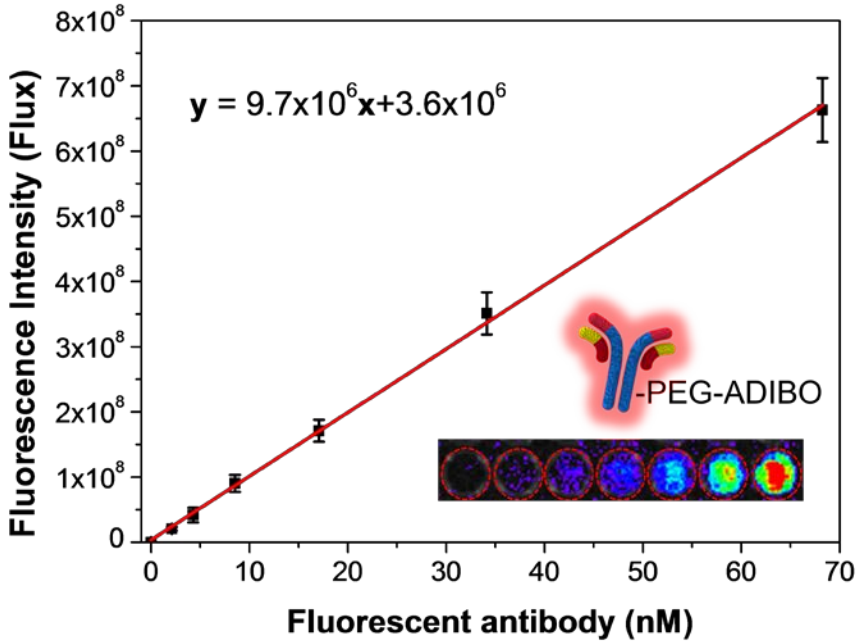

Figure 26. Standard curve according to the concentration of the ADIBO-conjugated fluorescent antibody. The inset was fluorescence image obtained by IVIS with 2 s-acquisition time.

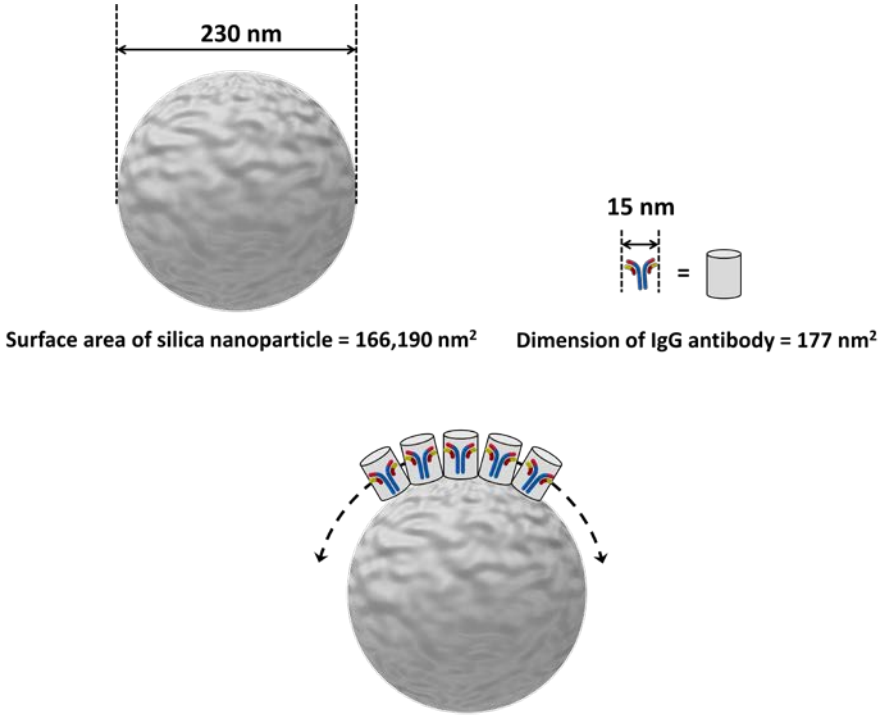

Figure 27. Theoretical calculation of the maximum number of the antibody conjugated to the surface of a single SiNP according to the dimension of an antibody and surface area of a single SiNP with a 230-nm diameter.

2.5 Quantitative determination of target binding ability of conjugate antibodies on NPs

In order to evaluate the targeting ability of antibody-conjugated SiNPs, I performed quantitative evaluation using fluorescent antigens. Furthermore, I compared the biofunctionality of the conjugated antibodies on the SiNPs prepared by EDC/NHS coupling and by click chemistry coupling. Using these methods, anti-human epidermal growth factor receptor 2 (HER2) antibody-conjugated SiNPs (anti-HER2-SiNPs) were prepared by both coupling methods. Subsequently, the anti-HER2-SiNPs were reacted with the HER2 antigen labeled with a fluorescent dye (FNR-648). As shown in Figure 28, a single anti-HER2 SiNP prepared by the click chemistry conjugation method could bind *ca.* 800 fluorescent antigens, revealing that almost all the conjugated antibodies were bioactive, since each of the *ca.* 450 antibodies on a single SiNP can bind two antigens. This high binding capability of the antibodies is attributed to the high coupling efficiency to SiNPs and the orientation control of the antibodies by functionalizing the site-specific thiol groups in the Fc domain while minimizing antibody denaturation. On the other hand, a single anti-HER2 SiNP prepared by the EDC/NHS coupling method could capture only *ca.* 100 antigens, which can be interpreted as a low conjugation efficiency of EDC/NHS coupling (1-20%) and randomly oriented antibodies due to the utilization of the primary amine functional groups in the antibodies for conjugation.[94]

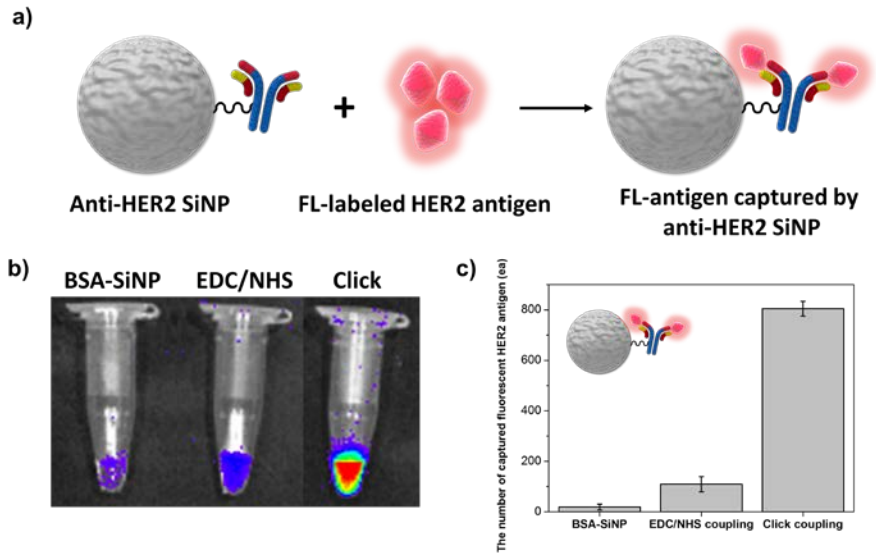

Figure 28. Quantitative evaluation of the antigen-binding capability of antibodies conjugated to SiNPs. (a) Schematic illustration of the quantitative bio-assay using fluorescent HER2 antigen. (b) Fluorescence images of BSA-treated SiNPs and anti-HER2-antibody conjugated SiNPs prepared using EDC/NHS coupling or click coupling method, respectively.

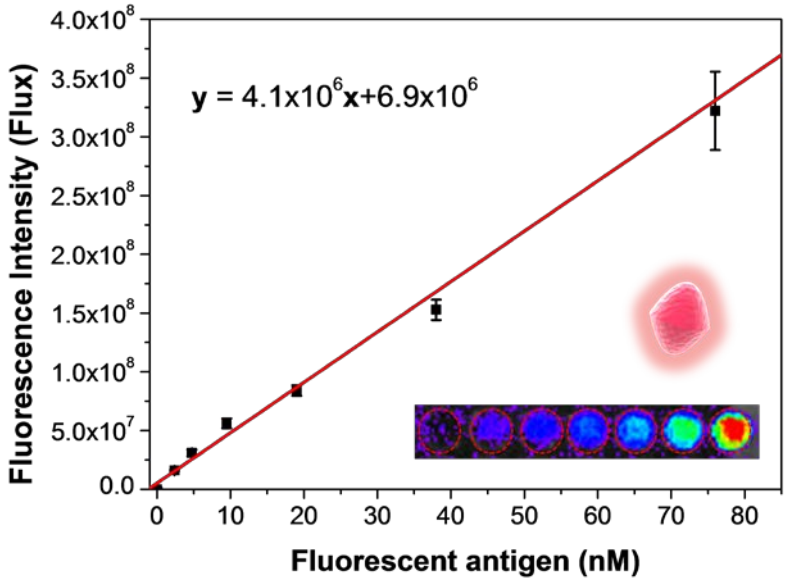

Figure 29. Standard curve according to the concentration of the fluorescently-labeled HER2 antigen with FNR-648. The inset was fluorescence image obtained by IVIS with 2 s-acquisition time.

2.5 *In vitro* immunoassay on breast cancer cells for comparison of target binding ability of antibodies on NPs prepared Click and EDC/NHS coupling method

To compare the target binding ability of the antibodies on the NP, conjugated by click chemistry and the EDC/NHS coupling method, an *in vitro* immunoassay was performed on the breast cancer cell line, MDA-MB 231/HER2, which expresses a high level of the HER2 biotarget (Figure 30). As a selectively targetable nanoprobe, silica-encapsulated quantum dot-embedded SiNPs (QD^2), which are considerably brighter than single quantum dots,[95] were utilized by conjugation to the anti-HER2 antibodies. The target binding capability of anti-HER2-QD^2 was evaluated by obtaining the fluorescence images of anti-HER2-QD^2 treated cancer cells using confocal laser scanning microscopy (CLSM). When 5 pM of anti-HER2 QD^2 was treated, the anti-HER2-QD^2 prepared by click chemistry (anti-HER2-QD^2_{click}) exhibited a much higher target binding ability than those prepared by EDC/NHS coupling (anti-HER2-$QD^2_{EDC/NHS}$) (Figure 31). These results were attributed to intact biofunctionality of the full-length antibodies on anti-HER2-QD^2_{click} due to the controlled orientation and the high conjugation efficiency of click chemistry. These results are also consistent with the quantitative evaluation of the target binding ability using fluorescent antigens; the antibody-conjugated SiNPs prepared by the click chemistry had an 8-times higher target-binding ability than those prepared by the EDC/NHS coupling

method. In particular, with treatment of 2 pM anti-HER2-QD^2, the targeted anti-HER2-$QD^2_{EDC/NHS}$ were not observed; however, anti-HER2 QD^2_{click} at the same concentration was appreciably targeted to the membrane of the cancer cells (Figure 31). From these results, I was also able to experimentally demonstrate that the sensitivity of the NP-based diagnostic platform incorporating antibodies is greatly affected by the antibody conjugation method, not only sensitivity of nanoprobes. To ensure the specific targeting ability of antibody-conjugated NPs, I used the bovine serum albumin-treated QD^2 (BSA-QD^2) without antibody conjugation as a negative control. No binding was seen with the non-selectively targeted BSA-QD^2 at any concentration (Figure 31(c)); this implied that all anti-HER2-QD^2 was successfully targeted with high selectivity.

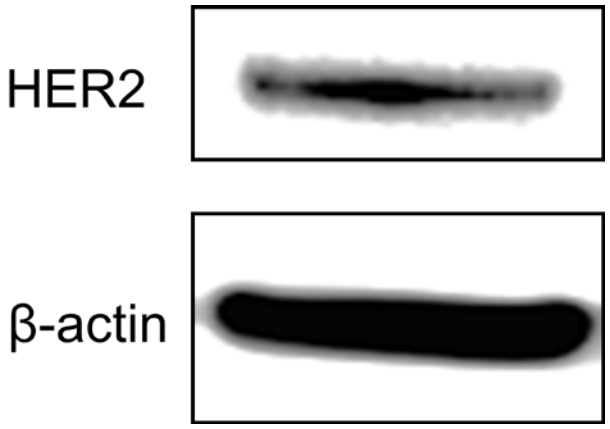

Figure 30. Western blot analysis of HER2 expression in the breast cancer cell-line (MDA-MB231/HER2). The β-actin was used as a loading control.

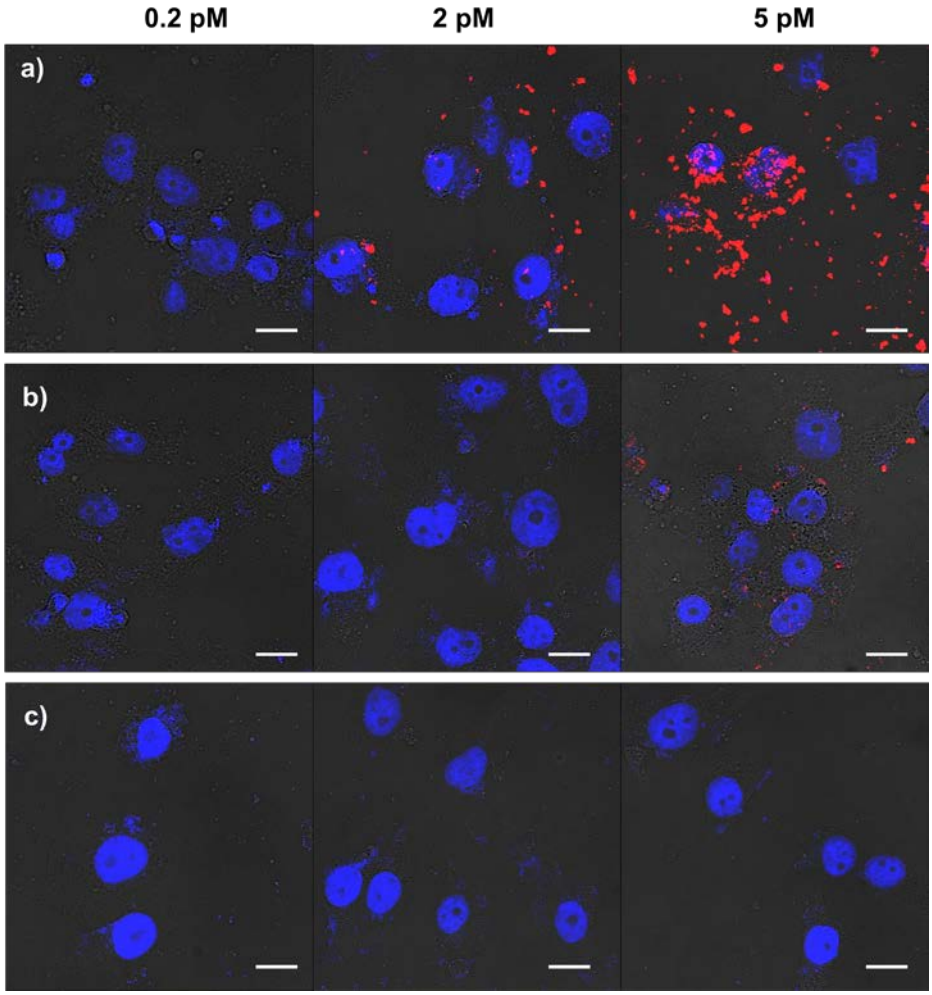

Figure 31. *In vitro* immunoassay using breast cancer cells (MDA-MB-231/HER2) for comparison of the targeting ability of antibodies on fluorescent NPs (anti-HER2 QD^2) conjugated by click chemistry or EDC/NHC coupling. Confocal laser scanning microscopy images of cancer cells targeted by anti-HER2-QD^2 conjugated by the click chemistry method (a) or the EDC/NHS coupling method (b); as a negative control, BSA-QD^2 was also treated (c). The scale bar represents 20 μm. The anti-HER2-QD^2 are represented by a red color, and the nuclei are stained by DAPI, indicated by a blue color.

2.6 Demonstration of versatility of the click chemistry based antibody conjugation method for silica encapsulated nanoprobes

To further verify the versatility of the developed antibody conjugation method, the anti-HER2 antibodies were conjugated with various types of silica-encapsulated nanoprobes such as QD^2, surface-enhanced Raman scattering nanoprobes (SERS dots), and fluorescent SERS dots (F-SERS dots).[96, 97] The anti-HER2 antibody-containing nanoprobes were analyzed by SDS-PAGE analysis to confirm antibody conjugation (Figure 32). In the SDS-PAGE analysis, only the stained bands at the top of the SDS-PAGE gel appeared, with no other bands at smaller molecular weights. This result clearly demonstrates that the antibodies were successfully conjugated to all types of silica-based nanoprobes, without leaving antibody fragments. It also suggests that the click chemistry-based antibody conjugation method can be widely applied to any type of silica-encapsulated nanoprobe, regardless of the inner structure. This antibody conjugation method can be extensively utilized to develop immunosensors on a glass substrate.

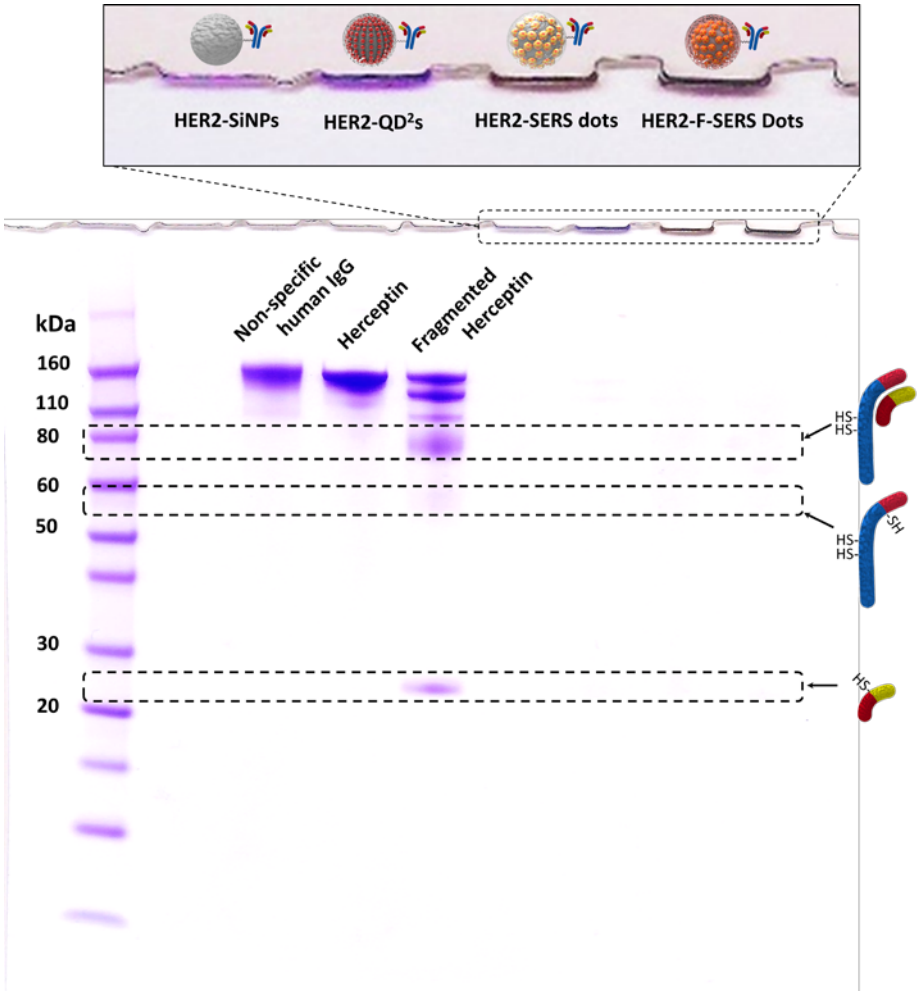

Figure 32. SDS-PAGE analysis of various antibody-conjugated NPs: anti-HER2-SiNPs, anti-HER2-QD^2, anti-HER2-SERS dots, and anti-HER2-F-SERS dots. All azido-NPs (1 mg/mL) were treated with same amount of the ADIBO-conjugated antibody, 50 μg.

3. *In Vivo* and *In Situ* Multiplexed Molecular Diagnostics using FRES for Breast and Colorectal Cancer

3.1 Evaluation of *in vitro* quantitative molecular diagnosis in colorectal cancer cell line using FRES

To evaluate feasibility of FRES for *in vitro* quantitative molecular diagnostic tool, active targeting on the colorectal cancer cells (HT29) were performed using antibody-conjugated F-SERS dots. As biotargets, the EGFR and VEGF expression on this cancer cell line were confirmed by western blot analysis (Figure 33). HT29 cells (10^4 cells/well) were seeded in an 8-well chambered cover glass with 300 μL of cell media per well.

For the quantitative analysis, the anti-EGFR antibody-conjugated F_{AF610}-$SERS_{RITC}$ dots (anti-EGFR-F-SERS dots-A) was treated HT29 cells with various amount of anti-EGFR-F-SERS dots-A: 0, 5, 10, 20, 40, 60, 80 and 100 μg. As shown in Figure 34, the FRES incorporating antibody-conjugated F-SERS dots shows high sensitivity in *in vitro* condition by detecting at 5 μg of anti-EGFR-F-SERS dots-A treatment (*ca.* 2 pM). As increasing the treated amount of the anti-EGFR F-SERS dots-A, the fluorescence and SERS signals were also increased up to 40 μg of anti-EGFR-F-SERS dots-A treatment. Over the 40 μg of anti-EGFR-F-SERS dots-A, the SERS signals were saturated. These results demonstrated the quantification ability of the FRES for the biotargets and also implied that the FRES can be utilized as an *in vivo* quantitative molecular diagnostic tool with high sensitivity.

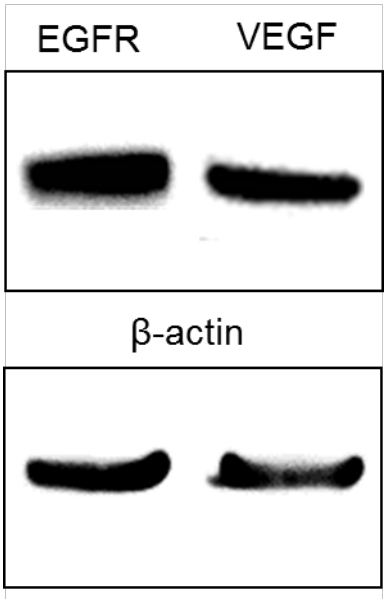

Figure 33. Western blot analysis of EGFR and VEGF expression in the colorectal cancer cell-line (HT29). The β-actin was used as a loading control.

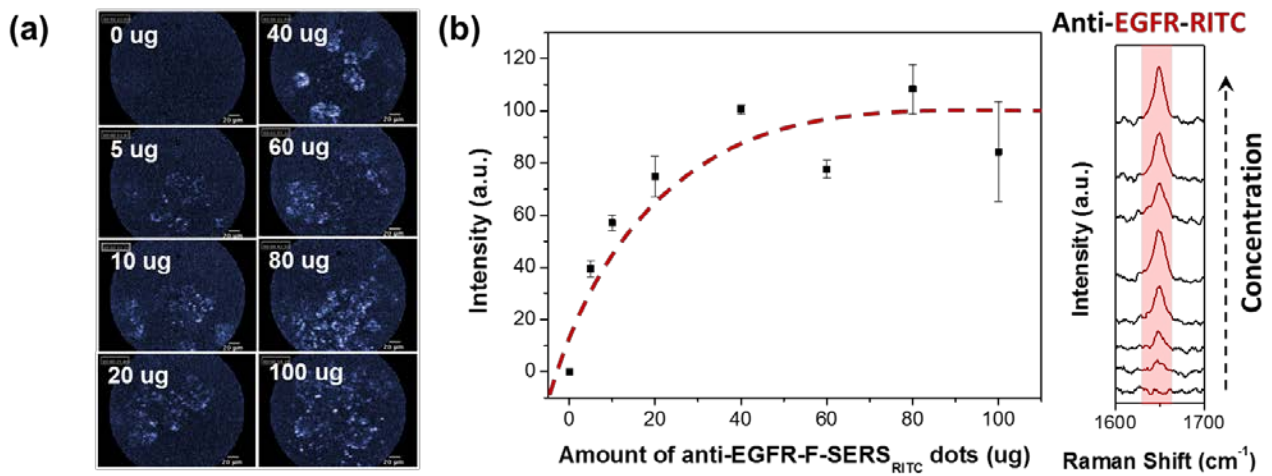

Figure 34. *In vitro* quantitative molecular diagnosis on colorectal cancer cell-line using the FRES. (a) The real-time fluorescence images at each treated amount of anti-EGFR-F-SERS dots. (b) The left side plot shows the SERS intensity profile of 1648 cm^{-1} corresponding to RITC Raman label compound. The right side plot shows the representative Raman spectra at each treated concentration of anti-EGFR-F-SERS dots.

3.2 Signal grades of detected Raman signal from FRES

To precisely describe the detected Raman signals, they were graded into three levels: clearly detectable, just-noticeably detectable, and non-detectable. To distinguish the signals from the background signals, the intensity of the signal should be higher than the noise-level intensity in a spectrum. Under this detecting condition, the noise-level intensity was 10 cps; this was determined by calculating standard deviation of the background signals. By this noise-level, I quantitatively graded the results of the multiplexed detection on cancer xenografts according to the intensity of the representative Raman bands, 1648 cm^{-1} of RITC and 1324 cm^{-1} of FITC, as follows: a) clearly detectable, over the 30 counts per second (30 cps, more than 3 times of noise-level), b) just-noticeably detectable, from 10 to 30 cps (not more than 3 times and more than noise level), and c) non-detectable, from 0 to 10 cps (below noise-level). (Figure 35)

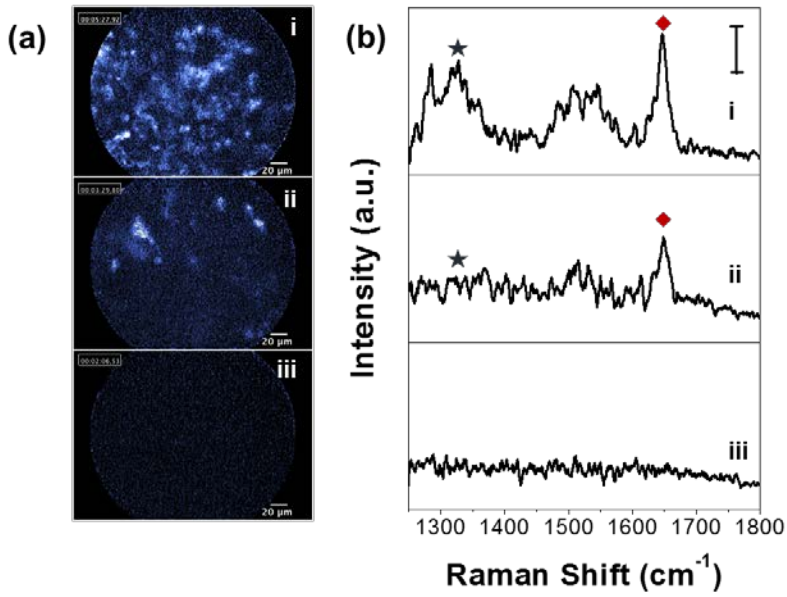

Figure 35. The representative (a) fluorescence images and (b) Raman spectra of each grades in whole results of the endoscopic multiplexed molecular diagnosis on the breast tumor xenografts. The grades of multiplexed detection are as follows: i) clearly detectable, ii) just-noticeably detectable, and iii) non-detectable. The scale bar in Raman spectra is 30 counts per second (cps). The labeled Raman bands in Raman spectra represents anti-EGFR antibody-conjugated F_{AF610}-$SERS_{FITC}$ dots (★) and anti-HER2 antibody-conjugated F_{AF610}-$SERS_{RITC}$ dots (◆), respectively.

3.3 *In vivo* and intraoperative multiplexed molecular diagnostics on breast cancer xenograft model

To confirm the feasibility of an endoscopic molecular diagnostics with FRES from the perspective of an intraoperative examination, four xenograft model mice were produced from the MDA-MB-231/HER2 breast cancer cell line, which expressed high levels of HER2 and EGFR (Figure 36). The active targeting was performed on the tumor surface (i.e., outer surface) and on the cut surface of the tumor 5-mm deep from the outer surface, respectively. Since subcutaneous breast cancer implants in mice were used, I first incised the skin of the breast near the tumor and simulated endoscopic imaging by probing the outer surface of the tumors and subsequently of their cut surface. After pretreatment with blocking antibodies, the targeting F-SERS dots (the anti-HER2-F_{AF610}-$SERS_{RITC}$ dots and anti-EGFR-F_{AF610}-$SERS_{FITC}$ dots) were sprayed directly on the surface of the tumor tissue. After incubation for 10 min, the unbound F-SERS dots were washed three times with PBS (pH 7.4). The fluorescence and Raman signals were simultaneously detected by a minimally invasive injection of the optical fiber bundle probe of the FRES (Figure 37).

Figure 38 shows a representative result from the four sets of the tumor surface studies. For the tumor site (i) in Figure 38(b), the distinct SERS bands in the Raman spectra were observed at 1285 and 1648 cm^{-1} corresponding to the anti-HER2-F_{AF610}-$SERS_{RITC}$ dots, and at 1324 and 1633 cm^{-1}

corresponding to the anti-EGFR-F_{AF610}-$SERS_{FITC}$ dots. At the same time, the location of the targeted F-SERS dots could be identified as a bright area in a dark background of the non-targeted lesions ((i) in Figure 38(a)), thereby indicating that the intense fluorescence signals of these F-SERS-dots with the AF610 dye can rapidly track the targeted regions. For the tumor site (ii) in Figure 38(b), which was treated with an anti-HER2 antibody to block the HER2 receptor, distinct SERS bands at 1324 and 1633 cm^{-1} corresponding to the anti-EGFR-F_{AF610}-$SERS_{FITC}$ dots were observed, without the bands of the anti-HER2-F_{AF610}-$SERS_{RITC}$ dots at 1285 and 1648 cm^{-1}. A bright area was observed in the fluorescence images ((ii) in Figure 38(a)). In contrast, at the anti-EGFR antibody-treated tumor site (iii) in Figure 38(b), the distinct bands at 1285 and 1648 cm^{-1} corresponding to the anti-HER2-F_{AF610}-$SERS_{RITC}$ dots were only observed in the Raman spectra. The targeted locations also appeared as a bright area in the fluorescence images ((iii) in Figure 38(a)). In the case of both antibodies-treated tumor site (iv) in Figure 38(a) and (b), I did not observe either fluorescence or SERS signals. As shown in Figure 38(a) and (c), only the targeted tumor areas exhibited fluorescence signals from the F_{AF610}-$SERS_{RITC/FITC}$ dots (represented by blue color in the FRES images or red color in the confocal laser scanning microscopy images), thus indicating that the antibody-conjugated F-SERS dots were specifically bound to the HER2 and EGFR expressing tumor tissues. To validate reproducibility of FRES in an endoscopic multiplexed molecular diagnosis, the entire results of

the multiplex detection in the outer and cut surfaces of the tumor in the four mice were categorized into three grades: ‘clearly detectable’, ‘just-noticeably detectable’, and ‘non-detectable’. For the outer surface study, 75% (3/4) was graded as ‘clearly detectable’, and 25% (1/4) was graded as ‘just-noticeably detectable’. For the cut surface study, 100% (4/4) of tumors were graded as ‘clearly detectable’. Non-detectable cases were not found in either surface of tumor (Table 1).

The reproducibility and applicability of FRES for the *in vivo* multiplex molecular diagnostics were demonstrated by direct topical administration of the antibody-conjugated F-SERS dots on the outer and cut surfaces of the breast tumor xenografts in the four mice. The antibody-conjugated F-SERS dots selectively targeted the corresponding the HER2 and EGFR on the outer and cut surfaces of the cancerous tissues. In terms of a multiplexed molecular diagnostics, the HER2 and EGFR were identified clearly at the same time on the outer and cut tumor surfaces in the four mice with 75% and 100% accuracy, respectively. For only one case in the outer surface, two kinds of biotargets were just-noticeably detectable without any significant error. The observed small variation was understood probably due to the variation of the HER2/EGFR expression according to the size and physiological conditions of the tumor implants. These results demonstrated that the real-time fluorescence imaging and Raman spectral measurement provided easy identification of the location of the culprit lesion and the types of targeted biomolecules thereof in an extensive area of suspected cancerous tissues

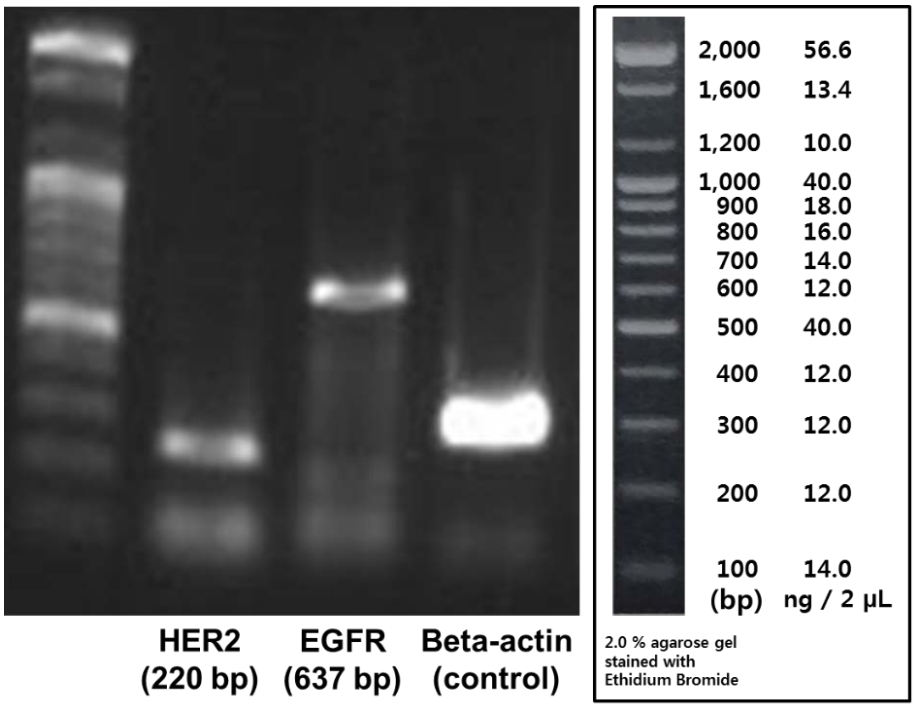

Figure 36. Reverse transcriptase-polymerase chain reaction (RT-PCR) for identification of the HER2 and EGFR expression in the MDA-MB-231/HER2 breast cancer cell line.

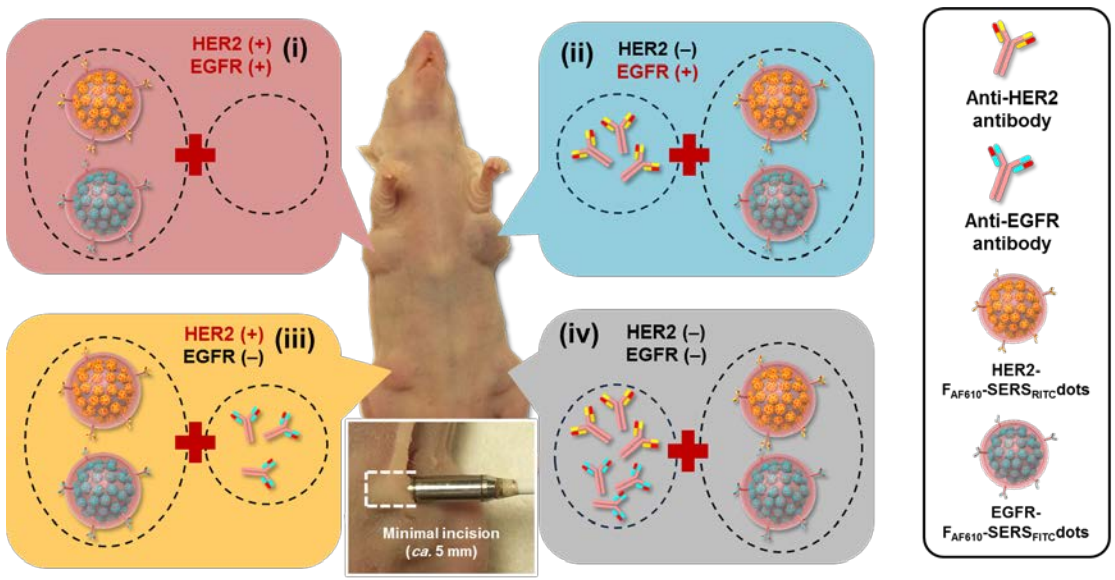

Figure 37. Demonstration of an *in vivo* active targeting ability of the F-SERS dots on the HER2 and EGFR positive breast tumor xenografts. Each tumor site (i) was not treated with any antibody, (ii) pre-treated with the anti-HER2 antibody, (iii) pre-treated with the anti-EGFR antibody, or (iv) pre-treated with both antibodies for blocking specific binding. Then, they were treated with the F-SERS dots (anti-HER2-F_{AF610}-$SERS_{RITC}$ dots and anti-EGFR-F_{AF610}-$SERS_{FITC}$ dots) for the FRES imaging. A photograph of the tumor-bearing mouse with the receptor expression status as shown besides the image. The real-time fluorescence images and Raman spectra were simultaneously obtained with an optical fiber bundle probe of the FRES (lower box).

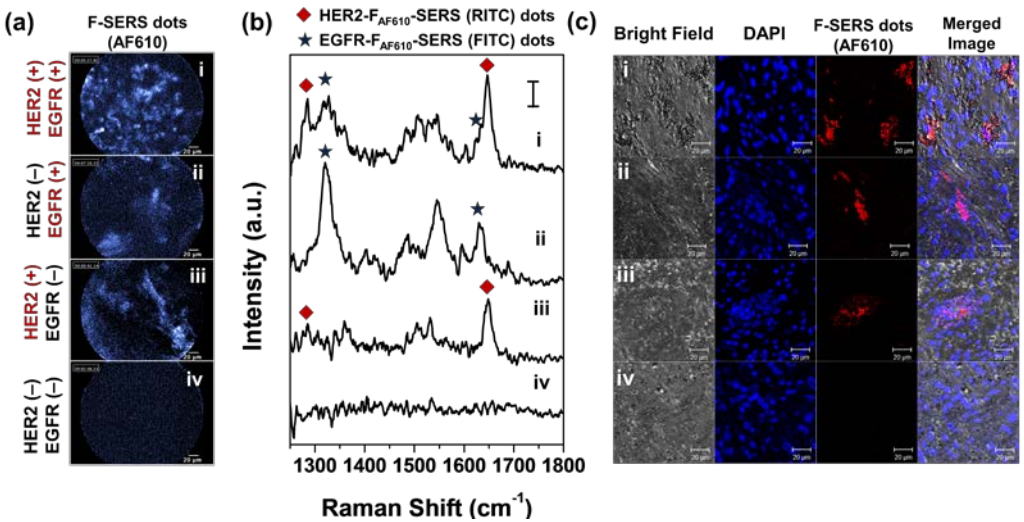

Figure 38. *In vivo* multiplexed molecular diagnosis of breast cancer xenografts using FRES. (a) Fluorescence images were obtained by the FRES with real-time (12 frames/s). The bright area in fluorescence images corresponds to the targeted probes. (b) Raman spectra were obtained by the FRES at a laser power of 2.7 mW and acquisition time of 1 s. Each tumor site (i) was not treated with any antibody, (ii) pre-treated with the anti-HER2 antibody, (iii) pre-treated with the anti-EGFR antibody, or (iv) pre-treated with both antibodies for blocking specific binding. The observed Raman bands in the Raman spectra correspond to the RITC (◆) and FITC (★) from the F-SERS dots. (c) Confocal fluorescence laser scanning (CLSM) images of the tumor sites. The nuclei of the tumor cells stained with 4',6-diamidino-2-phenylindole (DAPI) dye were shown as blue spots, and the targeted F-SERS dots containing Alexa Fluor 610 were shown as red spots.

Table 1. The grades of whole results of the *in vivo* multiplexed molecular diagnosis on the outer and cut tumor surfaces of breast tumor xenografts in four mice. The results of multiplexed detection were graded according to the intensity of the representative Raman bands, 1324 cm^{-1} of FITC and 1648 cm^{-1} of RITC, as follows: a) clearly detectable, over the 30 counts per second (cps), which is three times of the noise-level, b) just-noticeably detectable, from 10 to 30 cps, and c) non-detectable, from 0 to 10 cps. The noise-level intensity was 10 cps, which was defined by the standard deviation of the background signals.

Multiplexed detection	**Outer surface**	**Cut surface**	**Total**
Clearly detectable	75.0% (3/4)	100% (4/4)	87.5% (7/8)
Just-noticeably detectable	25.0% (1/4)	0.0% (0/4)	12.5% (1/8)
Non-detectable	0.0% (0/4)	0.0% (0/4)	0.0% (0/8)

3.4 *In vivo* and intraoperative endoscopic multiplexed molecular diagnostics on CRC xenograft using the FRES

To demonstrate usability of the FRES as an endoscopic molecular diagnosis with non-invasive procedure, the biotargets expressed on CRC xenograft were identified using the FRES *via* colonoscopic examination in a multiplex way. (Figure 39) The molecular characterization of CRC is crucial for the selection of most appropriate treatment option and also for patients' prognosis and quality of life. For CRC, EGFR (anti-EGFR monoclonal antibody: Cetuximab®) and VEGF (anti-VEGF monoclonal antibody: Bevacizumab®) targeted therapy is the standard therapy that prolongs the survival in patients with metastatic disease[98], and previous studies have also shown that EGFR[99] and VEGF[100, 101] can be identified by *in vivo* molecular imaging. From these background, EGFR and VEGF were selected as biotargets in this study: EGFR targets cellular membrane[102] and VEGF targets extracellular matrix[103].

A total of 20 mice having CRC xenograft were investigated. To topically administrate the targeting agents, the mixture of two kinds of antibody-conjugated F-SERS dots (anti-EGFR-F-SERS dots-A 100 μg + VEGF-F-SERS dots-B 100 μg) were directly sprayed using micropipette *via* anus. In addition, 9 normal mice were also investigated as controls according to above active targeting manner. As shown in Figure 40, by utilizing the FRES, the location of targeted F-SERS dots was identified in real-time fluorescence

images; simultaneously, the targeted biomakers were also identified by observing the Raman bands at 1648 cm^{-1} of RITC for anti-EGFR-F-SERS dots and 1324 cm^{-1} of FITC for anti-VEGF F-SERS dots, respectively (Figure 40(c)). In contrast, in all cases of normal mice as a control, any fluorescence and Raman signals were not observed. Among the 20 mice, these biotargets (EGFR and VEGF) in 15 mice were clearly detectable, 75% (15/20); another 5 mice were just-noticeably detectable. However, non-detectable cases were not found. (Table 2). These results were demonstrated the multiplex targeting ability of FRES for tumor receptor marker (EGFR) and tumor-secreted biomolecules (VEGF) in the microenvironment; it strongly supported that the FRES has great extendability to *in vivo* molecular diagnostics including not only the surface epitopes of immune or stromal cells but also fibroblasts and other secreted peptides or cytokines prevalent in the tumor microenvironment.

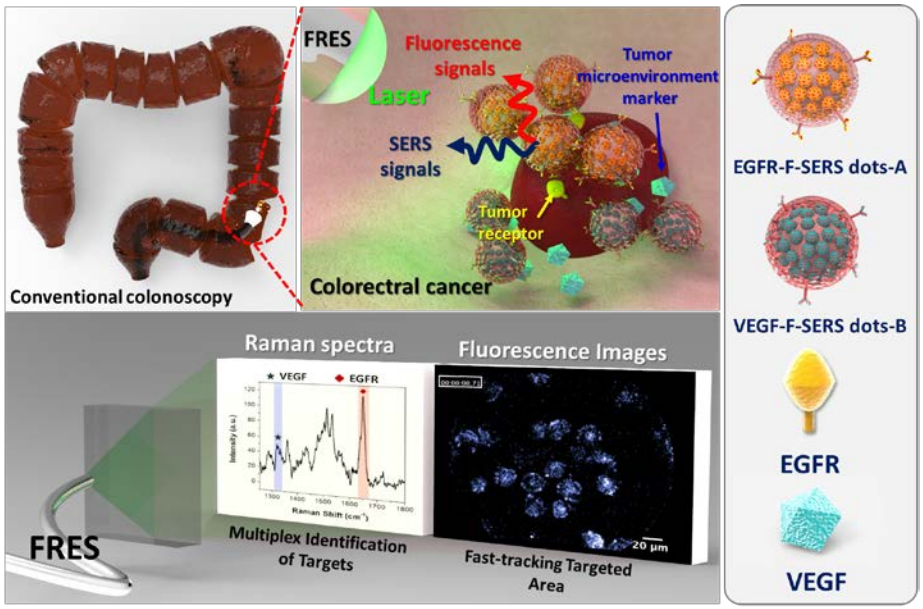

Figure 39. Schematic of *in vivo* multiplex molecular diagnosis for CRC using FRES. FRES can detect fluorescence and Raman signals simultaneously for molecular characterization of the tumor. When antibody-conjugated F-SERS dots were sprayed onto CRC tumor, the antibody-conjugated F-SERS dots bound to colon cancer cells (epidermal growth factor receptor; EGFR) and tumor microenvironments (vascular endothelial growth factor; VEGF). Based on both real-time fluorescence images and Raman spectra comes from specifically targeted F-SERS dots, the CRC could be molecularly characterized during colonoscopic examination.

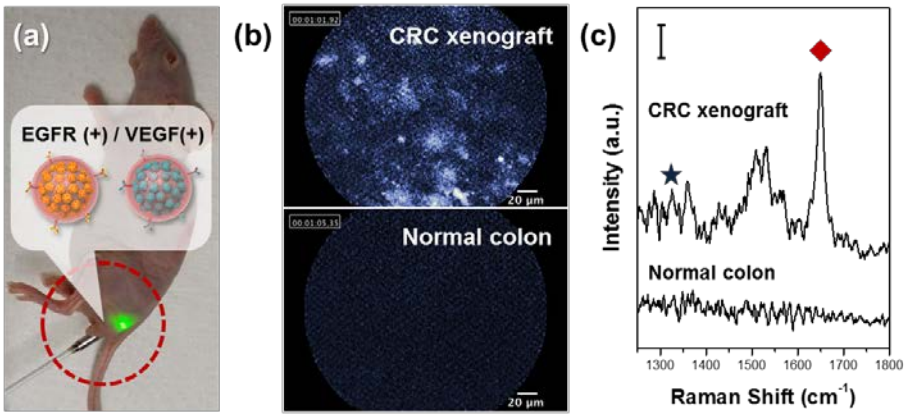

Figure 40. *in vivo* endoscopic multiplexed molecular diagnosis for CRC using FRES. (a) A photograph of colonoscopic examination *via* anus using the optical fiber bundle probe of the FRES for *in vivo* molecular diagnostics in orthotopic CRC xenograft mice. (b) Fluorescence images of CRC xenograft and normal colon tissue obtained by the FRES with real-time (12 frames/s). The bright area in fluorescence images corresponds to the targeted probes. (c) The Raman spectra of CRC xenograft and normal colon obtained by the FRES at a laser power of 2.7 mW and acquisition time of 1 s. The observed Raman bands in the Raman spectra correspond to the RITC (◆) and FITC (★) from the F-SERS dots.

Table 2. The grades of whole results of the *in vivo* endoscopic multiplexed molecular diagnosis on CRC xenografts in twenty mice with non-invasive procedure.

Multiplexed detection	**Biotargets on CRC xenograft**
Clearly detectable	75.0% (15/20)
Just-noticeably detectable	25.0% (5/20)
Non-detectable	0.0% (0/20)

3.5 Evaluation of *ex vivo* relative quantification ability of the FRES in tumor xenograft

By quantifying the Raman intensity using the FRES, the molecular heterogeneity of biotarget (EGFR) expression in tumor was evaluated in *ex vivo* condition. After 1 week of 1×10^7 HT29 cells subcutaneous injection, tumors were excised, and hemisected. One half tumor was treated with a 100 μg of anti-EGFR F-SERS dots according to *in vivo* targeting procedure (direct spraying method and incubation for 10 min). For further confirmation and evaluation of the EGFR expression, the other half tumor was examined by IHC. As shown in Figure 41, as increasing EGFR expression level in the tumor, the intensity of representative Raman band at 1648 cm^{-1} of RITC increased: 15 cps for low (i), 20 cps for moderate (ii), and 40 cps for high expression level (iii); at the same time, the bright area in real-time fluorescence image, which represented the targeted F-SERS dots with EGFR molecules, was also extended as increasing EGFR expression level. These results indicated that the FRES can be utilized to not only qualitatively but also quantitatively identify the pathological condition of suspicious lesion at the molecular level.

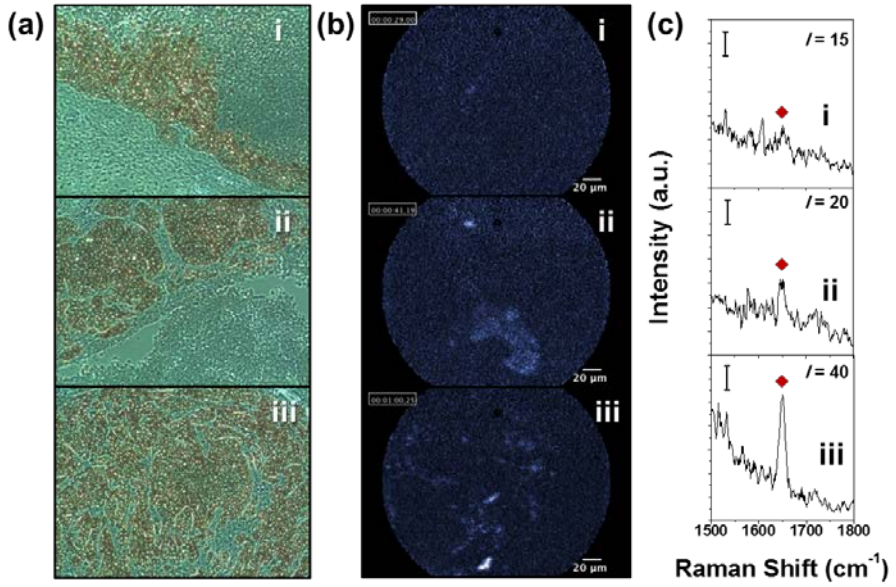

Figure 41. The evaluation of heterogeneous EGFR expression by the FRES *ex vivo*. The tumors were excised, and divided in half. (a) IHC results for EGFR expression in tumor; the dark lesion represents the EGFR expression in the tumor. The fluorescence images (b) and Raman spectra (c) were obtained by the FRES with 2.8 mW laser-power and 1 s acquisition time. The bright area in fluorescence images represents targeted anti-EGFR-F-SERS dots. The Raman band (♦) at 1648 cm^{-1} of RITC corresponds to anti-EGFR-F-SERS dots.

3.6 Validation of non-specific binding of the F-SERS dots for normal tissue in *in vivo* condition

For evaluating the non-specific binding of the F-SERS dots on a tissue, as a negative control, normal tissue (peritoneum) was examined by the FRES with the BSA treated F-SERS dots according to the active targeting procedure. As shown in Figure 42, at first, after spraying the BSA treated F_{AF610}-$SERS_{RITC}$ dots on the peritoneum, I could clearly observe fluorescence and Raman signals corresponding to the F-SERS dots in fluorescence image and Raman spectrum. However, after washing with PBS several times, the fluorescence and Raman signals disappeared. Additionally, the fluorescence signal of AF610 corresponding to the F-SERS dots was also not observed in the confocal laser scanning microscope images of the normal tissue after washing with PBS. Based on these results, I could confirm that the BSA treated F-SERS dots were not physically and non-specifically adsorbed on the peritoneum (i.e., the normal tissue).

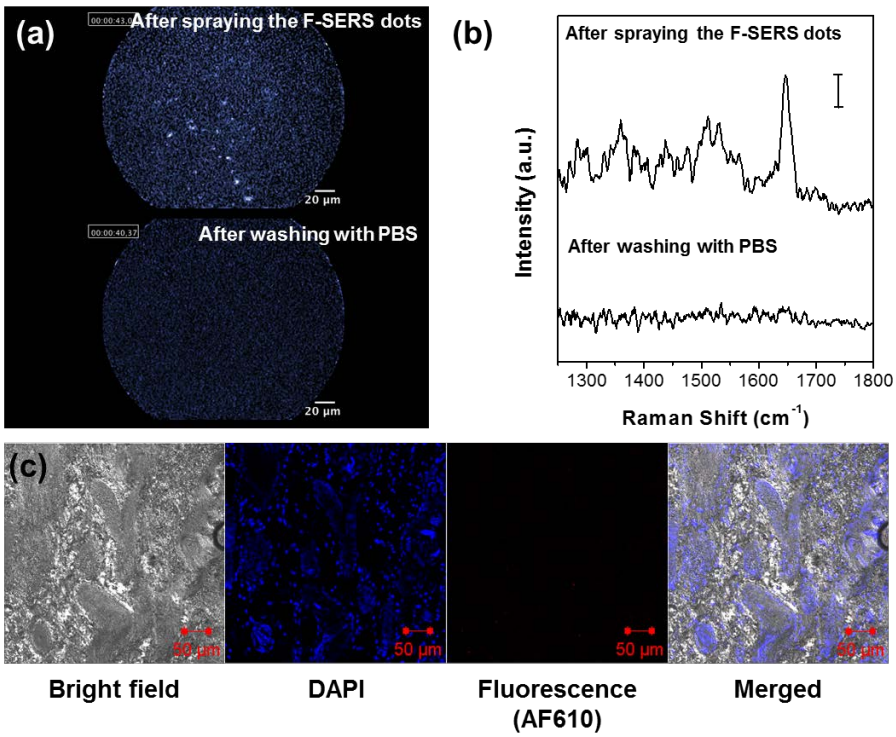

Figure 42. Evaluation of the non-specific binding of the F-SERS dots on the normal tissue, peritoneum. The fluorescence images (a) and Raman spectra (b) of the normal tissue after spraying the BSA treated F_{AF610}-$SERS_{RITC}$ dots and then washing with PBS. (c) The confocal laser scanning microscope images of the normal tissue after washing with PBS.

3.7 Significance of the FRES as an *in vivo* and intraoperative multiplexed molecular diagnostic tool

In this study, a novel endoscopic system using fluorescence-SERS active nano-probes has demonstrated successfully an *in vivo* dual modal detection of multiple targets for specific cancer tissue. The technique was based on simultaneous detection of dual modalities involving fluorescence and Raman signals using a single laser-line of excitation. This approach utilized F-SERS dots as tumor-targeting agents by directly spraying them on a suspicious lesion, thereby allowing for a real-time endoscopic multiplexed molecular diagnostics. Compared to previous fluorescence and/or Raman endoscopic diagnosis techniques, [18, 19, 36, 37] our strategy of using the FRES with F-SERS dots showed great potential for clinical diagnostics. For example, although fluorescence endoscopy provides highly sensitive fluorescence images, it does not have multiplexing capabilities due to its broad bandwidth of fluorescence emission. In contrast, Raman endoscopy with SERS dots as targeting agents can simultaneously detect subtle molecular changes and multiple bio-targets. However, the Raman endoscopy is limited for a clinical use because it can characterize only a small portion of an extensive suspicious lesion. To address these limitations, I have optimized the spectral design and endoscopic instrument. The F-SERS dots were fabricated to emit fluorescence and SERS signals at the same time by a single excitation source, and the FRES was designed to simultaneously detect fluorescence and Raman signals as a real-

time imaging instrument. Although the FRES cannot provide a wide-field endoscopic imaging (i.e., over several centimeters),[28, 104] the real-time fluorescence imaging ability (240 μm field of view, 12 frames/sec) of the FRES allowed for rapid localization of a pathologic lesion in the extensively suspicious area of interest,[105, 106] while the Raman spectra enabled the identification of different types of F-SERS dots bound to multiple bio-targets. Furthermore, the FRES utilized the optical fiber bundle with an external diameter of *ca.* 2.6 mm, which can be inserted into the instrument channel of a conventional endoscope. This feature could enable the FRES to be intraoperatively utilized for molecular diagnosis during a well-established endoscopic examination without further modification of the conventional endoscopic instrument.

When compared to immunohistochemistry analysis which has shortcomings such as reduced time efficiency, high background stain, and antigen transformation by solvents, the multiplex F-SERS dot approach using the topical spray can detect tumor biomarkers in the bona fide tissue environment without any endoscopic manipulation or without major skin removal in case of intraoperative imaging. In addition, the FRES system has the capability of simultaneous SERS multiplexing accompanied by the fast-screening search by fluorescence signals, whereas confocal laser endomicroscopy is limited in multiplexing capability due to its broad bandwidth of fluorescence emission. Since the F-SERS dot strategy aimed to

provide characteristics of the tumor on site by simultaneous monitoring of several tumor antigens in the primary tumor, it could contribute to an earlier detection of a cancer in a patient with certain biomarkers that have therapeutic or prognostic significances,[29] and could help design patient-tailored therapeutic drugs for customized and personalized cancer therapy.

Conclusion

In this study, for *in vivo*, *in situ*, and intraoperative multiplexed endoscopic molecular diagnostics, the dual modal fluorescence-Raman endoscopic system (FRES) incorporating the fluorescence-SERS nanoprobe (F-SERS dots) having targeting moiety was developed; it can be easily applied to routine endoscopy. To achieve this main purpose, the dual modal endoscopic system was precisely designed to simultaneously detect fluorescence and Raman signals without mutual interference; it can provide the real-time fluorescence images for tracking the location of targeted area and Raman spectra for identifying the kinds of targeted nanoprobes at the same time. Along with endoscopic detecting system, as a targeting agent, the F-SERS dots were designed to simultaneously emit fluorescence and SERS signals with a single excitation laser-line. Furthermore, to specifically bind toward their own target, the efficient and reliable antibody conjugation method was developed by using quantitatively validated protocols while preserving intact antibody functionality. Lastly, the applicability and extendability of the FRES with F-SERS dots for translating to clinical application were demonstrated in breast and colorectal cancer xenograft models.

First, to properly confer selective targeting ability on the F-SERS dots as targeting agents, I developed a versatile and easy-to-operate antibody conjugation method using click chemistry, which retained the full bio-functionality of intact antibodies conjugated to the nanoprobes. Additionally,

the antibodies conjugated to the nanoprobes were quantitatively characterized using fluorescently-labeled antibodies and antigens, which is challenging in antibody-antigen conjugation-based bio-assay using nanoprobes. The results strongly indicate that the click chemistry-based conjugation strategy offers proper orientation of the target binding sites in antibodies on NPs and a high density of antibodies per single NP, while preserving the intact target-binding capability of full-length antibodies. Furthermore, I successfully demonstrated superior target binding ability of the antibodies on NPs by targeting HER2 in the MDA-MB-231/HER2 breast cancer cell-line. The versatility of this antibody conjugation method was also demonstrated with various types of silica-encapsulated nanoprobes.

To demonstrate the feasibility of the FRES as *in vivo* multiplexed molecular diagnostic tool, its sensitivity, real-time dual modal detecting ability, and multiplexed active targeting ability were evaluated in breast and colorectal cancer xenograft model. In breast cancer xenografts, the HER2 and EGFR expressed in the tumor tissues were successfully identified using antibody conjugated F-SERS dots by the FRES in a minimally invasive procedure. As illustrated in our results, the FRES can rapidly track the location of tumor and identify those pathological condition by detecting tumor receptor markers (HER2 and EGFR). Furthermore, in CRC xenograft model, the FRES can identify not only the tumor receptor marker (EGFR) but also tumor-secreted biomolecule (VEGF) as tumor microenvironment *via*

colonoscopic procedure; that features enable us to select most appropriate treatment option at an early stage. Also, by utilizing the intensity of Raman signal corresponding to targeted F-SERS dots, the relative quantification ability of FRES was also demonstrated in *in vitro* and *ex vivo* condition that allow to identify the molecular heterogeneity of the tumor, which is major obstacle for personalized therapy. From these results, I can believe that the real-time endoscopic molecular imaging technique using fluorescence and Raman dual-modality could potentially be applied to a routine endoscopic procedure where multiplexed molecular diagnosis of specific cancers or the differentiation of precancerous tissue from normal tissue at an early stage. In addition, this unique detection strategy can be applied for an accurate and efficient intraoperative molecular diagnosis of all tissues of the hollow organs accessible to an endoscope.

References

1. Bruno, M. Magnification endoscopy, high resolution endoscopy, and chromoscopy; towards a better optical diagnosis. *Gut* **52**, iv7-iv11 (2003).

2. Shukla, R., Abidi, W.M., Richards-Kortum, R. & Anandasabapathy, S. Endoscopic imaging: How far are we from real-time histology? *World J. Gastrointest. Endosc.* **3**, 183 (2011).

3. Khondee, S. & Wang, T.D. Progress in molecular imaging in endoscopy and endomicroscopy for cancer imaging. *J. Healthc. Eng.* **4**, 1-21 (2013).

4. Elahi, S.F. & Wang, T.D. Future and advances in endoscopy. *J. Biophotonics* **4**, 471-481 (2011).

5. Rosbach, K.J. et al. High-resolution fiber optic microscopy with fluorescent contrast enhancement for the identification of axillary lymph node metastases in breast cancer: A pilot study. *Biomed. Opt. Express* **1**, 911-922 (2010).

6. Funovics, M.A., Alencar, H., Montet, X., Weissleder, R. & Mahmood, U. Simultaneous fluorescence imaging of protease expression and vascularity during murine colonoscopy for colonic lesion characterization. *Gastrointest. Endosc.* **64**, 589-597 (2006).

7. Muldoon, T.J. et al. Evaluation of quantitative image analysis criteria for the high-resolution microendoscopic detection of neoplasia in Barrett's esophagus. *J. Biomed. Opt.* **15**, 026027 (2010).

8. Waldner, M.J., Wirtz, S., Neufert, C., Becker, C. & Neurath,

M.F. Confocal laser endomicroscopy and narrow-band imaging-aided endoscopy for in vivo imaging of colitis and colon cancer in mice. *Nat. Protoc.* **6**, 1471-1481 (2011).

9. Wang, T.D. & Van Dam, J. Optical biopsy: A new frontier in endoscopic detection and diagnosis. *Clin. Gastroenterol. Heptol.* **2**, 744-753 (2004).

10. Sonn, G.A. et al. Optical biopsy of human bladder neoplasia with in vivo confocal laser endomicroscopy. *J. Urol.* **182**, 1299-1305 (2009).

11. Dunbar, K.B., Okolo, P., 3rd, Montgomery, E. & Canto, M.I. Confocal laser endomicroscopy in Barrett's esophagus and endoscopically inapparent Barrett's neoplasia: a prospective, randomized, double-blind, controlled, crossover trial. *Gastrointest Endosc.* **70**, 645-654 (2009).

12. Neumann, H., Kiesslich, R., Wallace, M.B. & Neurath, M.F. Confocal laser endomicroscopy: technical advances and clinical applications. *Gastroenterology* **139**, 388-392, 392 e381-382 (2010).

13. Kiesslich, R. et al. In vivo histology of Barrett's esophagus and associated neoplasia by confocal laser endomicroscopy. *Clin. Gastroenterol. Heptol.* **4**, 979-987 (2006).

14. Kiesslich, R. et al. Chromoscopy-guided endomicroscopy increases the diagnostic yield of intraepithelial neoplasia in ulcerative colitis. *Gastroenterology* **132**, 874-882 (2007).

15. Kiesslich, R. et al. Confocal laser endoscopy for diagnosing intraepithelial neoplasias and colorectal cancer in vivo. *Gastroenterology* **127**, 706-713 (2004).

16. Laemmel, E. et al. Fibered confocal fluorescence microscopy

(Cell-viZio™) facilitates extended imaging in the field of microcirculation. *J. Vasc. Res.* **41**, 400-411 (2004).

17. Loeser, C.S., Robert, M.E., Mennone, A., Nathanson, M.H. & Jamidar, P. Confocal endomicroscopic examination of malignant biliary strictures and histologic correlation with lymphatics. *J. Clin. Gastroenterol.* **45**, 246-252 (2011).

18. Meining, A. et al. In vivo histopathology for detection of gastrointestinal neoplasia with a portable, confocal miniprobe: an examiner blinded analysis. *Clin. Gastroenterol. Heptol.* **5**, 1261-1267 (2007).

19. Waldner, M.J. et al. VEGF receptor signaling links inflammation and tumorigenesis in colitis-associated cancer. *J. Exp. Med.* **207**, 2855-2868 (2010).

20. Muldoon, T.J. et al. Noninvasive imaging of oral neoplasia with a high-resolution fiber-optic microendoscope. *Head & neck* **34**, 305-312 (2012).

21. Muldoon, T.J., Anandasabapathy, S., Maru, D. & Richards-Kortum, R. High-resolution imaging in Barrett's esophagus: a novel, low-cost endoscopic microscope. *Gastrointest Endosc.* **68**, 737-744 (2008).

22. Muldoon, T.J. et al. Subcellular-resolution molecular imaging within living tissue by fiber microendoscopy. *Optics express* **15**, 16413-16423 (2007).

23. Maru, D. et al. Evaluation of quantitative image analysis criteria for the high-resolution microendoscopic detection of neoplasia in Barrett's esophagus. *J. Biomed. Opt.* **15**, 026027-026027-026027 (2010).

24. Bergholt, M. et al. In vivo diagnosis of esophageal cancer

using image-guided Raman endoscopy and biomolecular modeling. *Tech. Canc. Res. Treat.* **10**, 103-112 (2011).

25. Garai, E. et al. High-sensitivity, real-time, ratiometric imaging of surface-enhanced Raman scattering nanoparticles with a clinically translatable Raman endoscope device. *J. Biomed. Opt.* **18**, 096008 (2013).

26. Weissleder, R. Molecular imaging in cancer. *Science* **312**, 1168-1171 (2006).

27. Goetz, M. & Wang, T.D. Molecular imaging in gastrointestinal endoscopy. *Gastroenterology* **138**, 828-833 e821 (2010).

28. van Dam, G.M. et al. Intraoperative tumor-specific fluorescence imaging in ovarian cancer by folate receptor-α targeting: First in-human results. *Nat. Med.* **17**, 1315-1319 (2011).

29. Atreya, R. et al. In vivo imaging using fluorescent antibodies to tumor necrosis factor predicts therapeutic response in Crohn's disease. *Nat. Med.* **20**, 313-318 (2014).

30. Short, M.A. et al. Development and preliminary results of an endoscopic Raman probe for potential in vivo diagnosis of lung cancers. *Opt. Lett.* **33**, 711-713 (2008).

31. Day, J.C. et al. A miniature confocal Raman probe for endoscopic use. *Phys. Med. Biol.* **54**, 7077-7087 (2009).

32. Huang, Z. et al. In vivo detection of epithelial neoplasia in the stomach using image-guided Raman endoscopy. *Biosens. Bioelectron.* **26**, 383-389 (2010).

33. Crow, P. et al. Assessment of fiberoptic near-infrared Raman spectroscopy for diagnosis of bladder and prostate cancer. *Urology* **65**, 1126-1130 (2005).

34. Bergholt, M.S. et al. Combining near-infrared-excited autofluorescence and Raman spectroscopy improves in vivo diagnosis of gastric cancer. *Biosens. Bioelectron.* **26**, 4104-4110 (2011).

35. Mo, J. et al. High wavenumber Raman spectroscopy for in vivo detection of cervical dysplasia. *Anal. Chem.* **81**, 8908-8915 (2009).

36. Bergholt, M.S. Raman Endoscopy for Objective Diagnosis of Early Cancer in the Gastrointestinal System. *J. Gastroint. Dig. Syst.* **01** (2013).

37. Wang, J. et al. Comparative study of the endoscope-based bevelled and volume fiber-optic Raman probes for optical diagnosis of gastric dysplasia in vivo at endoscopy. *Anal. Bioanal. Chem.* **407**, 8303-8310 (2015).

38. Wang, J. et al. Simultaneous fingerprint and high-wavenumber fiber-optic Raman spectroscopy improves in vivo diagnosis of esophageal squamous cell carcinoma at endoscopy. *Sci Rep* **5**, 12957 (2015).

39. Zavaleta, C.L. et al. A Raman-based endoscopic strategy for multiplexed molecular imaging. *Proc. Natl. Acad. Sci.* **110**, E2288-2297 (2013).

40. Mohs, A.M. et al. Hand-held spectroscopic device for in vivo and intraoperative tumor detection: Contrast enhancement, detection sensitivity, and tissue penetration. *Anal. Chem.* **82**, 9058-9065 (2010).

41. Ramanujam, N. et al. Cervical precancer detection using a multivariate statistical algorithm based on laser-induced fluorescence spectra at multiple excitation wavelengths. *Photochem. Photobiol.* **64**, 720-735 (1996).

42. Kang, H. et al. Near-infrared SERS nanoprobes with plasmonic Au/Ag hollow-shell assemblies for in vivo multiplex detection. *Adv. Funct. Mater.* **23**, 3719-3727 (2013).

43. Wang, Y. & Schlucker, S. Rational design and synthesis of SERS labels. *The Analyst* **138**, 2224-2238 (2013).

44. Dinish, U.S., Balasundaram, G., Chang, Y.T. & Olivo, M. Actively targeted in vivo multiplex detection of intrinsic cancer biomarkers using biocompatible SERS nanotags. *Sci. Rep.* **4**, 4075 (2014).

45. Nie, S. & Emory, S.R. Probing single molecules and single nanoparticles by surface-enhanced Raman scattering. *Science* **275**, 1102-1106 (1997).

46. Kneipp, K. et al. Single molecule detection using surface-enhanced Raman scattering (SERS). *Phys. Rev. Lett.* **78**, 1667 (1997).

47. Schlücker, S. SERS microscopy: Nanoparticle probes and biomedical applications. *ChemPhysChem* **10**, 1344-1354 (2009).

48. Samanta, A. et al. Ultrasensitive near-infrared Raman reporters for SERS-based in vivo cancer detection. *Angew. Chem. Int. Ed.* **50**, 6089-6092 (2011).

49. Kim, J.-H. et al. Nanoparticle probes with surface enhanced Raman spectroscopic tags for cellular cancer targeting. *Anal. Chem.* **78**, 6967-6973 (2006).

50. Maiti, K.K. et al. Development of biocompatible SERS nanotag with increased stability by chemisorption of reporter molecule for in vivo cancer detection. *Biosens. Bioelectron.* **26**, 398-403 (2010).

51. McVeigh, P.Z., Mallia, R.J., Veilleux, I. & Wilson, B.C. Widefield quantitative multiplex surface enhanced Raman scattering imaging in vivo. *J. Biomed. Opt.* **18**, 046011 (2013).

52. Lee, S. et al. Fabrication of SERS-fluorescence dual modal nanoprobes and application to multiplex cancer cell imaging. *Nanoscale* **4**, 124-129 (2012).

53. Qian, J., Jiang, L., Cai, F., Wang, D. & He, S. Fluorescence-surface enhanced Raman scattering co-functionalized gold nanorods as near-infrared probes for purely optical in vivo imaging. *Biomaterials* **32**, 1601-1610 (2011).

54. Yu, K.N. et al. Multiplex targeting, tracking, and imaging of apoptosis by fluorescent surface enhanced raman spectroscopic dots. *Bioconjugate Chem.* **18**, 1155-1162 (2007).

55. Larson, S.M., Carrasquillo, J.A., Cheung, N.K. & Press, O.W. Radioimmunotherapy of human tumours. *Nat. Rev. Cancer* **15**, 347-360 (2015).

56. Shen, B.Q. et al. Conjugation site modulates the in vivo stability and therapeutic activity of antibody-drug conjugates. *Nat. Biotechnol.* **30**, 184-189 (2012).

57. Jeong, S. et al. Fluorescence-Raman dual modal endoscopic system for multiplexed molecular diagnostics. *Sci. Rep.* **5**, 9455 (2015).

58. Noh, M.S. et al. Target-specific near-IR induced drug release and photothermal therapy with accumulated Au/Ag hollow nanoshells on pulmonary cancer cell membranes. *Biomaterials* **45**, 81-92 (2015).

59. Kocbek, P., Obermajer, N., Cegnar, M., Kos, J. & Kristl, J. Targeting cancer cells using PLGA nanoparticles surface

modified with monoclonal antibody. *J. Control. Release* **120**, 18-26 (2007).

60. Hui, J.Z. et al. Facile method for the site-specific, covalent attachment of full-length IgG onto nanoparticles. *Small* **10**, 3354-3363 (2014).

61. Hui, J.Z. & Tsourkas, A. Optimization of photoactive protein Z for fast and efficient site-specific conjugation of native IgG. *Bioconjugate Chem.* **25**, 1709-1719 (2014).

62. Vashist, S.K., Dixit, C.K., MacCraith, B.D. & O'Kennedy, R. Effect of antibody immobilization strategies on the analytical performance of a surface plasmon resonance-based immunoassay. *The Analyst* **136**, 4431-4436 (2011).

63. Jung, Y. et al. Controlled antibody immobilization onto immunoanalytical platforms by synthetic peptide. *Anal. Biochem.* **374**, 99-105 (2008).

64. Seo, M.H. et al. Controlled and oriented immobilization of protein by site-specific incorporation of unnatural amino acid. *Anal. Chem.* **83**, 2841-2845 (2011).

65. Kausaite-Minkstimiene, A., Ramanaviciene, A., Kirlyte, J. & Ramanavicius, A. Comparative Study of Random and Oriented Antibody Immobilization Techniques on the Binding Capacity of Immunosensor. *Anal. Chem.* **82**, 6401-6408 (2010).

66. Le, H.T., Jang, J.G., Park, J.Y., Lim, C.W. & Kim, T.W. Antibody functionalization with a dual reactive hydrazide/click crosslinker. *Anal. Biochem.* **435**, 68-73 (2013).

67. Jung, J., Yi, S.Y., Jang, H.H., Lee, C.-S. & Chung, B.H. Facile and oriented antibody immobilization on α-cyclodextrin-modified sensors surfaces. *Macromol. Res.* **21**, 130-133 (2012).

68. Song, H.Y., Zhou, X.D., Hobley, J. & Su, X.D. Comparative Study of Random and Oriented Antibody Immobilization as Measured by Dual Polarization Interferometry and Surface Plasnnon Resonance Spectroscopy. *Langmuir* **28**, 997-1004 (2012).

69. Natarajan, A. et al. NanoFerrite Particle Based Radioimmunonanoparticles: Binding Affinity and In Vivo Pharmacokinetics. *Bioconjugate Chem.* **19**, 1211-1218 (2008).

70. Kuzmin, A., Poloukhtine, A., Wolfert, M.A. & Popik, V.V. Surface Functionalization Using Catalyst-Free Azide-Alkyne Cycloaddition. *Bioconjugate Chem.* **21**, 2076-2085 (2010).

71. Prim, D. et al. ADIBO-based "click" chemistry for diagnostic peptide micro-array fabrication: physicochemical and assay characteristics. *Molecules* **18**, 9833-9849 (2013).

72. Hong, V., Presolski, S.I., Ma, C. & Finn, M.G. Analysis and optimization of copper-catalyzed azide-alkyne cycloaddition for bioconjugation. *Angew. Chem. Int. Ed.* **48**, 9879-9883 (2009).

73. Kotagiri, N. et al. Antibody quantum dot conjugates developed via copper-free click chemistry for rapid analysis of biological samples using a microfluidic microsphere array system. *Bioconjugate Chem.* **25**, 1272-1281 (2014).

74. Salehi, M. et al. Two-color SERS microscopy for protein co-localization in prostate tissue with primary antibody-protein A/G-gold nanocluster conjugates. *Nanoscale* **6**, 2361-2367 (2014).

75. Danczyk, R. et al. Comparison of antibody functionality using different immobilization methods. *Biotechnol. Bioeng.* **84**, 215-223 (2003).

76. Pathak, S., Davidson, M.C. & Silva, G.A. Characterization of the functional binding properties of antibody conjugated quantum dots. *Nano Lett.* **7**, 1839-1845 (2007).

77. Makaraviciute, A. & Ramanaviciene, A. Site-directed antibody immobilization techniques for immunosensors. *Biosens. Bioelectron.* **50**, 460-471 (2013).

78. Jung, Y., Jeong, J.Y. & Chung, B.H. Recent advances in immobilization methods of antibodies on solid supports. *The Analyst* **133**, 697-701 (2008).

79. Stöber, W., Fink, A. & Bohn, E. Controlled growth of monodisperse silica spheres in the micron size range. *J. Colloid Interface Sci.* **26**, 62-69 (1968).

80. Lee, K.H. et al. Technetium-99m-Labeled Antigranulocyte Antibody Bone Marrow Scintigraphy. *J. Nucl. Med.* **36**, 1800-1805 (1995).

81. Choi, C.W. et al. Development of bone marrow immunoscintigraphy using a Tc-99m labeled anti-NCA-95 monoclonal antibody. *Nucl. Med. Biol.* **22**, 117-123 (1995).

82. Shimizu, M. et al. (−)-Epigallocatechin gallate and polyphenon E inhibit growth and activation of the epidermal growth factor receptor and human epidermal growth factor receptor-2 signaling pathways in human colon cancer cells. *Clinical Cancer Research* **11**, 2735-2746 (2005).

83. Donigan, M. et al. Novel murine model for colon cancer: non-operative trans-anal rectal injection. *Journal of Surgical Research* **154**, 299-303 (2009).

84. Takahashi, T., Morotomi, M. & Nomoto, K. A novel mouse model of rectal cancer established by orthotopic implantation

of colon cancer cells. *Cancer science* **95**, 514-519 (2004).

85. Kim, K., Lee, H.B., Lee, Y.M. & Shin, K.S. Rhodamine B isothiocyanate-modified Ag nanoaggregates on dielectric beads: a novel surface-enhanced Raman scattering and fluorescent imaging material. *Biosens. Bioelectron.* **24**, 1864-1869 (2009).

86. Zhang, D., Ansar, S.M., Vangala, K. & Jiang, D. Protein adsorption drastically reduces surface-enhanced Raman signal of dye molecules. *J. Raman Spectrosc.* **41**, 952-957 (2010).

87. Zhang, X.-D. et al. Size-dependent in vivo toxicity of PEG-coated gold nanoparticles. *Int. J. Nanomed.* **6**, 2071 (2011).

88. Schipper, M.L. et al. A pilot toxicology study of single-walled carbon nanotubes in a small sample of mice. *Nat. Nanotechnol.* **3**, 216-221 (2008).

89. AshaRani, P.V., Low Kah Mun, G., Hande, M.P. & Valiyaveettil, S. Cytotoxicity and Genotoxicity of Silver Nanoparticles in Human Cells. *ACS Nano* **3**, 279-290 (2008).

90. Yen, H.-J., Hsu, S.-h. & Tsai, C.-L. Cytotoxicity and Immunological Response of Gold and Silver Nanoparticles of Different Sizes. *Small* **5**, 1553-1561 (2009).

91. Salouti, M. et al. A New Monoclonal Antibody Radiopharmaceutical for Radioimmunoscintigraphy of Breast Cancer: Direct Labeling of Antibody and Its Quality Control. *Eur. J. Nucl. Med. Mol. I.* **32**, S276-S276 (2005).

92. Davis, M.E., Chen, Z.G. & Shin, D.M. Nanoparticle therapeutics: an emerging treatment modality for cancer. *Nat. Rev. Drug Discovery* **7**, 771-782 (2008).

93. Kim, H.I. et al. Orientation and density control of bispecific

anti-HER2 antibody on functionalized carbon nanotubes for amplifying effective binding reactivity to cancer cells. *Nanoscale* **7**, 6363-6373 (2015).

94. Thorek, D.L.J., Elias, D.R. & Tsourkas, A. Comparative Analysis of Nanoparticle-Antibody Conjugations: Carbodiimide versus Click Chemistry. *Mol. Imaging* **8**, 221-229 (2009).

95. Jun, B.-H. et al. Ultrasensitive, Biocompatible, Quantum-Dot-Embedded Silica Nanoparticles for Bioimaging. *Adv. Funct. Mater.* **22**, 1843-1849 (2012).

96. Kim, J.H. et al. Nanoparticle probes with surface enhanced Raman spectroscopic tags for cellular cancer targeting. *Anal. Chem.* **78**, 6967-6973 (2006).

97. Woo, M.A. et al. Multiplex immunoassay using fluorescent-surface enhanced Raman spectroscopic dots for the detection of bronchioalveolar stem cells in murine lung. *Anal. Chem.* **81**, 1008-1015 (2009).

98. El Zouhairi, M., Charabaty, A. & Pishvaian, M.J. Molecularly targeted therapy for metastatic colon cancer: proven treatments and promising new agents. *Gastrointestinal cancer research: GCR* **4**, 15 (2011).

99. Goetz, M. et al. In vivo molecular imaging of colorectal cancer with confocal endomicroscopy by targeting epidermal growth factor receptor. *Gastroenterology* **138**, 435-446 (2010).

100. Foersch, S. et al. Molecular imaging of VEGF in gastrointestinal cancer in vivo using confocal laser endomicroscopy. *Gut* **59**, 1046-1055 (2010).

101. van Scheltinga, A.G.T. et al. Intraoperative near-infrared

fluorescence tumor imaging with vascular endothelial growth factor and human epidermal growth factor receptor 2 targeting antibodies. *Journal of Nuclear Medicine* **52**, 1778-1785 (2011).

102. Yarden, Y. The EGFR family and its ligands in human cancer: signalling mechanisms and therapeutic opportunities. *European journal of cancer* **37**, 3-8 (2001).

103. Park, J.E., Keller, G.-A. & Ferrara, N. The vascular endothelial growth factor (VEGF) isoforms: differential deposition into the subepithelial extracellular matrix and bioactivity of extracellular matrix-bound VEGF. *Molecular biology of the cell* **4**, 1317-1326 (1993).

104. Oh, Y. et al. Thoracoscopic color and fluorescence imaging system for sentinel lymph node mapping in porcine lung using indocyanine green-neomannosyl human serum albumin: intraoperative image-guided sentinel nodes navigation. *Ann. Surg. Oncol.* **21**, 1182-1188 (2014).

105. Eser, S. et al. In vivo diagnosis of murine pancreatic intraepithelial neoplasia and early-stage pancreatic cancer by molecular imaging. *Proc. Natl. Acad. Sci.* **108**, 9945-9950 (2011).

106. Pan, Y. et al. Endoscopic molecular imaging of human bladder cancer using a CD47 antibody. *Sci. Transl. Med.* **6**, 260ra148 (2014).

요 약

최근 광학 영상과 더불어 생체 발광, 형광, 라만 신호 등이 병합된 내시경 기술이 개발됨으로써, 생체 중공기관(hollow organ) 내 표면의 세포 내 구조적 변성과 병리학적 조건을 실시간으로 진단 가능해 지고 있다. 특히, 생체 내 암과 관련된 생체 표적 분자들과 선택적으로 결합이 가능한 타겟팅 분자 표지자 (molecular probes) 기술과 내시경 영상 기술을 동시에 활용함으로써 생체 내, 그리고 수술 중 분자 진단이 가능할 수 있게 되었다. 이러한 생체 내 분자 진단은 생체 내에서 암과 관련된 생체 물질의 발현을 내시경적 진단 중에 확인 함으로써 암의 조기 진단, 개인별 치료, 영상 유도 치료 등을 가능케 한다. 다양한 분자 표지자 기술 중 형광 기반 분자 표지자 기술은 넓은 영역에서 분자 표지자에 의해 특이적으로 표적화된 영역을 영상화하는 기술로서 널리 활용되고 있다. 이와 더불어 표면증강라만산란(surface enhanced Raman scattering, SERS) 나노 입자는 높은 민감도와 다중 측정 능력을 가지고 있어 다중 분자 진단 기술에 폭넓게 활용되고 있다.

진단과 치료에 활용하기 위한 분자 타겟팅 물질로서 항체가 결합된 나노입자는 높은 신호 민감도와 생체 표적에 대한 특이성, 그리고 폭넓을 활용성을 가짐으로써 그 잠재력이 매우 크다. 하지만 불행히도 이러한 특징들은 나노입자에 항체를 도입하는 방법에 따라 항체 도입 효율, 도입된 항체의 배향, 그리고 항체 생체 활성의 변성도 등이 크게 달라지게 됨으로써 그 성능과 효험이 크게 달라지게 된다. 또한 단일 나노입자에 도입되는 항체의 숫자나 도입된 항체의 항원 표적 능력을 파악하는 것 또한 나노입자를 기반으로 하는 정량적 생물학적 검정에서 매우 중요한 요소이다. 이를 위해, 본 연구에서는 촉매(구리)를 사용하지 않는 Click Chemistry를 활용하여 나노입자의 표면에 항체 배향을 조절함과 동시에 높은 효율

로 항체를 도입할 수 있는 손쉬운 항체 도입 기술을 개발하였다. 또한 나노입자의 표면에 도입되는 항체의 개수와 도입된 항체의 항원 표적 능력을 형광이 표지된 항원과 항체를 활용하여 정량적, 그리고 실험적으로 입증 가능한 프로토콜을 제시하였다. 이를 통해 단일 나노입자에 도입되는 항체의 개수와 그 항원 결합 능력을 평가 할 수 있었으며, 더 나아가, Click chemistry를 통해 도입된 항체의 활성과 기존에 널리 활용되고 있는 항체 도입 방법(EDC/NHS 결합 방법)으로 도입된 항체의 활성을 비교 분석하였다. 결과적으로 Click chemistry를 통해 도입된 생체 활성이 기존의 방법으로 도입된 항체보다 8배 높은 항원 결합 능력을 보유하고 있음을 확인하였다.

생체 내에 존재하는 의심 병변의 분자 병리학적 정보를 내시경 진단 과정에서 다중 분석 방법으로 확인하기 위해, 형광-라만 내시경 시스템과 더불어 생체 표적 타겟팅 물질로 형광-표면증강라만 활성 다중 나노 표지물질(Fluorescence-SERS nanoprobe, F-SERS dots)을 개발하였다. 이 형광-라만 내시경 시스템과 항체가 결합된 다중 나노 표지 물질을 활용하여, 형광 신호를 활용한 실시간 분자 영상과 표면증강라만산란 신호를 활용한 다중 생체 표적 분석 결과를 동시에 얻음으로써 생체 내 존재하는 유방암 그리고 직장암 모델에 대한 다중 분자 진단을 체내에서 그리고 실시간으로 성공적으로 수행할 수 있었다. 유방암 모델에서는 종양 세포 표지 인자로 인간표피성장인자 수용체2 (human epidermal growth factor 2. HER2) 그리고 표피생장인자 수용체(epidermal growth factor receptor, EGFR)의 생체 표적 분자를 내시경적 다중 분자 진단 기술을 활용하여 동시에 성공적으로 검출할 수 있었다. 또한 실제 임상 모델로서, 직장암 모델에서는 종양 세포에 대한 표지 인자로 표피생장인자 수용체(epidermal growth factor receptor, EGFR)를 종양 세포 외 기질에 존재하는 종양 미세환경 표지 인자

로 혈관내피성장인자 (vascular endothelial growth factor, VEGF)를 대장내시경적 다중 분자 진단 기술로써 성공적으로 검출해 낼 수 있었다. 그 뿐만 아니라, 형광-라만 내시경 시스템을 활용하여 체외/탈체 조건에서 검출된 라만 신호를 기반으로 생체 표적 분자에 대한 상대적 정량 분석이 가능함으로써 종양의 이질적인 분자 특성도 확인할 수 있는 가능성도 확인하였다. 이를 통해 형광-라만 내시경 시스템은 생체 내 다중 분자 진단 기술로서 실시간으로 특정 암 조직의 종양 세포 수용체와 종양 미세환경까지 확인함으로써 암의 조기진단, 개인별 맞춤형 치료를 가능케 할 수 있음을 확인하였다.

주요어 : 형광-라만 내시경 시스템, 체내 다중 분자 진단, 전신 항체 도입, 정량적 분석, 항체 배향 조절, 촉매(구리) 배제 Click Chemistry, 유방암, 직장암

학 번 : 2012-31069